Spectrally Agile Endoscopic Fluorescence Imaging

Steven D. Quinn, M.Phys.

Hertford College

&

The Gray Institute for Radiation, Oncology and Biology,

University of Oxford

A Thesis submitted for the degree of Master of Science by Research at the University of Oxford, United Kingdom.

Submitted September 2010

Word count: ~ 22000

Spectrally Agile Endoscopic Fluorescence Imaging

Steven. D. Quinn, M.Phys.

(M.Sc. by Research candidate)

Hertford College, University of Oxford.

Submitted September 2010

Abstract

During minimally invasive (keyhole) tumour resection surgery, the sentinel node is typically visualized by injecting an opaque dye into the tumour and monitoring uptake in the node via endoscopy. Conventional illumination methods for sentinel node mapping are limited to shallow penetration depths causing nodes below fat tissue to be overlooked. This paper reports on the development of novel optical techniques for the implementation of a spectrally-agile laparoscopic system capable of identifying near-infrared fluorescence from clinically-approved fluorescent dyes. The construction of a tuneable illumination unit is described; this combines a series of near-infrared laser diodes with conventional visible light for fluorescence excitation and sample illumination respectively. Additionally, a methodology based on a micro-lens approach for separating near-infrared fluorescence images from conventional colour images at the laparoscope's eyepiece with minimal distortions is presented. Near-infrared detection methods based on optical

multichannel analyzers are discussed, with special consideration given to their commercial availability and potential for endoscopic applications in the abdominal, gastrointestinal and gynaecological cavities. In order to determine maximum penetration depths achievable with our system, Monte Carlo and analytic methods have been implemented to model photon transport through mammary fat tissue at visible and near-infrared wavelengths, revealing imaging sensitivity. Specifically, expected optical penetration depths at 690 nm, 732 nm, 785 nm and 830 nm are 2.27 mm, 2.90 mm, 3.15 mm and 3.26 mm respectively. In essence, laparoscopic assisted spectroscopy based on tuneable excitation and emission can be employed to increase sensitivity and specificity of sentinel node detection and may provide the additional benefit of differentiation between normal and cancerous tissue.

Contents

Acknowledgements

I would like to take this opportunity to thank my co-supervisors, Professor Borivoj Vojnovic (Gray Institute for Radiation, Oncology and Biology, University of Oxford) and Professor Tony Wilson (Dept. of Engineering, University of Oxford) for their valuable advice and support throughout the duration of this project. I am particularly indebted to Dr. Iain Tullis (Gray Institute) and Dr. Iestyn Pope (University of Cardiff) for providing support, motivation and inspiration as well as the project's principal investigator, Mr. Stephen Kennedy (Nuffield Dept. of Obstetrics and Gynaecology, University of Oxford), without whom this project would not have been possible. Thanks must also goes to Dr. Roberto Tozzi and his surgical team (Churchill Hospital, Oxford) for tutoring me in the physiological and practical aspects of laparoscopic surgery. Prof. Peter Dobson and Dr. Helen Townley provided crucial advice with regards to fluorescent dyes and Dr. Rasiah Bharathan offered his clinical expertise on laparoscopic procedures and anatomy of the lymphatic system. Mr. Robert Newman was involved in the production of electronic components for our apparatus and Dr. Paul Barber, Mr. Glen Pierce (both Gray Institute) and Dr. Rehan Ali (Stanford University) were involved in the development of imaging software. I would like to acknowledge Dr. Sarah Norman, Dr. Nikki Sibson, Mrs. Debbie Luther and Prof. Gillies McKenna (all Gray Institute), for their guidance and support during the course of my studies and I owe Mr. John Prentice and Mr. Gerry Shortland (both Gray Institute) a great deal of gratitude for their explanations

and advice as to the practical aspects and limitations of mechanical engineering.

I am incredibly thankful for the financial support of the Medical Research Council (MRC), Cancer Research UK (CR-UK) and the Engineering and Physical Sciences Research Council (EPSRC) for allowing this project to realise its potential, and for funding my studies.

Glossary

$\in \mathbb{Z}$	in the set of integers.
5-ALA	5-Aminovelunic acid.
^{99m}TC	Technetium 99.
CAD	Computer aided design.
CCD	Charge-coupled device
CT	Computerized tomography.
Cy5.5	Cyanine 5.5.
Cy 7	Cyanine 7.
f	Focal length.
FOV	Field of view
H-G	Henyey-Greenstein (phase function).
H_20	Water.
Hb	Haemoglobin.
HbO_2	Oxyhaemoglobin.
ICG	Indocyanine green.
λ	Wavelength.
Lymph	Lymphatic
MRI	Magnetic resonance imaging.
n	Refractive Index.
NIR	Near infrared.
ν	Optical frequency.
NA	Numerical aperture.
P	Power
PpIX	Protoporphyrin IX.
PVC	Polyvinyl chloride.
RGB	Red, green and blue.
S	Singlet energy state.
SNR	Signal to noise ratio.
SPIONs	Super-paramagnetic iron oxide nanoparticles.
T	Triplet energy state.
UNF	Unified fine thread

Chapter 1

Introduction

1.1 The Clinical Need for a Spectrally Agile Endoscopic Fluorescence Imaging System.

During conventional minimally invasive (keyhole) tumour resection surgery, the stage (an indicator of how much cancer cells have metastasised) is often estimated by examining tumour characteristics such as size, mass and penetration depth into surrounding tissue. Its measure is arguably the most powerful predictor of survival and is fundamentally critical, particularly during the early stages of diagnosis, since treatments, if any, are based upon its interpretation. Yet in order to deduce the stage as accurately as possible, and ultimately gain an understanding of the growth and expansion of the tumour into adjacent and/or distant organs, an analysis of the surrounding lymphatic system is required. In essence, the number of lymphatic nodes the tumour has metastasized to, in conjunction with their locations, can reveal clues regarding tumour evolution and future progression.

Lymphatic nodes and vessels in the vicinity of a tumour are traditionally visualised by injecting opaque, clinically approved dyes into tumour tissue such that drainage into the lymphatics can be monitored ‘by eye.’ In extracting the information associated with such node mapping techniques however, one inevitably relies on a method which is entirely dependent on user experience,

and unreliable where the lymphatic system is obscured by fat tissue. Conventional illumination methods for node mapping are currently limited to shallow penetration depths and nodes underneath layers of tissue are likely to be overlooked.

By utilising clinically approved near-infrared (NIR) fluorescent dyes (e.g. indocyanine green and methylene blue) imaged with a spectrally-agile laparoscopic system, greater penetration depths may be achieved, revealing otherwise obscured lymphatic nodes underneath multiple tissue layers. A laparoscopic approach based on excitation and emission tunability, has the potential to increase sensitivity and specificity, whilst allowing multiple dyes to be used *in vivo*. Visual detection of lymphatic nodes adjacent to a tumour is critical for determining the extent of metastasis and is likely to be improved with the introduction of a minimally invasive instrument capable of detecting a range of NIR fluorescence wavelengths from clinically approved dyes.

Early detection of lymphatic nodes, and particularly those receiving drainage from a primary tumour, is likely to enhance the efficiency of diagnostic techniques and may affect treatment plans offered to patients. With growing evidence to suggest that the use of NIR fluorescence improves the detection of tumour metastasis, a methodology which utilises such a technique for detection and visualization of the lymphatic system is likely to improve patient morbidity rates. The quality of life for patients requiring such surgery is likely to improve as a result, with a reduction in the risk of tumour recurrence expected to follow.

1.2 Medical Science Background and Clinical Anatomy of the Lymphatic Node.

In recent years, notable progress has been made towards a comprehensive understanding of the dynamics which underpin the lymphatic system and its circulation [1]. In this section, an overview of the structure and anatomy of lymphatic nodes, together with the characteristics that are likely to be observed at the microscopic level is provided. In the discussion which follows, the sentinel lymphatic node is defined as being the first node to which cancer cells metastasize from a primary tumour.

Lymphatic (lymph) nodes are encapsulated oval-shaped masses of lymphoid tissue with lengths ranging from 1 - 25 mm. Located near junctions of the major lymphatic vessels and most notably concentrated in the neck, thoracic duct, the abdomen, pelvis and proximal regions of the limbs [2], their function is to provide a filter for the blood, exposing trapped foreign antigens to the immune system for annihilation. Specifically, their purpose is to generate B and T cells, add antibodies to the blood flow and remove sub-micro particles from fluid drained from adjacent organs. By definition however, nodes in the vicinity of a primary tumour are susceptible to accumulating metastasising cancer cells.

A two-dimensional cross-section of a typical lymphatic node is shown in Figure 1. The node structure can be well represented by a mass consisting of two distinct components: the capsule, an outer layer of connective tissue, and the cortex, the functional area of the lymph node surrounded by an inner medulla. The latter contains inactivated B and T lymphocytes and numerous

cavities through which lymph from afferent lymphatic vessels flow and into which cells may become attached. A distinctive feature of a node's overall appearance is an indentation (hilum) on one of its sides through which efferent lymphatic vessels and the medulla surface and blood vessels enter and exit.

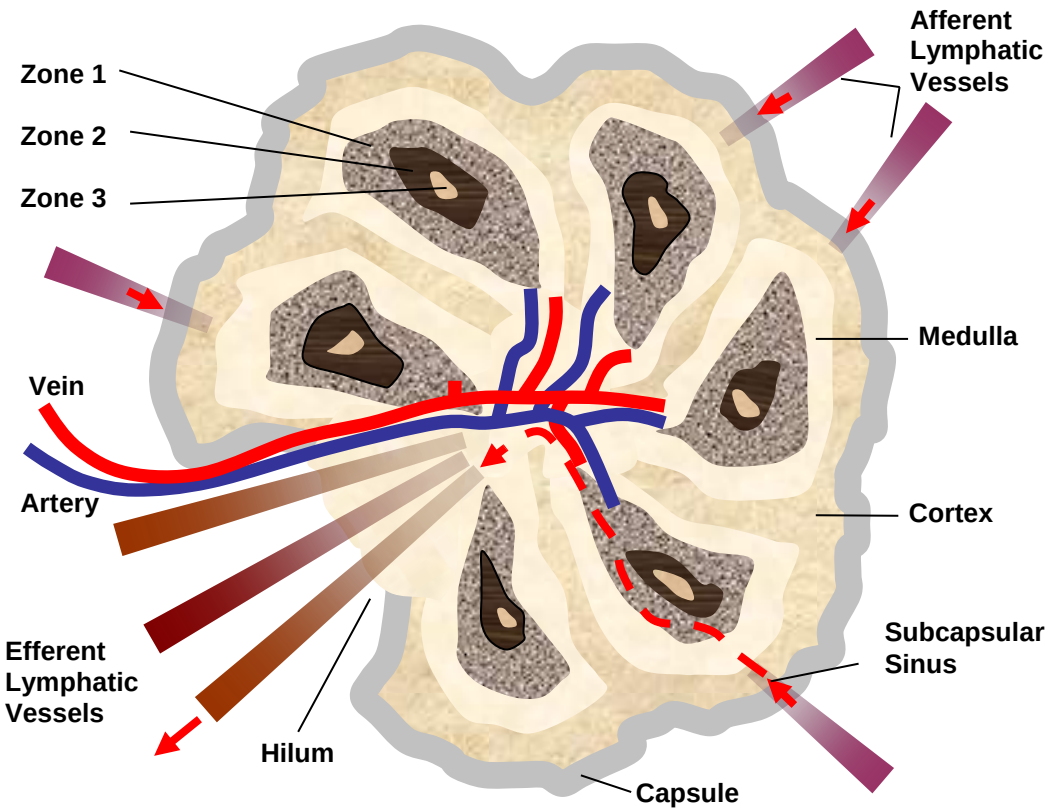

Figure 1. Two-dimensional cross-section of a typical lymphatic node. The capsule and cortex form the outer shell and functional area respectively. Afferent lymphatic vessels entering via the capsule transport fluid into the functional area, whilst efferent vessels situated at the hilum remove the processed fluid, allowing circulation to progress.

The capsule is composed of flattened reticular cells embedded within a network of fine collagen fibres and has the role of supporting the mass contained within the cortex and lymphatic vessels which penetrate its surface. The cortex contains a distribution of lymphatic channels through which fluid travels after entry into the node via afferent vessels. The vessels, each of

which may be connected to a secondary node, penetrate the node at numerous locations and form an opening into a region adjacent to the capsule (subcapsular sinus) through which lymph may be collected. The channels subsequently expose lymph to phagocytic cells as well as B and T lymphocytes such that the internal environment of the body is protected from endothelia and damage by undesirable foreign and endogenous agents.

Straight-branched veins and arteries, which carry blood to and from the node respectively, enter via the hilum and cross the medulla. Upon reaching the cortex and follicles (regions of densely packed lymphocytes), arteries form an intricate network of arterioles and capillaries [3], all of which eventually connect to highly branched veins via junctions which part to allow the passage of cells [4] (Figure 2). Furthermore, veins have the ability to exit the cortex in order to supply the capsule and surrounding connective tissue with oxygen. Lymphatic vessels are, in general, larger than surrounding capillaries but both ensure unidirectional flow, the course of which is determined by a series of valves. The lymphatic node, and indeed system, is thus an exceptionally dynamic and reactive arrangement.

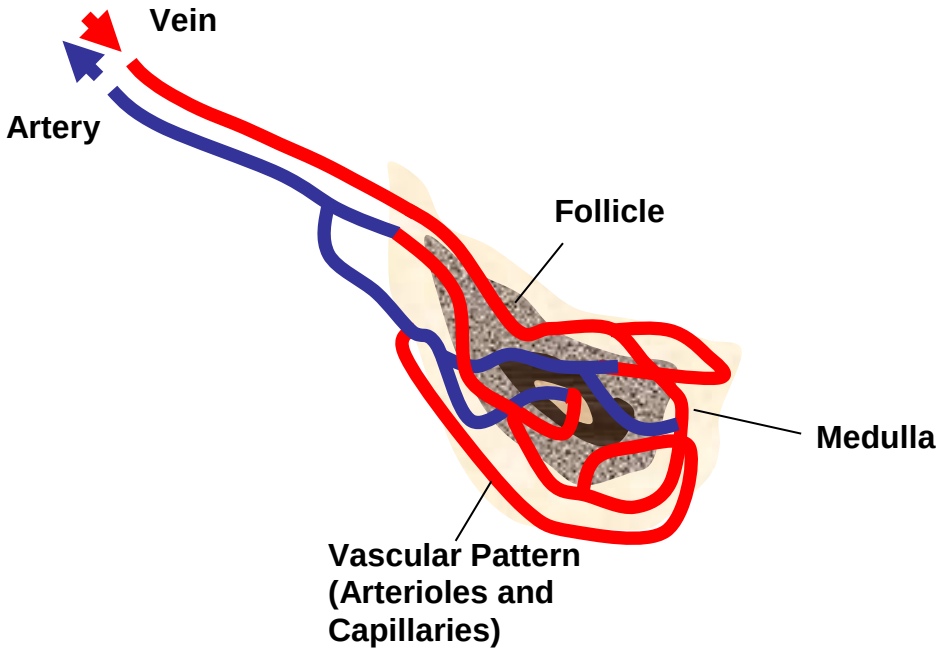

Figure 2. An illustration of lymphatic vascular patterns occurring near the follicle and capsule.

The distribution and density of lymphocytes and cells within the cortex varies from region to region. The reticulum is predominantly host to B and T lymphocytes but macrophages may also be found. Cells within the subcapsular sinus may be washed into the lymph during its circulation, and in the body of the cortex, cells are so densely packed that lymphoid structures (follicles) may form. Nopajaroonsri *et al.* [5] suggest three different zones within the follicles exist, each of which contains a different cell packing density and distinct cell type. The first zone (zone 1) has the lowest packing density and is located on the outer edge of the follicle. Small inactivated lymphocytes, macrophages and plasmacytes may be found here, extending towards the centre of the node and into the medulla. The second zone (zone 2) comprises a denser region of predominantly small inactivated lymphocytes and macrophages. Zone 3 forms the central germinal cores of the lymph node and tend to be observed in nodes which have been antigenically stimulated. The

cells in this region include large lymphoblasts, macrophages and dendrimers. Activated cells contained within the follicle structures may traverse the medulla and exit the node via efferent vessels before being passed towards adjacent nodes or the thoracic duct. The number of lymphocytes within the medulla itself is small in comparison and those that do exist have the ability to form irregular branching cords into which macrophages, plasmacytes and granulocytes may become entangled.

1.3 Reported Methods for Sentinel Node Mapping.

Since the concept of the sentinel node was first demonstrated in a feline model by Cochran *et a*l. [6] its clinical importance has become one of the most researched topics in the field of surgical oncology. Notably, recent studies suggest that sentinel node mapping techniques in gastrointestinal and breast cancers could improve post-operative prognosis and patient quality of life [7, 8, 9, 10].

Despite the field of sentinel node mapping being in its infancy, a variety of detection methods currently exist. Many groups report a radio-guided method in which radiopharmaceuticals are injected intradermally at the site of a primary tumour and detected externally as they drain into the lymphatics by a probe mounted to the distal end of an endoscope or a gamma camera placed external to the body. Others use clinically approved opaque dyes, either alone or in combination with probe detection, to allow lymphatic drainage to be visualized by eye. Only recently, however, have such dyes been used for NIR fluorescence studies, allowing nodes underneath layers of tissue fat to be revealed for the first time. Some studies use this technique for

identification of the sentinel lymph node only, whilst others aim to detect most or all of the nodes within the same lymphatic basin. However, as such reports are playing a crucial role in the detection of metastasis locations, debates as to the location and number of injection sites and concentration of injectate prescribed still exist.

i. The Radio-Guided Method

Drainage of the lymphatic system was first demonstrated by radiographic injection using Ethiodol, a radio-opaque agent common to hysterosalpingography [11]. A report by Sherman *et al.* which followed demonstrated the uptake of colloidal gold in lymph nodes after interstitial injection via autoradiography [12]. Crucially, both papers formed the basis of clinical studies aimed at monitoring the lymphatic drainage of breast carcinoma – the first studies to apply autoradiography to the spread of cancer. Today, a variety of clinics use radioactive tracers for the diagnosis and prognosis of not only breast, but a variety of different types of cancer.

A number of techniques have been employed for injecting a suitable radioactive tracer into the region under investigation. Lymphatic tissue is predominantly found in the vicinity of the peripheral skin layer, suggesting injection into the subdermal region should allow the radioactive substance to enter the lymphatic system via associated vessels. Direct injection into a tumour is less favourable because tissue within its structure has fewer lymphatic vessels and is often subject to high intersititial and intercellular pressures. Thus, direct injection may lead to leakage of the tracer from the tumour into surrounding tissue as well as the induction of micrometastasis

from the needle track. At present, the literature suggests such consequences are unlikely to effect the long-term development of the tumour or prognosis, but nevertheless, direct injection should only be performed if the disadvantages are outweighed [13].

Radioactive tracers were initially developed for detecting the liver's reticuloendothelial system, the bone marrow and spleen, and as such, their characteristics were non-optimal for the detection of lymphatic nodes. However, the introduction of colloid labelled with the metastable isomer of technetium-99, ^{99m}TC, revolutionized lymphoscintigraphy. With a physical half-life suitable for detection in humans, universal accessibility and a relatively low cost per Becquerel, it became a test-bed for a number of studies which tried to develop radiocolloids with improved retention properties. Most notably, the introduction of smaller radiocolloids allowed node retention to be improved and an optimum size of ~10 nm was suggested [14].

After appropriate selection of a radiocolloid and injection site, particles enter tissue fluid from which they are drained into the nodal basin and lymphatic nodes. Geiger-Müller probes mounted to the distal end of an endoscope are suitable for tracking the location and progress of the radiocolloid particles as they pass into the lymphatic vessels. High frame-rate gamma cameras external to the body offer an alternative detection method but both are useful for providing information with respect to radiocolloid migration. Regions of the body which are observed to emit increased levels of radioactivity correspond to probable locations of the lymphatic nodes (Figure 3).

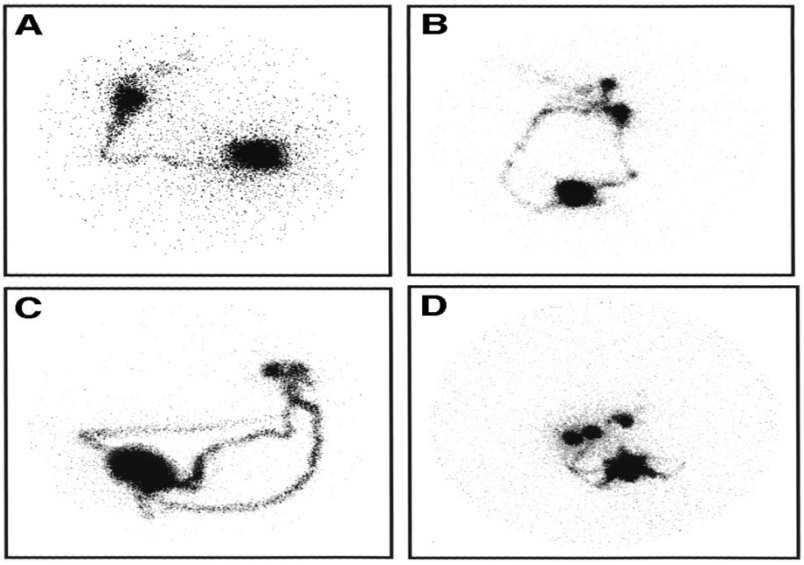

Figure 3 [15]. Regions in the body where high levels of radioactivity are detected correspond to locations of the lymphatic nodes and channels.

Depending on the radiocolloid used and indeed the specific application for which they are used, probes are chosen based on their sensitivity, resolution and ease of use *in vivo*. Probe resolutions may differ by a factor of 4, and up to a factor of 20 with respect to sensitivities [16] and are set to rise with the continued interest shown in sentinel node detection. However, the radio-guided method is often non-optimal and subject to several limiting factors. For instance, high levels of radioactivity are observed at the injection site, suggesting nodes within this region may not be visualized. Additionally the very act of injecting a radioactive tracer into the body is in itself, an undesirable procedure.

ii. The Dye-Guided Method

The development of the dye-guided method by Morton *et al.* [17] revolutionized the field of sentinel node mapping, by providing a convenient and much safer methodology. By indicating that the sentinel node could be

detected successfully by injection of an opaque dye such as isosulfan blue at the site of a primary tumour, an array of clinical applications followed. Specifically, the detection concept has been practiced in melanoma, breast and gastric cancers [18, 19, 20].

After the introduction of general or local anaesthesia, the dye is injected intradermally at the tumour site. If the tumour has previously been removed, the injections are performed on each side of the excision scar. Intradermal injections ensure that the dye travels to nodes receiving drainage from the tumour, rather than deeper and distinct lymphatic nodes via veins. To minimize the latter, only a small volume of dye (0.5 – 1 ml) is injected at any given time to avoid excretion of the dye into the subcutaneous tissue. The injection site is thereafter massaged to promote the flow of dye into the lymphatic system and nodes. Typically ten minutes post-administration, tissue overlying the expected location of the lymph basin closest to the primary tumour is removed and the lymphatic channels and nodes receiving drainage are visually identified, since nodes become discoloured as they receive dye uptake. In this way, the sentinel lymph node may be identified from other nodes contained within the lymphatic basin and excised for biopsy, allowing an understanding of the tumour's progression to be gained.

Post-operative complications with the dye-guided method are rare and trivial. Most patients do however report a blue discolouration of the urine 1 – 24 hours after the operation, and many report staining at the location of the first injection site several months later. Significantly, no instances of hypersensitivity or damage to the immune system have been reported as a consequence of the method.

Lymph node detection by the dye-guided method is a convenient and safe method for detection of the true sentinel node. However, navigational surgery based on a method which depends entirely on user experience has the potential for false-negative, sentinel nodes to be reported. The most common cause of this is due to obstructions in the lymphatic channels by massive cancerous invasion. In such a scenario, the administered dye fails to migrate to the true sentinel node and excretes to second-tier lymphatic nodes as a consequence. Such a limitation has particular implications for patient survival rates, particularly during the early stages of diagnosis. Additionally, nodes below layers of tissue fat may not be identified by-eye, emphasising the need for additional improvements to the method.

iii. The Fluorescence Guided Method

Contemporary advances in node detection have resulted in a technique which utilises the NIR fluorescence properties of clinically approved dyes to achieve imaging at greater penetration depths in tissue. In particular, indocyanine green (ICG) is being established as the most useful fluorescent diagnostic reagent for monitoring hepatic function, vascular flow and cardiac output during surgery [21, 22]. Recently, its fluorescence characteristics have realised a new method for sentinel node navigation surgery in gastric and breast cancer [23, 24]. Following intradermal administration at the tumour site, lymphatic vessels and nodes can be visualized, their locations identified and their uptakes monitored via fluorescence imaging.

ICG, despite its non-linear fluorescence properties, has a strong affinity and biochemical compatibility with plasma proteins in living tissue. When fully

bound [25], a peak fluorescence emission at ~ 840 nm when excited at 800 nm is observed. Consequently, it becomes well distributed and detected within the intravascular space and its near-infrared fluorescence emission subsequently allows nodal drainage to be visualized under several layers of tissue. Lymphatic nodes, specifically those not directly visible by eye, may be observed by their bright fluorescence signals. Sensitivity of the fluorescence-guided method is therefore potentially greater than that of previously reported techniques. Sentinel lymph node biopsy using the fluorescence guided method is not only convenient and safe, but is providing surgeons with an improved tool for assessing the status of lymphatic nodes and vessels in the vicinity of primary tumours.

Imaging NIR fluorescence emission is commonly performed using a charge-coupled device (CCD) camera in combination with NIR bandpass filters and a method of excitation. One common excitation approach is to utilise an array of light-emitting diodes of appropriate wavelengths mounted onto the periphery of the detector [23]. Captured fluorescence signals are transmitted to a digital video processor and thereafter displayed on high-definition monitors in real time.

The fluorescence guided method is rapidly proving to be an innovative clinical technique for node resection and staging. Yet whilst a variety of tumour-specific NIR dyes have been developed, only a small number have been approved for use in the clinic. Indocyanine green is favoured in many cases as the gold-standard, but the fluorescence guided method is not strictly limited to studies which incorporate its use. In the field of surgical gynaecology for example, a clinical case reporting metastasis from ovarian

cancer to the sentinel lymph node via detection of 5-aminovelunic acid (5-ALA) induced proto-porphyrin IX fluorescence has been documented [26]. Additionally, the dye has been shown to assist in the early detection of bladder cancer [27], malignant gliomas [28] and lymphatic node metastasis in mouse rectal cancer [29]. In the latter, PPIX fluorescence occurring as a result of exogenous application of 5-ALA was shown to play a crucial role in the detection of microscopic lymph node metastases of digestive organ cancer with a high diagnostic accuracy and sensitivity. In principal, colorectal cancers could therefore be distinguished by endogenous application in humans. Additionally, the differences in accumulation of PPIX in tumour and normal lymphatic tissue allow identification of metastatic foci by fluorescence stereomicroscopy and ultimately differentiation between normal and cancerous tissue.

Recently, Tajima *et al*. demonstrated sentinel node mapping in gastric cancer by indocyanine green fluorescence imaging during laparoscopy-assisted gastrectomy [30]. Imaging was achieved using local bandpass filters and a NIR sensitive CCD camera with an array of NIR light-emitting diodes acting as the excitation source. Highly sensitive intraoperative imaging of sentinel nodes was achieved, with bright regions of fluorescence against a dark background corresponding to the location of lymphatic nodes. Crucially, no adverse effects or complications to patient health were observed after surgery.

1.4 Endoscopy

1.4.1 Fields of Application

The introduction of endoscopy has revolutionized many surgical procedures, allowing intra-operative techniques to be performed in a minimally invasive fashion. As a direct consequence of its implementation, patient mortality and morbidity rates have reduced, post-operative recovery times have fallen and the quality of life for those requiring surgery has undoubtedly improved. Complications arising as a result of endoscopic procedures are rare, minor and not life-threatening [31] and the techniques have been shown to yield a higher degree of accuracy compared with conventional open-surgery. Specific fields of application which document the importance of endoscopy are laparoscopy and colonoscopy.

Laparoscopy is often defined as the procedure in which the abdominal or pelvic cavity is sufficiently inflated with carbon dioxide such that the abdominal wall is elevated above the internal organs. This creates a working space into which a laparoscope can be inserted. Carbon dioxide is used primarily because of its non-flammable properties and natural absorption into tissue for removal by the respiratory system. Specifically, laparoscopy has been used for the diagnosis and therapy of paediatric abdominal trauma [32] in addition to the detection of colon [33] and ovarian [34] cancers.

The field of colonoscopy specifically targets the proximal, descending and sigmoid colons, cecum, rectum and latter stages of the digestive system via flexible endoscopy. In many cases the procedure is performed in conjunction with computer aided tomography (CAT) and magnetic resonance

imaging (MRI) scans. Ulcers and untreated colorectal polyps, which form the foundations of colorectal cancer may be visualized and removed for biopsy [35]. Additional benefits include the detection and diagnosis of gastrointestinal lesions and inflammatory bowel disease [36].

1.4.2 Classification of Endoscopes

Technological advancements in optical engineering and imaging modalities have played a crucial role in the design of a variety of minimally invasive surgical instruments. Most notably, the evolution of endoscopy has led to the visualisation and manipulation of anatomical objects at sites otherwise only accessible by open surgery. Post-operative patient prognosis and morbidity rates have subsequently improved, and as endoscopic procedures develop in complexity, improvements to their optical design for the analysis of specific organ tissue have been made, in turn allowing contemporary diagnostic capabilities to improve.

In this section, a variety of endoscopic designs currently employed for conventional keyhole surgery from an engineering perspective are assessed. It should be noted that all designs vary in length, from several millimetres to ~50 cm, but all have the unique ability to allow entry into the body via small incisions (~1-20 mm) or cavities.

Rigid Endoscopes

The generic rigid endoscope is composed of a series of lenses, which transmit an image from the distal end of the endoscope to the eyepiece (proximal end), with optical fibres located around their periphery for sample

illumination. Specifically, white-light illumination is achieved by coupling the output from a high intensity source (e.g. a high pressure Xenon arc lamp) to such fibres via a fibre-optic or liquid-filled light guide with high transmission at visible wavelengths.

Collimated rays leaving the eyepiece are, in general, focussed onto a CCD chip by lenses contained within the camera's housing unit. Images are thereafter digitally converted and displayed on high-definition monitors within the operating theatre. Contemporary CCD cameras have the ability to perform intensity-correction post-acquisition and may have adjustable gain and contrast controls for optimal imaging.

I. Traditional Relay-Lens Endoscopy

The traditional relay-lens endoscope is composed of a series of one or more optical systems, each of which transmits an inverted image to the next with a magnification of unity [37]. Figure 4 illustrates a typical ray trace of light passing through a single relay system.

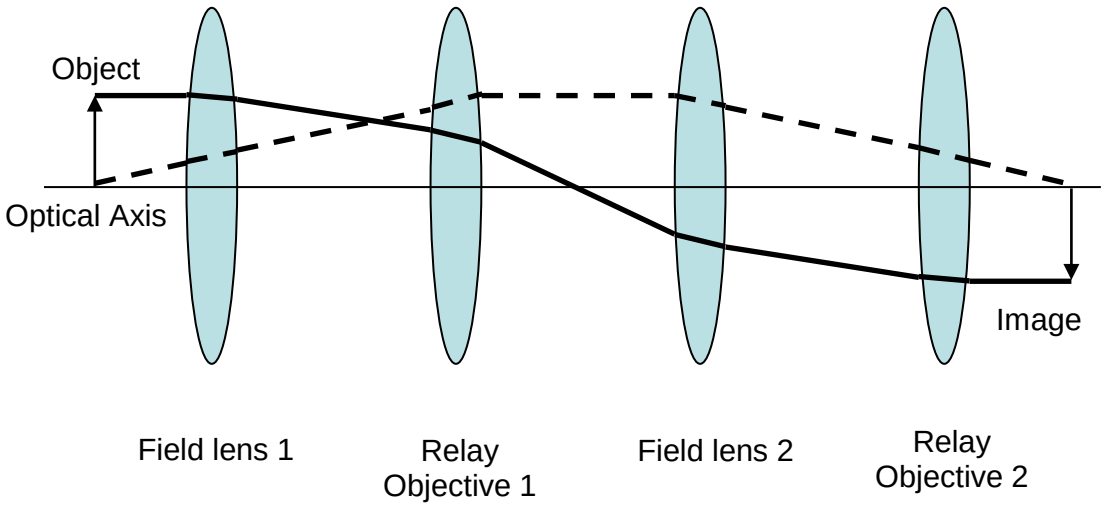

Figure 4. Ray diagram of one of three to five relay systems found in the traditional relay-lens endoscope.

The ray indicated by the dashed line is collimated after passing through field lens 1 and relay objective 1. Conversely, the ray represented by the bold line is collimated external to the relay system after leaving the second relay objective. Conventional systems rely on thin biconvex lenses with each system telecentric in both object and image space. In other words, the entrance and exit pupils associated with each system are placed at infinity.

Traditional relay-lens endoscopes consist of a chain of between three and five relay systems with diameters ranging from 3 - 7 mm. In simplified form, the role of the relay system is to transmit an image from one location to another with minimal chromatic aberrations. In order to assess the suitability of a relay objective to a particular field lens, one must deduce the Lagrange Invariant Constant, L, of both. This can be achieved via the expression

$$L = ny\theta \qquad (1)$$

An objective lens of known numerical aperture and aperture angle, θ, produces an image with a height, y, with respect to the optical axis in a medium of refractive index, n. Any field lens utilized for relay imaging must subsequently have the same Lagrange Invariant.

In order to asses the way in which chromatic aberrations are transferred through a relay system, it is important to determine the system's axial magnification, α, given a known lateral magnification m.

$$\alpha = m^2 \qquad (2)$$

A system which has a lateral magnification of unity therefore has an axial magnification of the same value. In such a scenario, the system is symmetric, and has the advantage of removing coma, distortion and lateral chromatic aberrations by default.

From an engineering perspective, the ideal relay-lens endoscope will have as few relay systems and cemented components as possible in order to avoid optical losses as rays propagate through refractive index boundaries. Additionally, an image field of low curvature is favourable in order to produce a high quality image.

II. Hopkins Rod-Lens Endoscopy

The Hopkins Rod-Lens endoscope revolutionized endoscopy by replacing the free space between field and objective lenses with glass rods. The number of glass-air refractive index boundaries decreased and fewer optical surfaces were necessary. As a direct consequence, light transmission improved significantly and imaging within the operating theatre could be performed with relative ease.

The Hopkins lens relay system consists of two quartz rods mounted concentrically along an optical axis with an air gap between them, forming an air-lens (Figure 6).

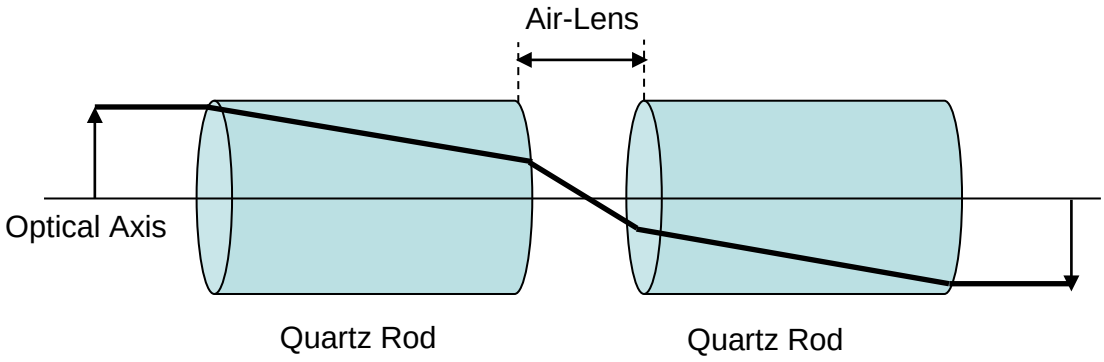

Figure 6. The Hopkins lens relay system used in conventional endoscopy is composed of glass rod lenses separated by an air gap.

By replacing the air gaps (n = 1) between lenses in a traditional lens assembly (Figure 5) with glass rods (n ≈ 1.5), a significant increase in light transmission is realized due to a rise in refractive index. Light transmission is directly proportional to the square of the refractive index through which the light rays traverse, allowing the Hopkins system to have a higher degree of throughput. Additionally, the rods do not require stopping down – a process in which the iris of a lens is reduced in order to increase the depth of field seen at the image plane. Thus, the diameter of Hopkins relay systems can be as small as ~1 mm, allowing endoscopes of various diameters to be produced for a range of applications [38]. Upon comparison to a traditional lens relay system of the same diameter, the Hopkins rod-lens system can achieve a factor of nine times greater optical transmission. However, the inherent design of Hopkins' original optical system may result in astigmatism and field curvature, reducing the off-axis image quality. Utilizing shorter glass rods within the air gaps was shown to correct such abnormalities [39], but with extra elements added to the system, manufacturing costs inevitably increased.

Dobson realized that a new relay stage composed of two identical rod lenses located equidistant from the aperture stop reduces coma, distortion and transverse chromatic aberrations [40]. Consequently an optical design capable of correcting on- and off-axis spherical aberrations as well as astigmatism and field curvature was developed. Each new rod lens consisted of a field lens and relay objective attached to opposite ends of the glass rod in such a way that the overall component has a tangential field (Figure 7).

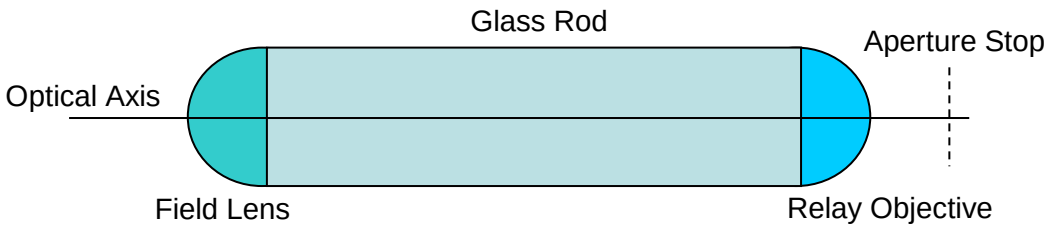

Figure 7. Form of the rod-lens proposed by Dobson to reduce both on- and off-axis aberrations.

Each rod lens has the best form of correction when the image is formed on a flat plane, occurring when

$$S_A = -\frac{S_P}{3} \qquad (3)$$

where S_A and S_P are the Siedel sums representing astigmatism and Petzval field curvature respectively. Given that the field lens has a high refractive index (~1.7) such that $(S_A)_{\text{field-lens}}$ and $(S_P)_{\text{field-lens}}$ become small, $(S_P)_{\text{rod-lens}}$ can be deduced if the approximation

$$(S_P)_{Objective} \approx 0.6H^2K \qquad (4)$$

is made, where H represents the Helmholtz-Lagrange invariant and K is the power of the relay objective. If $(S_P)_{rod\text{-}lens}$ is chosen such that each rod lens, and subsequently each relay system, has a flat tangential field, then $(S_P)_{objective}$ and $(S_P)_{glass\text{-}rod}$ are deduced, the latter from its paraxial ray variables, refractive index and length. As a result, thin field and relay objective lenses can be calculated to produce a rod-lens, and therefore a relay system, with a flat tangential field and improved image quality may be developed.

As a direct consequence of the introduction of Hopkins lens relay systems to endoscopy, light transmission through an endoscopic system may increase significantly, images are sharper with improved contrast and resolution, and wider fields of view are achievable. Additionally, the system reduces darkening of off-axis images, ultimately resulting in reduced vignetting. Fewer relay systems are required, and endoscope diameters down to ~1 mm are commercially available [41]. Diagnostic surgical procedures employing Hopkins-lens endoscopy have improved as a result, rendering the Hopkins rod-lens as one of the major advances in the field of optical engineering.

Flexible Endoscopes

I. Fibre Optic Image Guiding Endoscopy

Flexible fibre-optic based endoscopes are among the most common types used in keyhole surgery today, particularly in the field of diagnostics. Their unique ability to transmit images over relatively long distances (upwards of 60 cm) and around bends has proved exceptionally useful for viewing and

treating regions contained within the rectum and gastrointestinal tract [42, 43]. Such devices are based on the use of coherent fibre bundles, i.e. where the fibres are aligned at both the input and output ends. The fibres are based on a step-index structure, and couple light, with minimal optical loss, from the endoscope's distal end to the eyepiece, providing surgeons with a technique capable of observing anatomical structures which would only otherwise be observed during open surgery.

When light propagating in a medium of high refractive index n_1 (e.g. the core of an optical fibre) strikes the surface of a medium with low refractive index n_2 (e.g. the cladding of an optical fibre), there exists a critical angle of incidence, θ_c, above which the rays are totally internally reflected, rather than refracted, at the boundary (Figure 8). Total internal reflection is favourable when the ratio n_2/n_1 is less than unity and for angles of incidence greater than θ_c, where

$$\theta_c = \sin^{-1}\left(\frac{n_2}{n_1}\right) \qquad (5)$$

For angles of incidence below the critical angle, rays are refracted at the index boundary and propagates through the low index medium and out of the fibre,

with an angle of refraction governed by Snell's Law.

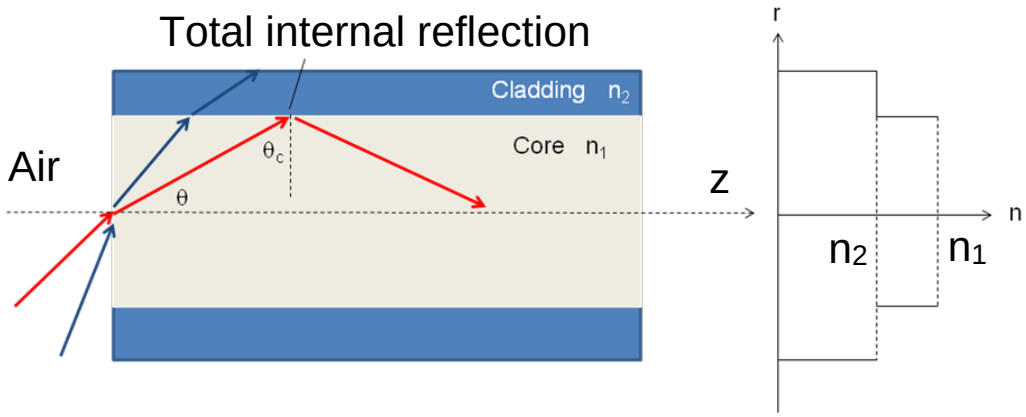

Figure 8. Light rays propagating in the core of an optical fibre at an angle θ relative to the z-axis, are subject to total internal reflection at the boundary between the core of high refractive index and the cladding of low refractive index if the angle at which the rays strike the cladding is equal to or larger than the critical angle (red trace). If the angle of incidence is smaller than the critical angle, the ray propagates through the refractive index boundary and out of the low index medium (blue trace).

Equation (5) governs the condition for the maximum numerical aperture, NA_{max}, achievable by the fibre. From the condition of total internal reflection

$$NA_{\max} = \sin(\theta_c) = \frac{n_2}{n_1} \qquad (6)$$

When $\theta = 90^o - \theta_c$,

$$NA_{\max} = n_1 \cos(\theta_c) = n_1\sqrt{1-\sin^2(\theta_c)} = n_1\sqrt{1-\left(\frac{n_2}{n_1}\right)^2} = \sqrt{\left(n_1^2 - n_2^2\right)} \qquad (7)$$

A typical flexible endoscope is composed of ~10^5 quartz fibres, each of which has a core and cladding of refractive indices 1.475 and 1.460 respectively, and an outer diameter in the range of 5-10 μm. The resolving

power of the endoscope is determined by the formation of the fibres within the bundle which guides the image, and therefore, by the total number of fibres.

1.5 Fluorescence

When a photon of wavelength λ_1 is incident upon the surface of certain molecules, there exists a finite probability that the photon will be absorbed. If absorption is favourable then a finite probability that the molecule will emit a photon of longer wavelength, λ_2, (photoluminescence) due to the process of fluorescence exists [44].

Fluorescence is the emission produced when a molecule relaxes from its excited singlet-state back to its lowest energy level (ground state) after initial excitation by an incoming photon. The fluorescent molecule, in general, absorbs a high energy (short wavelength) photon and emits a lower energy (longer wavelength) photon with emission generally occurring in the visible, ultraviolet and infrared wavelengths (300-750 nm).

1.5.1 The Quantum Mechanical Principle

In quantum mechanics, a spatially confined particle (e.g. an electron in an atom) may only exist in discrete, quantized energy levels: a ground state of minimum energy and higher excited states. Each level is sub-divided into vibrational and rotational components and excitation to upper molecular energy states may take place with optical pumping.

When light radiation of energy $h\upsilon$, where h is Planck's constant and υ is the optical frequency, is incident upon the surface of a molecule, an

electric-dipole allowed singlet-singlet (S_0 to S_1) optical transition may occur if the absorbed photon energy matches the energetic difference between the ground state and one of the vibrational sub-levels of the first excited state. Almost instantaneously after excitation, non-radiative vibrational relaxation occurs, and the excited molecule moves to the lowest sub-level of the first excited state. In this energy configuration, the molecule can relax to one of the vibrational levels of the ground state via the fluorescent emission of a photon but there is also a finite probability that intersystem crossing into a non-fluorescing triplet state, T_1, occurs - a process normally referred to as photoblinking. Following emission of a fluorescence photon, further vibrational relaxation occurs from the upper sub-levels of the ground state, until the molecule reaches its initial energy configuration (Figure 9).

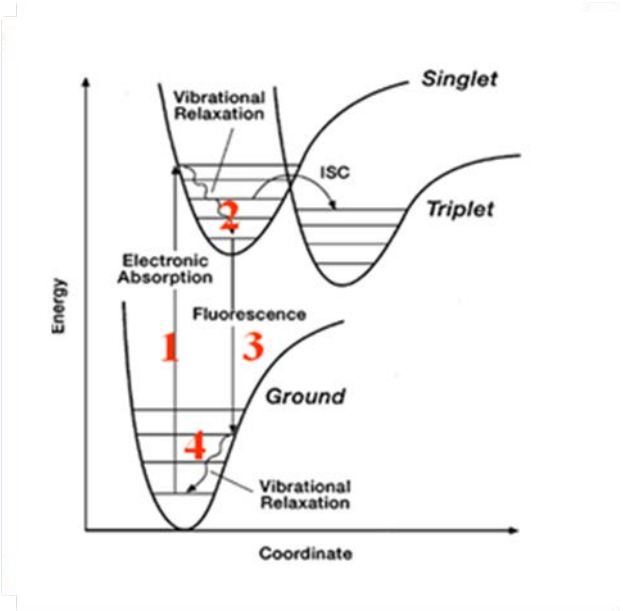

Figure 9 [45]. A photon is absorbed by a molecule providing its energy is equal to the energy difference between one of the upper sub-level of S_1 and the lowest sub-level of S_0 (1). After absorption, the molecule relaxes non-radiatively to the lowest energy sub-level of S_1. (2). When the molecule resides in the lowest energy sub-level of S_1 intersystem crossing into a triplet state T_1 or relaxation to the upper sub-level of S_0 via the emission of a fluorescent photon can occur (3). In the event of fluorescence emission, the molecule returns non-radiatively to its initial energy level in the ground state.

Non-radiative vibrational relaxation stages result in the loss of energy to molecular vibrations and heat, causing a spectral red shift between the absorption and emission wavelengths known as the Stokes Shift. This shift is defined as the difference between the peak absorption and emission wavelengths. The smaller the Stokes shift, the more complex optical elements must be to separate absorption photons from emitted fluorescence photons.

Fluorescence emission takes on a radiative pathway from the excited state back to the ground state, but there are a number of other competing processes that can take place as an alternative [46]. These include internal conversion (non-radiative relaxation from upper to lower energy states), intersystem crossing (non-radiative decay from an upper singlet state to a non-fluorescing triplet state) and quenching (any process which decreases the probability of the excited molecule returning to the ground state via fluorescence emission).

1.6 Fluorophores

Upon excitation of light with an appropriate wavelength, fluorophores may best be described as the functional entities of a molecule which emit fluorescence photons, the intensity and wavelength of which is critically dependent upon its chemical composition, structure and local environment. Many are naturally occurring, but most have been engineered for the specific labelling of proteins, DNA, RNA and lipid membranes for a variety of single-molecule, micro- and macroscopic studies.

Fluorophores may be classified by their emission and binding properties. Those which emit a wavelength λ_1 in healthy cells and $\lambda_2 \neq \lambda_1$ in

diseased cells are defined as non-specific. Targeted fluorophores bind to specific entities from which high signal-to-noise ratios (SNRs) can be achieved if high affinities between the fluorophores and its target exist. Activatable fluorophores are defined as those which have the ability to couple strongly to each other. The very act of doing so quenches fluorescence emission, but this may be recoverable via enzyme-mediated cleavage. Increased SNRs are achievable in this instance since little background is detected in the quenched state and over time, enzymes may cleave multiple probes, allowing the fluorescence signal to amplify. The effectiveness of a fluorophore for a particular application critically depends on a number of limiting factors. First, the dye-target ratio has to be carefully controlled as it may affect the fluorescence properties of the conjugates and second, labelled antibodies tend to have long plasma half-lives, causing long-lasting background fluorescence. Additionally, fluorophores may be so large in size that they fail to pass tissue barriers, making their target unobtainable.

1.6.1 The Near-Infrared Window

Fluorophores are proving to be vital in the quest to reveal otherwise unobtainable biological information from living cells and animals [47]. Their fluorescence signals have revolutionized optical readout modalities, particularly microscopy, and are providing new opportunities at the interface between physics and the life sciences [48]. Molecules associated with disease can be tracked and their optical properties examined in a variety of environmental conditions. The advantages of fluorescence are however entirely dependent on the construction of a suitable fluorophore for application

of the biological sample of interest and despite their importance for studying disease mechanisms, little is known about how to rationally design those with optimum properties. Additionally, fluorophores which emit in the visible portion of the electromagnetic spectrum (~400-700 nm) have limited use in samples which are relatively large and opaque nor in applications in which penetration into tissue is required.

The development of fluorophores which emit at NIR wavelengths (650-900 nm) have extended their utility *in vivo*, allowing depth penetration to be achieved because mammalian tissue is less opaque at such wavelengths. Emission below 650 nm does not penetrate deeply through tissue due to scattering and the presence of endogenous absorbers and lipids. At NIR wavelengths however, the absorption coefficients of the absorbers are low, and in conjunction with optical scattering in tissue being proportional to λ^{-4}, NIR photons may penetrate further. However, at wavelengths >900 nm, imaging detectors can become complex and expensive, resulting in a wavelength window of opportunity (650-900 nm) in which deep imaging is optically and practically possible (Figure 10).

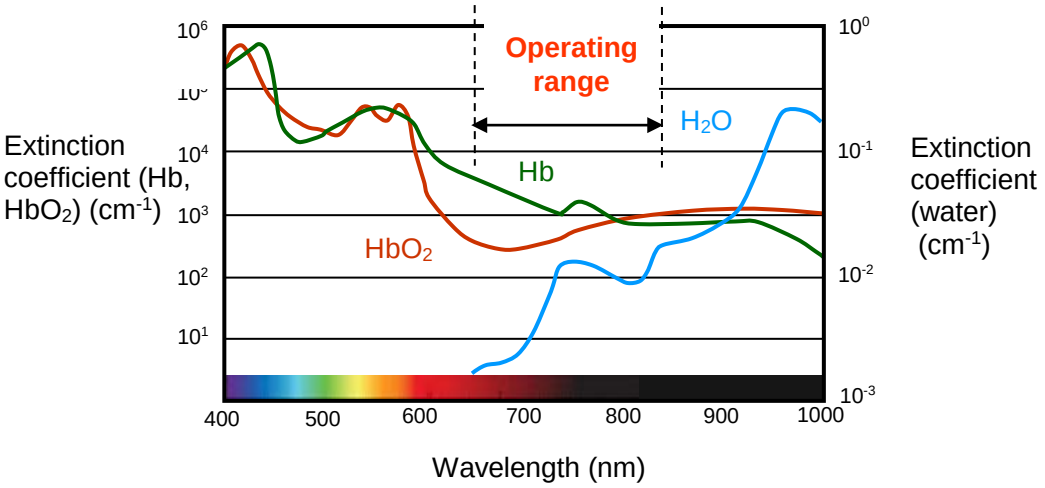

Figure 10. The absorption (extinction) coefficients of haemoglobin, Hb, oxyhaemoglobin, HbO_2 and water, H_2O, are low at near infrared wavelengths. In parallel with reduced scattering, photons at such wavelengths may penetrate further in tissue, allowing imaging to be achieved at greater penetration depths upon comparison with conventional imaging.

In order to fully comprehend the molecular dynamics which underpin mammalian biology and disease, one requires the ability to examine cellular and molecular functions noninvasively and *in vivo*. Many contemporary imaging procedures rely on fluorophores which emit visible wavelengths [49, 50] but the introduction of near-infrared emitting fluorophores is allowing images within tissue structures to be examined with reduced autofluorescence, and several have already been introduced into the clinic.

The ideal fluorescent marker should be highly efficient with a high quantum yield and exhibit little or no photobleaching. Strong fluorescence emission in the near-infrared is desirable and the fluorescence spectra should be stable over a range of pH values and tissue oxygenation (redox) states. In addition, the fluorophore should be non-toxic to its host and must have the ability to bind to the region of interest with ease. Research into the design of near-infrared fluorophores with optimum properties is still in its infancy, but

their very existence has been shown to revolutionize studies in living cells. In particular, NIR fluorescence imaging can be performed over a variety of resolutions ranging from the microscopic detection of subcellular objects to the macroscopic anatomy of anaesthetised mice [51] with a sensitivity capable of revealing complex biological dynamics as they occur deep in living tissue.

1.6.2 Examples of NIR Fluorophores

i. Protoporphyrin IX

Protoporphyrin IX is induced by application of 5-ALA either topically or systematically to tissue. With a peak excitation wavelength of around 400 nm and peak fluorescence emission wavelength of 630 nm, PpIX offers an opportunity to exploit the tissue transparency window by emitting in the NIR (Figure 11).

When 5-ALA is injected intradermally into the vicinity of a tumour, cells may become photosensitised by the formation and accretion of endogenous PpIX on their surface. 5-ALA is an intermediary substance in the synthesis of haem, with PpIX formation being the final stage before iron is introduced and haem is produced. When occupying its ground state, PpIX exists as a singlet, S_0, with zero spin and D_{2h} symmetry.

As a consequence of the enzymatic differences between cancerous and normal cells, PpIX accumulates within tumour tissue [52, 53, 54] since its conversion into heme is slow. As a result, cancerous tissue may be differentiated from normal tissue by, for example, fluorescence endoscopy

[55, 56]. Regions of tissue in which fluorescence is visible suggests the presence of cancerous cells.

The factors which cause the biosynthesis and accumulation of PpIX in cancerous cells are not entirely understood but reports do suggest cancerous cells and tumour tissue accumulate significantly more PpIX than normal tissue [57]. In particular, cancerous cells in the blood, plasma and the serum, have been observed via fluorescence spectroscopy [58, 59], prompting clinical trials for a fluorometric method for tumor diagnosis. Additionally, Kriegmair *et al*. used PpIX fluorescence for the earlier detection of bladder cancer [60]. The spectral ratio of fluorescence from PpIX can be used to examine the level of metabolism of cancer in humans and animals since the intensity depends linearly on the concentration of fluorescent matter. One such study successfully showed that the fluorescence intensity from PpIX from plasma in tumour-implanted mice could be used to estimate the metabolism and stage of tumor development [61].

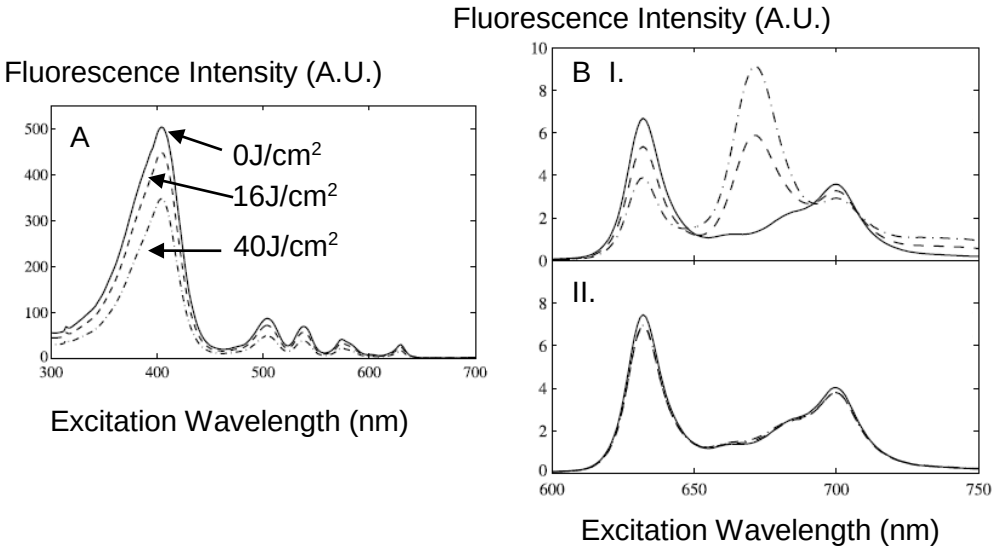

Figure 11. Adapted from [62]. A. Fluorescence excitation spectra of PpIX as a function of light exposure. B. (I) Fluorescence excitation spectra of PpIX as a function of light exposure in the

presence of air. (II) Fluorescence excitation spectra of PpIX as a function of light exposure in the presence of a deoxygenated sample.

Although the emission wavelengths of PpIX are appropriate for deep tissue work, the fact that blue light is used to excite the dye severely limits the depth at which it can be excited.

II. Indocyanine Green

Indocyanine green (ICG) (Figure 12) is clinically approved as a non-specific fluorescent probe for examining hepatic blood flow and function, pulmonary artery and aortic flow and has been used in ophthalmologic fluorescence angiography for allowing choroidal vascular structures to be visualized [63, 64, 65]. Tajima *et al.* have recently reported the use of ICG for sentinel node mapping in cases of gastric cancers and suggest that it may provide a useful tool for determining the metastatic status of lymph nodes, particularly in cases with cT1-stage cancer [66]. For such applications, ICG becomes favourable since low background images are obtained rapidly after injection and the dye is promptly excreted from the blood. Its non-linear fluorescence and high albumin binding have however proved to be problematic for a selection of fluorescence applications. In addition, bioavailability reduces with ICG use but research is ongoing to synthesise by-products with improved spectral and binding properties.

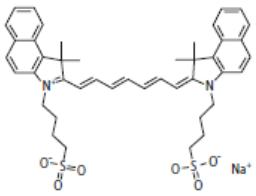

Figure 12. [67] The molecular structure of ICG.

ICG has an excitation wavelength of 800 nm, near the isobestic point of Hb and HbO_2. This results in a maximum fluorescence peak of 840 nm when fully bound to plasma proteins, including high- and low-density lipoproteins. In water however, the excitation wavelength that results in maximum fluorescence reduces to 700 nm when used in high concentrations and 780 nm when used in low concentrations (Figure 13).

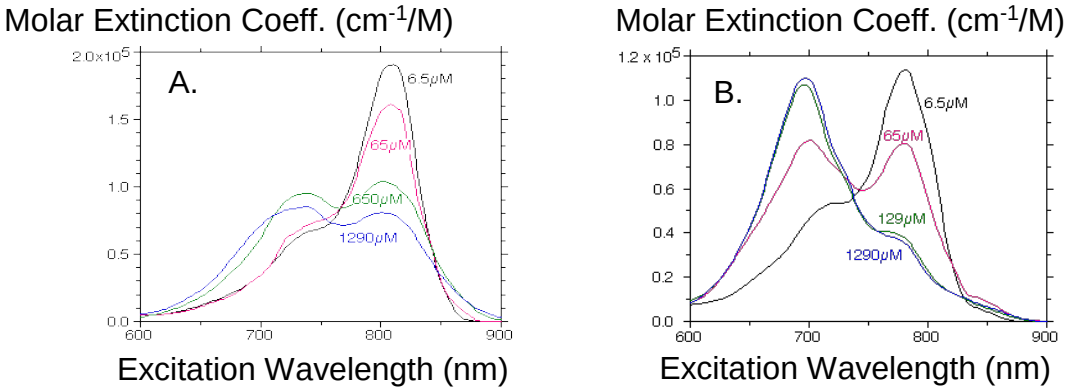

Figure 13. Adapted from [67]. A. Absorption spectrum of ICG in plasma as a function of concentration. B. Absorption spectrum of ICG in water as a function of concentration.

Consequently, ICG fluorescence does not follow the Beer-Lambert law suggesting that lymph nodes receiving ICG drainage may appear with varying fluorescence wavelengths. However, with low toxicity and the ability to undergo rapid excretion into the bile, ICG is the favoured staining agent for the dye-guided method for sentinel node mapping. However, the due

photphysics are complex and optimal choice of excitation and emission wavelength bands is not straightforward; moreover these vary under different environmental conditions.

iii. Methylene Blue

Methylene blue is a member of the triphenylmethane acid dyes and can be used as a fluorescent probe in conjunction with biological staining. Originally introduced as a cheaper alternative to Isosulfan blue [68], it reduces complications due to hypersensitivity reactions [69] upon injection and has been described as a dye capable of improving sentinel node mapping by the dye-guided method [70, 71]. After injection, temporary side effects including blue discolouration of the skin around the injection site and darkening of the urine and stool [72] have been observed.

Many studies report that methylene blue should be used in conjunction with the radio-guided method to improve sentinel node identification rates, particularly with respect to breast cancer [73, 74], with the combination of both likely to result in a 0-11% improvement to sentinel node mapping compared to the dye guided method alone [75]. However, sentinel node detection via injection of a radio tracer is likely to increase surgical costs as well as pre- and post-operative preparation times, and may impose the threat of radiation exposure to those handling extracted nodes [76]. It would therefore appear that the use of methylene blue in combination with the radio-guided method results in a high price to pay for a potentially small improvement that has yet to be justified extensively in the literature.

Methylene blue has a broad absorption spectrum spanning UV to IR wavelengths and produces NIR fluorescence (600 - 780 nm) when excited between 550 and 650 nm (Figure 14) [77]. It therefore becomes feasible to employ the use of methylene blue as a staining agent and a NIR fluorescent marker for the identification of lymph nodes *in vivo.*

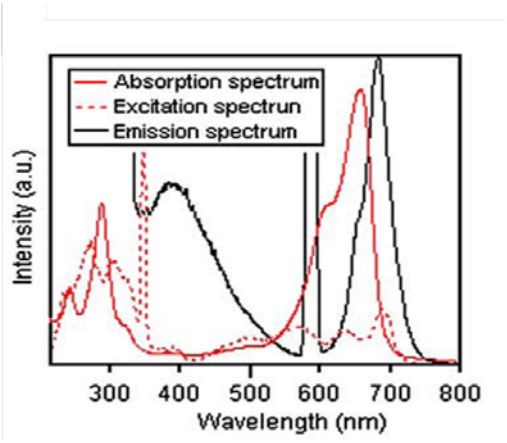

Figure 14 [adapted from 77]. Optical properties of methylene blue solution. The red solid curve indicates the absorption spectrum and the black solid curve highlights the fluorescence emission. The dashed curve displays the excitation spectra of methylene blue dissolved in phosphate buffer solution (167.15μM, pH 7.2).

1.7 Chapter Summary

The dye- and radio-guided methods for sentinel lymph node mapping are recommended for a variety of applications, most notably for sentinel node mapping in breast cancer. However, a declining marginal benefit of using each one in isolation has been observed. Instead, it seems plausible that the use of NIR fluorescent dyes including methylene blue and indocyanine green will combine the advantages of the dye-guided method with a technique capable of reaching greater penetration depths in tissue, revealing otherwise indistinguishable nodes underneath layers of fat tissue.

The use of near-infrared fluorophores in conjunction with optical imaging techniques are allowing sensitive detection of vascular structures surrounded by layers of mammalian tissue *in vivo*. Although additional research is needed in both instrumental design and pharmacology, it is likely that both will continue to provide the clinical practice with an experimental tool crucial for diagnostic procedures, understanding disease pathophysiology and preclinical drug development.

Chapter 2

Development of a Spectrally-Agile Fluorescence Imaging System for Sentinel Node Mapping During Laparoscopic Surgery.

A major obstacle in the quest to develop practical spectral laparoscopy is the use of complicated bulk optics to transmit NIR excitation to, and return colour and NIR fluorescence images from, a conventional laparoscope. In this chapter, specific elements and approaches towards the development of a spectrally-agile endoscopic fluorescence acquisition system are discussed. In particular, three distinct components are described: a tuneable excitation source for the delivery of visible illumination and excitation light to a laparoscope, an optical image splitter capable of separating NIR and visible wavelengths with minimal distortions and a NIR detection unit which allows discrete NIR wavelength bands to be imaged.

In the following text, design aspects of a radically novel, real-time surgical tool for the identification and metastatic status of sentinel nodes receiving drainage from a primary tumour is discussed. In terms of biomedical research, it is envisaged that this apparatus will assist sentinel node mapping procedures in gynaecological, abdominal and colorectal cancers, and may reduce the need for surgical biopsy.

2.1 The System Challenges

Conventional sentinel node mapping techniques rely on clinically approved dyes for use in reflectance imaging and illumination methods which are limited to shallow penetration depths. The use of NIR illumination offers enhanced penetration depths and the potential to locate nodes below overlying tissue layers, improving specificity. By employing the use of a laparoscope with spectrally-agile illumination and detection components, multiple dyes may be used within the laboratory and autofluorescence may be eliminated when searching in deep regions. Specifically, a spectroscopic approach allows the dye environment to be evaluated and differentiation between normal and cancerous tissue to be made.

In terms of imaging, high quality colour images must be preserved during extraction of NIR wavelengths at the eyepiece. Additionally, a methodology of separating discrete NIR wavelength bands for the production of a tuneable imaging device is required. In the latter, high resolution NIR images are not essential since photons from deep tissue layers are subject to scattering, with spatial resolution at the detector decreasing as a function of tissue depth. Crucially however, both colour and NIR images have the requirement to focus on the same field of view. In engineering terms, any system placed at the eyepiece must be small, lightweight and portable such that the ease of use and entry of the laparoscope into the body remains unaffected. The lack of availability of image-separating (flat) dichroics and compact lenses of specific focal lengths does however result in a significant practical limitation.

From an illumination and excitation perspective, conventional white light illumination must be preserved and coupled to high intensity, narrowband, NIR excitation sources. In this section, the design of a modular illumination unit is discussed. This couples white light from a metal-halide (or other) source with that from narrowband NIR laser diodes, while adhering to maximum permissible intensity levels.

2.2 A Practical Solution to Spectral Laparoscopy.

This section reports on a potentially viable solution to practical spectrally-agile fluorescence endoscopy, the experimental arrangement of which is shown in Figure 15.

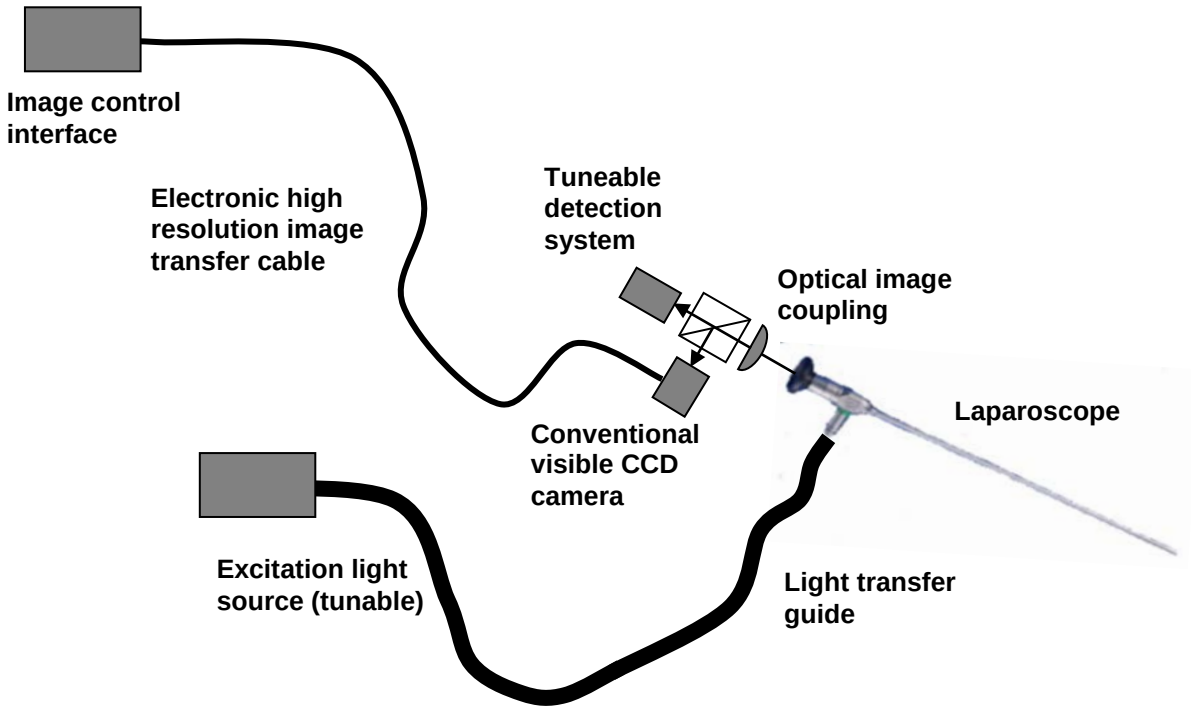

Figure 15. The experimental spectrally-agile endoscopic fluorescence imaging arrangement consists of an optical image splitter which is used to separate visible from near infrared wavelengths. This is coupled to the laparoscope eyepiece, a conventional colour CCD

camera and a tuneable NIR detection system. A tuneable illumination source is achieved by combining a series of NIR laser diodes with a conventional white light source. Excitation and illumination light is subsequently pumped into and through the laparoscope via a fibre-optic light guide.

Conventional white light from a metal halide source is coupled with light from excitation lasers operating at wavelengths of 690 nm, 732 nm, 785 nm and 830 nm respectively to form a tuneable illumination source. Excitation light is focussed into a fibre-optic light transfer guide (NA = 0.59) before being injected into illumination fibres contained within the casing of the laparoscope. This combined source is spectrally agile in the sense that the visible source may be turned off via the insertion of a mechanical shutter controlled by a solenoid and the individual laser sources may be energised individually or multiply, as required.

After illumination, images are transferred to the laparoscope's eyepiece via a series of rod-lens optical relay systems, before entering an electrically insulated optical image splitter. To facilitate ease of use and entry of the laparoscope into internal cavities of the body, the optical image splitter is composed of lightweight and compact optical and mechanical elements. Near infrared wavelengths >662 nm are transmitted by a dichroic mirror whilst visible wavelengths <662 nm are reflected. Transmitted NIR images may either be focussed onto the surface of a NIR-sensitive CCD chip after passing through a NIR transmission filter, or focussed into a low-resolution image transfer guide and transferred to an external detection system. Visible images, which are reflected by the dichroic mirror, are passed through an optical relay system within the image splitter, before being focussed onto a conventional colour CCD chip. A high-resolution electronic image transfer cable

subsequently transfers a digital version of the image to a control interface, from which images may be displayed on high definition monitors within the operating theatre. This visible light detector is the same as would be normally used with a conventional non-fluorescence laparoscope.

2.3 Development of a Spectrally-Agile Excitation Light Source

In conventional laparoscopic procedures, a fibre-optic light guide transfers white light from a metal-halide source directly into illumination fibres contained at the proximal end of the laparoscope. Such fibres are located around the laparoscope optics and are used to guide light via total internal reflection to the laparoscope's distal end. Cavities within the body may subsequently be illuminated, allowing high quality images to be transferred to and viewed at the eyepiece. However, in order to collect NIR fluorescence images from fluorophores such as indocyanine green it becomes necessary to also couple NIR excitation light to conventional white light illumination. In this section, the development of a modular, multi-wavelength excitation system is discussed.

In order to achieve a spectrally-agile method of illumination, white light from a metal halide source (Karl Storz, Germany) is transferred to a liquid light guide (Model 77568, Newport Corp., U.K.) and combined with NIR laser diodes (BWT, Beijing) within an optical coupling unit. Figure 16 illustrates the methodology used.

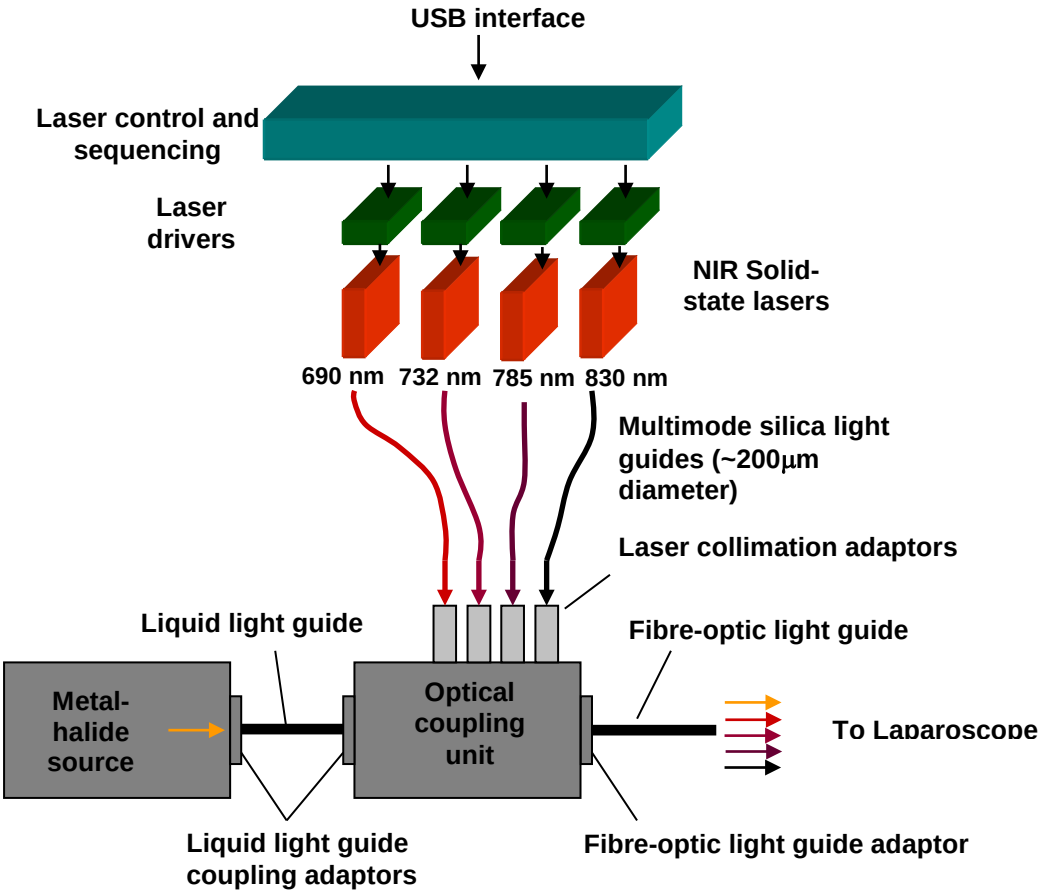

Figure 16. White light from a metal-halide source is transferred by liquid light guide into an optical coupling unit where it is combined with NIR laser diodes. The latter are each controlled via a series of laser drivers and modulated using control software at a USB interface. All wavelengths entering the optical coupling unit are subsequently directed into a fibre-optic light guide before being transferred into illumination fibres situated at the proximal end of the laparoscope.

The liquid light guide (5.1 mm core diameter, 1 m length) is transmissive over the wavelength range 340-800nm and is used to transmit light from the metal-halide source into the optical coupling unit. The guide consists of a plastic tube filled with a transparent, anaerobic, non-toxic fluid which is sealed at both ends with polished fused silica windows and is protected by layers of polyvinyl chloride (PVC). By employing the use of a liquid guide rather than an optical-fibre guide, optical transmission from the

metal-halide source is improved. The liquid light guide is coupled to the metal-halide source with a custom made 51.4 x 1.27 UNF adaptor (Figure 17).

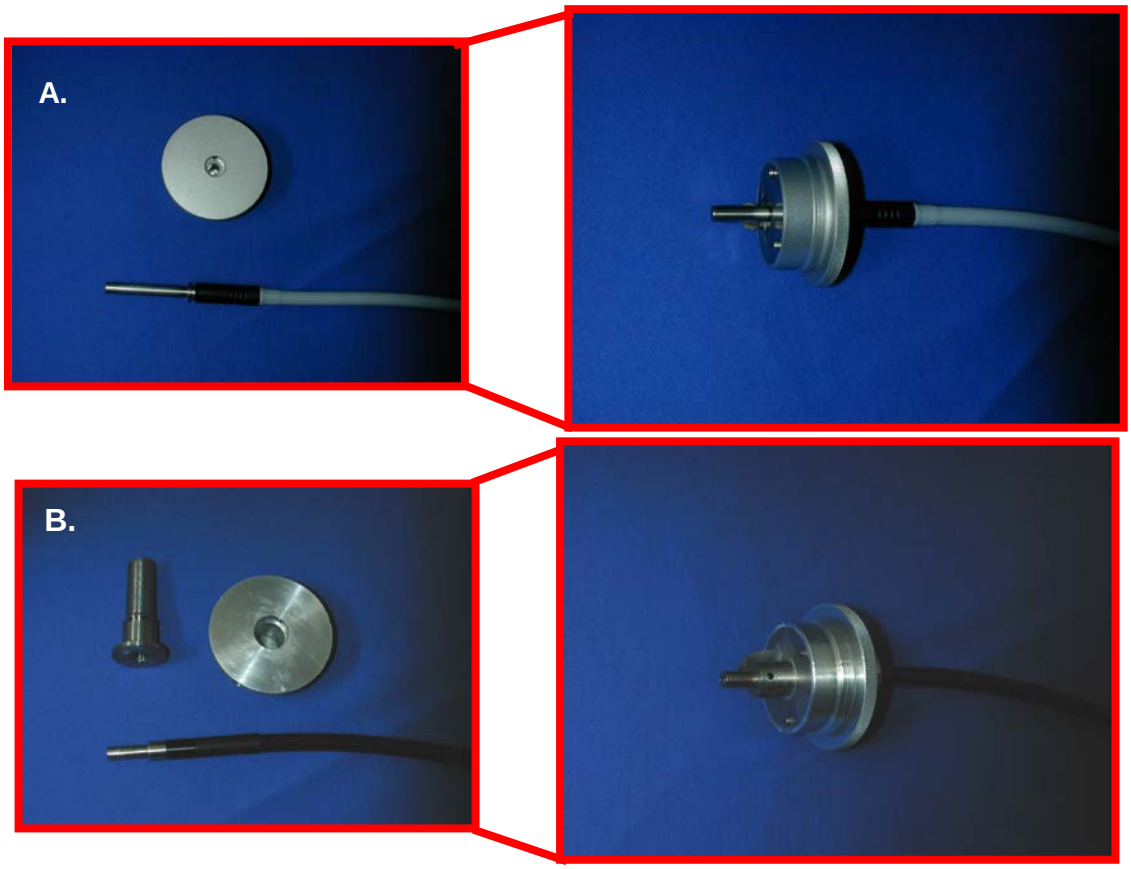

Figure 17. (A): A conventional 51.4 x 1.27 UNF (25.8 mm long, 6.9 mm hole diameter) adaptor used to couple a fibre-optic light guide to a metal-halide source. (B): We have developed a 51.4 x 1.27 UNF (55.4 mm long, 6.9 mm hole diameter) adaptor capable of coupling a 5.1 mm core diameter liquid light guide to the same metal-halide source.

The full-angle at which light may be expected to leave the liquid guide, and propagate into the optical coupling unit, is 72.4^{o}. Upon entering the optical coupling unit (Figure 18), white light is collimated by a 16.5 mm focal length aspheric condenser lens (16AF25, Comar Optics, Cambridge, UK). Thereafter, any NIR wavelengths above 662 nm are removed by the introduction of a dichroic mirror (FF662, Semrock Inc., U.S.A.). Wavelengths below 662 nm are reflected towards a 40 mm focal length NIR-visible coated

double convex lens (NT63-688, Edmund Optics, U.K.) and a 25 mm focal length NIR-visible coated plano-convex lens (NT45-504, Edmund Optics, U.K.) and focussed into a fibre-optic light guide (Karl Storz, Germany) before being transferred to the laparoscopic illumination fibres.

Light from NIR laser diodes (Table 1) is transferred into the optical coupling unit via silica multimode light guides fitted to fibre collimation lenses (FF22OFC, Thorlabs Ltd., U.S.A.), which are in turn mounted to the housing unit containing the optical components. Upon collimation, NIR photons are transmitted by the dichroic mirror and become vertically displaced by ~0.3 mm. Collimated NIR rays leaving the dichroic mirror are subsequently coupled to the fibre-optic light guide by passing through the NIR-visible coated double convex and plano-convex lenses, the combination of which acts as a visible-NIR focussing lens.

A mechanical shutter controlled by a 6V DC, continuous mode solenoid (model 250-1280, RS Components Ltd, Corby, Northants : model 44A-220-621-540 BLP Components Ltd, Suffolk) may be used to remove white-light illumination during NIR laser diode operation.

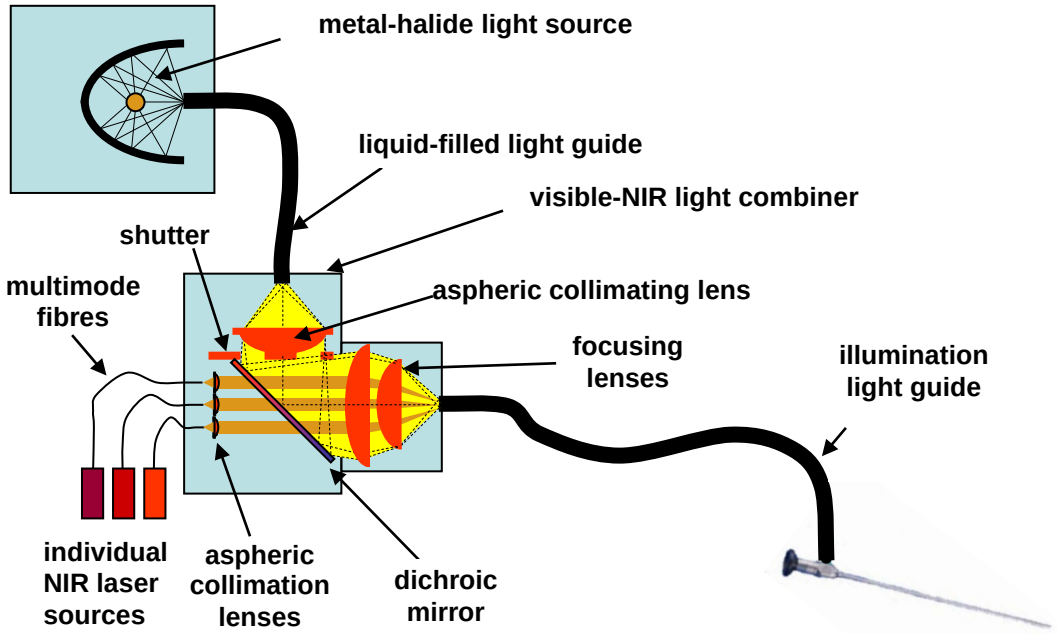

Figure 18. The optical components within the coupling unit are shown. Conventional white-light illumination from a metal halide source is coupled to NIR laser wavelengths and a fibre-optic light guide via a dichroic mirror of edge wavelength 662 nm and a series of NIR-visible coated lenses.

λ(nm)	P(mW)	Δλ(nm)	Laser Operating conditions	Photo-diode operating current
690	800	3.2	2.4 V @ 0.7-1.5 A	91 mA @ 810 mW
732	1600	3.0	1.9 V @ 6-1.9 A	55 mA @ 810 mW
785	1600	6.0	1.85 V @ 0.3-1.9 A	105 mA @ 800 mW
830	1000	6.0	1.66 V @ 0.28-1.2 A	120 mA @ 1000 mW

Table 1. NIR laser diodes with wavelengths ranging from 690-830nm are employed in our setup, each of which has varying operating specifications, bandwidths and output powers.

Each light guide is attached to the overall housing of the light coupling unit via custom made aluminium adaptors. Lenses are held in place with retaining rings and the dichroic mirror is attached to an aluminium mirror

mount via silicon-rubber. Laser collimators are inserted into a back-panel via 11 x 0.5 mm tapped holes. Figures 19 and 20 illustrate the mechanical assembly of the optical coupling unit.

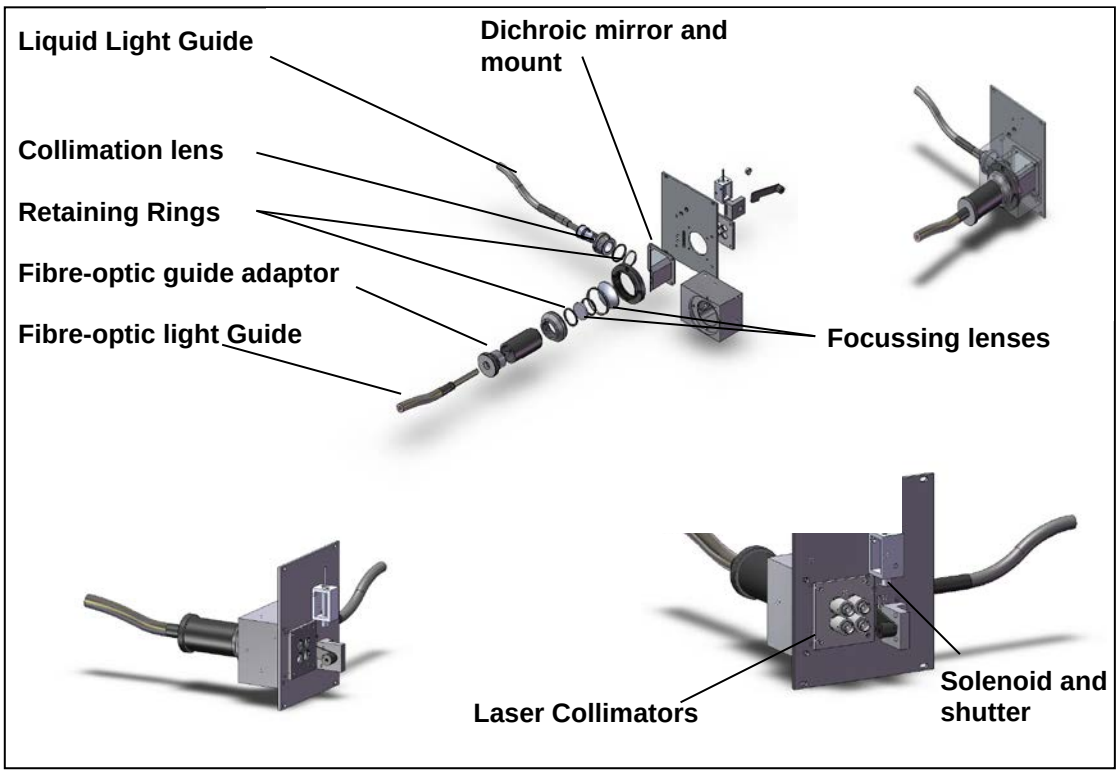

Figure 19. CAD drawings illustrate the mechanical components present in the optical coupling unit.

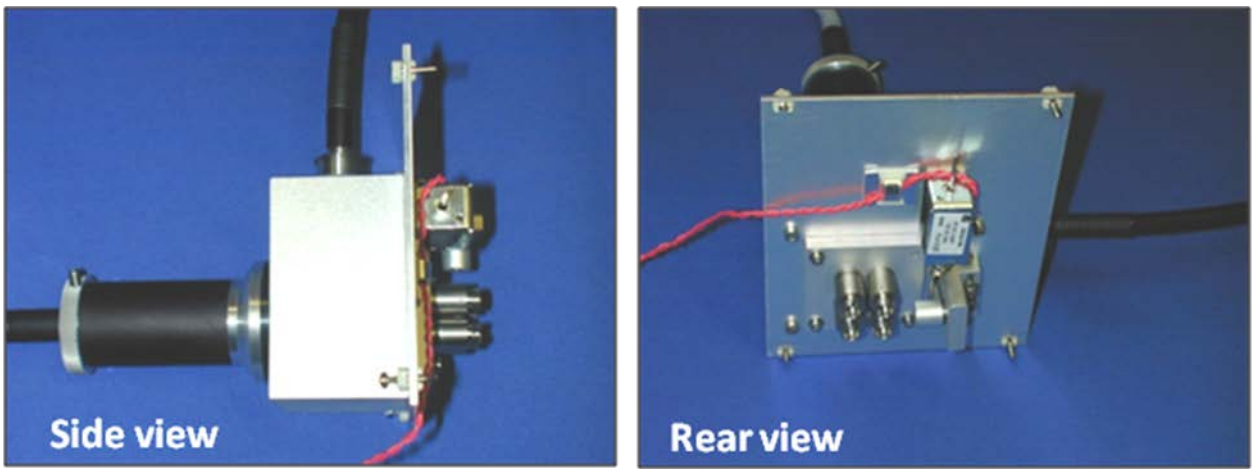

Figure 20. Images of the prototype optical coupling unit.

2.4 Laser Driver Development

Individual NIR laser drivers are mounted to 100 x 160 mm Eurocards containing optical and electrical power monitors as well as Peltier thermoelectric controllers (Figure 21).

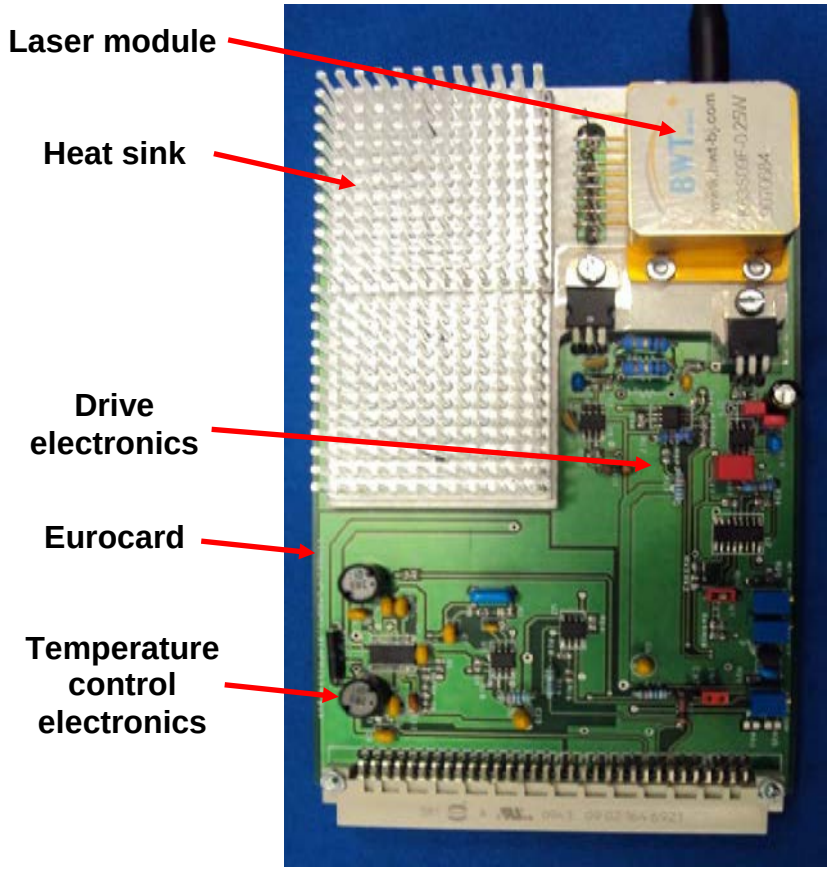

Figure 21. NIR laser diodes are optically and electrically monitored. Cooling of the laser module is achieved by using a Peltier cooling pump mounted within the laser module, with heat removed through a fan-cooled heatsink.

Each laser diode is operated in constant current mode and attached to a power supply of 0-6 V. A switch is incorporated into the circuit to ensure the laser can be modulated (on-off) via software (LabWindows CVI) and a current control allows the intensity of light produced to be adjusted. The greater the

current supplied to the diode, the greater the intensity of light produced. A mechanical interlock is included to allow the user to directly prohibit light emission from a switch on the housing unit in which the Eurocard resides.

Following activation, current flowing towards each laser diode is ramped by a capacitor such that light emission undergoes soft-start operation. The operating current, operating power, optical intensity of emission and temperature associated with the laser are monitored, the latter of which is controlled by a thermoelectric Peltier cooling pump (0-6V) and forced air cooling.

Thermoelectric cooling is achieved by monitoring the temperature of the laser diode using a thermistor, the resistance and voltage across which varies proportionally with the temperature. The voltage produced by the thermistor is compared to that of a desired temperature set by the user such that the difference can be used to determine whether the Peltier cooler situated below the laser diode requires heating or cooling. Simply applying a DC voltage will cause one side of the Peltier cooler to have a lower temperature than the other, allowing heat to be removed from the laser diode. Additional cooling may be achieved via an air fan which draws additional heat from the laser diode towards a heat sink.

All NIR laser diodes (Figure 22) are coupled to multimode fibre-optic guides (NA = 0.22, 105 μm outer diameter) and contained within a modular casing (Figure 23).

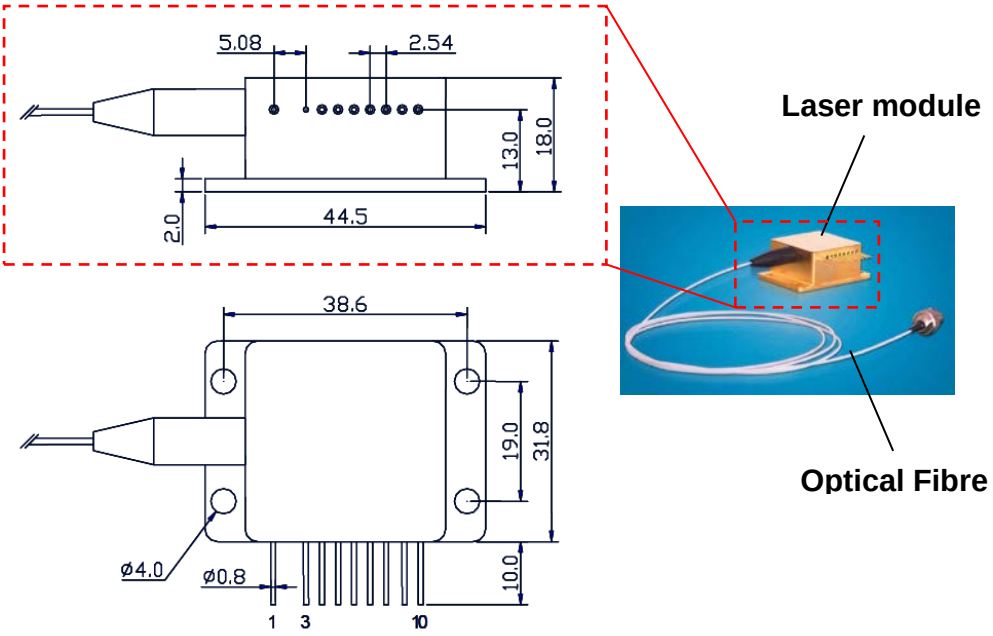

Figure 22. Miniature high power NIR solid state laser modules like the one shown here are used in the development of a tuneable excitation source.

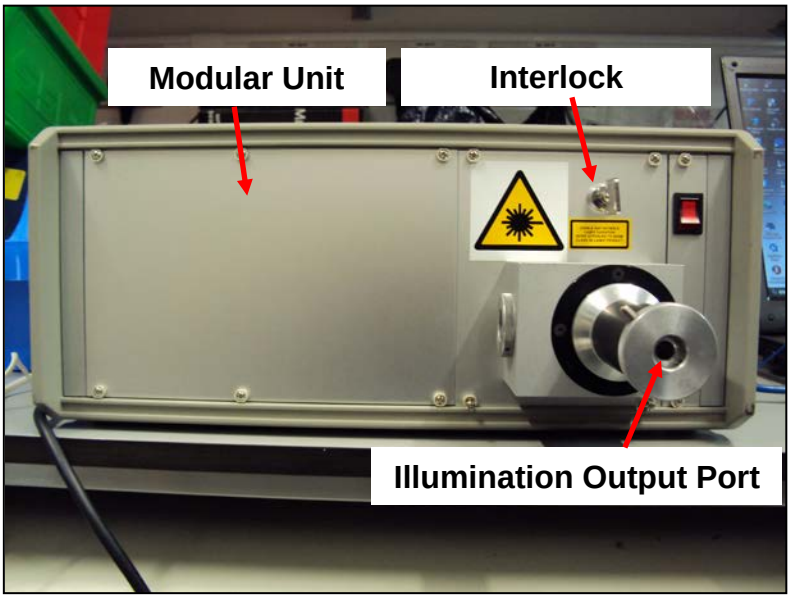

Figure 23. NIR laser diodes mounted to their respective Eurocards are contained within a modular housing unit together with illumination optics.

2.5 Development of a NIR-Visible Optical Image Splitter

Images transferred from the distal to proximal end of the laparoscope are found to exit the eyepiece with a divergence of ±7^{o}. Upon leaving the eyepiece, light enters the optical image splitter through a 12.5 mm diameter, NIR-visible coated fused silica window (NT49-639, Edmund Optics, U.K.) and is split into NIR and visible components via a dichroic mirror with an edge wavelength of 662 nm (FF662, Semrock Inc., U.S.A.). Visible wavelengths below 662 nm are reflected towards a path ultimately ending with a conventional colour CCD camera (Karl Storz, Germany). This visible light path consists of an optical relay system composed of two back-to-back 25 mm focal length finite conjugate micro video lenses (NT54-855, Edmund Optics, U.K.) with a lens-lens air distance of 50 mm. A prism mirror placed 22 mm after the first relay lens folds the rays to ensure that the optical system is compact. The visible image is inverted after leaving the relay system but can be compensated for by inverting the camera direction with respect to normal operation. Visible images with a magnification of unity and field of view comparable to that seen directly through the eyepiece are captured before being digitally converted and transferred to an image control interface (Karl Storz, Germany). Wavelengths above 662 nm are transmitted through the dichroic mirror and can be focussed onto a NIR sensitive detector using different lenses. This detector can consist of one of two arrangements. The first of these consists of a 1/3” (3.6 mm x 4.8 mm x 6 mm diagonal) NIR sensitive CCD chip (DSP 3600, Cohu Inc., U.S.A.) preceded by a 25 mm focal

length lens and appropriate NIR filter. The second type of detector consists of an NIR transmission followed by an 8 mm focal length NIR micro video lens (NT58-847, Edmund Optics, U.K.) which provides an image on the input of a coherent fibre bundle of 1 mm diameter. To employ the use of all coherent fibres, a 6.95 mm focal length lens is necessary, but the nearest commercially available micro video lens is the 8 mm focal length lens as specified. Alternatively, NIR wavelengths may be coupled to a low resolution guide of ~1 mm diameter and transferred to a NIR detector external to the system at the eyepiece. The latter is a likely apparatus for clinical use as it ensures that the optical image splitter is electrically isolated and that the overall system complies with medical electrical safety standards. Figure 24 illustrates the apparatus used in the optical image splitter.

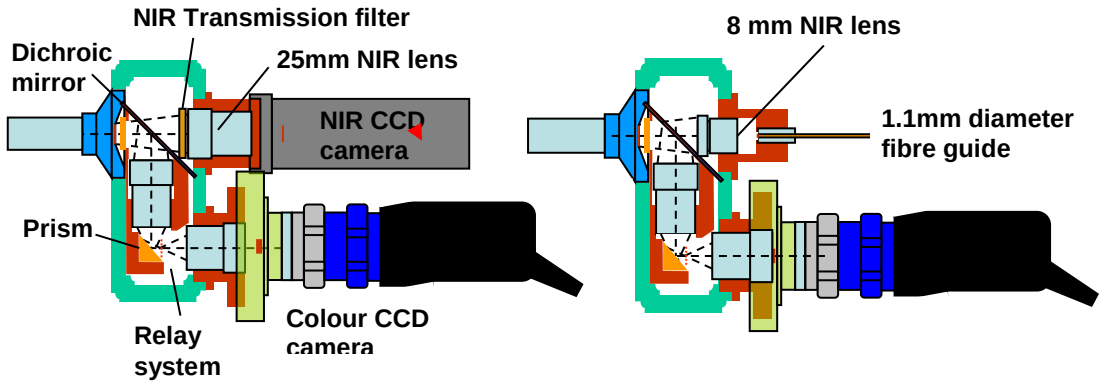

Figure 24. Light leaving the laparoscope eyepiece is split into NIR and visible components via a dichroic mirror with an edge wavelength of 662 nm. The NIR component can be focussed onto a NIR CCD chip after a NIR wavelength band has been selected via a transmission filter (left) , but may in principle be coupled to a low resolution guide and tuneable NIR detector (right). Visible images with a magnification of unity are transferred to a colour CCD chip via an optical relay system consisting of two 25mm focal length lenses. A prism mirror folds the light in order to produce a compact optical system.

NIR wavelengths >662 nm are transmitted by the dichroic mirror. Initially travelling in air ($n_{air} = 1$), and as the near-parallel rays strike the

surface of the 1.1 mm thick fused silica mirror (n_{fs}=1.458) they are refracted by an angle, $\theta_{refraction}$ governed by

$$n_{air}\sin(\theta_{in}) = n_{fs}\sin(\theta_{refraction}) \qquad (8)$$

A ray propagating along the optical axis, at 45º relative to an axis, z, normal to the planar surface of the dichroic mirror, indicated in Figure 25, is refracted by 29º. Subsequently, the ray is vertically displaced by 0.35 mm relative to the optical axis.

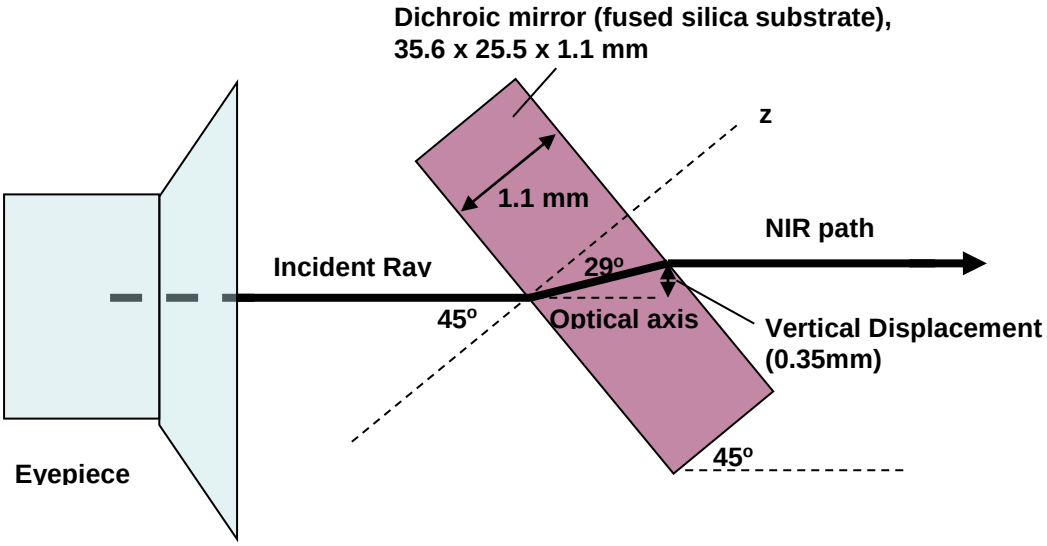

Figure 25. The vertical displacement of a NIR ray propagating along the optical axis and through a fused silica dichroic filter of 1.1 mm thickness is ~0.35 mm.

All optical components are housed within an enclosed anodized aluminium chassis of dimensions 88 x 40 x 37 mm, the thickness of which is determined exclusively by the outer diameter of the eyepiece. Specifically, the dichroic mirror is attached to the surface of an insert at 45º relative to the horizontal. The first visible lens is inserted into the same insert from below the mirror, with its height adjustable via an M16 x 0.5 mm thread. Below, a prism mirror is attached to a flat horizontal surface using silicon-rubber. The

mechanical insert is in turn coupled to the chassis via two M3 x 0.5 mm flathead screws and one M0.25 x 0.45 screw inserted internally. The second relay lens is threaded into a Delrin™ eyepiece custom-made to match the dimensions of the eyepiece on the laparoscope. This eyepiece is in turn threaded to the chassis and allows the conventional colour CCD camera clamp to be attached. The 25 mm NIR micro video lens is coupled to a Delrin™ lens mount (diameter 25.65 mm) which in turn, may be coupled to a NIR CCD chip and threaded to the chassis for laboratory work. The laparoscope eyepiece is attached to the chassis via a clamp threaded to a coupling ring mounted to the outer casing via M3 x 0.5 mm grub screws. Figure 26 illustrates the various mechanical and optical components used in the construction of the optical image splitter.

A. **B.**

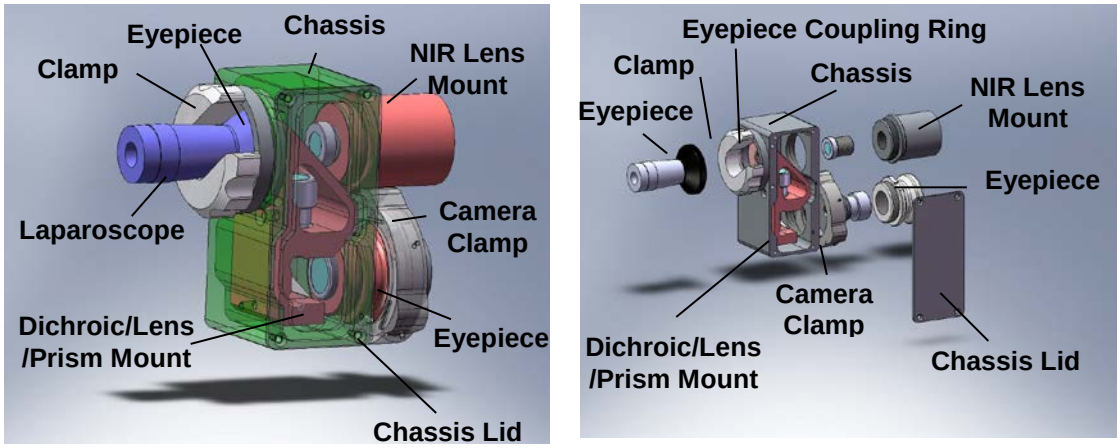

Figure 26. Solidworks™ CAD drawings of the prototype optical image splitter which separates NIR wavelengths from those in the visible. A. Transparent view. B. Exploded view.

The optical image splitter is small, lightweight (~248 g), portable and easily gripped during laparoscopic procedures (Figure 27) without hindering performance and ease of use. In addition, the apparatus is composed of off-

the-shelf optical components, offering an economically viable solution to the problem of separating visible from NIR images. All lenses can be focused by adjusting their relative positions on their respective threads and the overall thickness of the unit is 40 mm - only 2 mm thicker than the diameter of the eyepiece. However, all components within the optical image splitter are small and tolerances are tight. Additionally, by using a prism mirror to make the optical system compact, the image is inverted and subsequently the camera direction with respect to normal operation is reversed. As a result, camera operation must be performed from below.

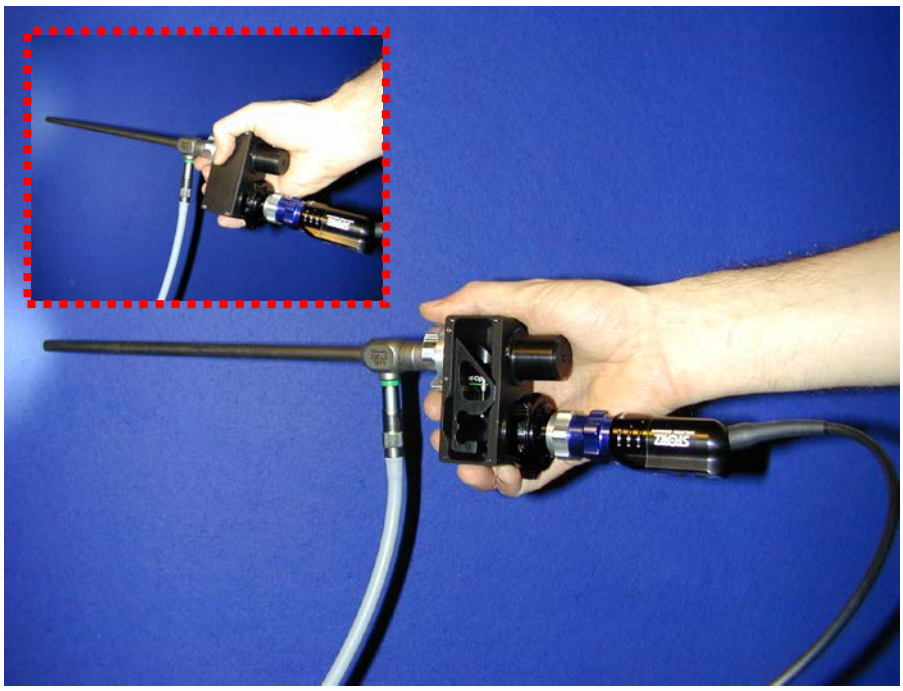

Figure 27. Once attached to the laparoscope, the compact optical image splitter is easily held by the operator during surgery.

Paraxial Arrangement of 1:1 Visible Microlens Relay System

There are many possible configurations of two lenses which satisfy the conditions for a 1:1 image relay system, but each differ in their overall length, L, and field of view, FOV. The paraxial image relay arrangement used within

the optical image splitter is shown in Figure 28. Collimated rays leaving the eyepiece with a spot divergence of ±7º pass through a focussing lens (f = 25 mm) a distance f away from the exit lens of the eyepiece. An inverted image is formed on a plane adjacent to the optical axis with a magnification of -1 before an inverted microlens (f = 25 mm) collimates the rays towards optical components within the colour CCD camera. Rays are subsequently focussed onto a colour CCD chip to produce an image with a magnification of ~1. The insertion of a prism in the final optical image splitter design results in this image being inverted but this may be compensated for with the introduction of a pentaprism in any future designs.

Each microlens has a focal length f = 25 mm and mounting diameter d = 16 mm. The overall length of the relay lens is defined as the distance from the object (eyepiece lens) to the final image plane. Consequently, for an optical relay system in which the object is located a distance *f* in front of the first lens and imaged at a distance *f* after the first lens with a magnification of -1, the overall length is given by

$$L \approx 4f \qquad (9)$$

For our construction, L ≈ 100 mm for the optical image splitter depicted in this section. Given the symmetry of the system, the total magnification at the image plane is unity.

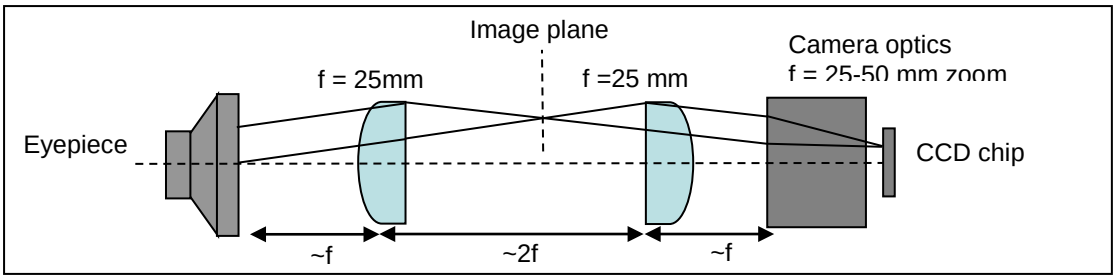

Figure 28 Paraxial layout of 1:1 imaging with a single pair of microlenses, as used within the visible path of the optical image splitter.

2.6. Spectrally-Agile NIR Detection System Designs

Several embodiments of the NIR detection system have been studied, as described in the sections which follow.

i. A detection system based on bandpass and dichroic filters.

Light leaving the laparoscope is separated into visible and NIR bands via an optical image splitter coupled to the eyepiece. Visible images are focussed onto a colour CCD chip before being digitally converted and passed to an imager control interface, from which images on high definition monitors can be displayed. The NIR component is coupled to a low power objective before being transferred to a spectrally agile NIR detector via an image transfer coherent fibre bundle (Figure 29). Light leaving the transfer bundle is coupled to a second low power objective before being subject to a series of dichroic filters, the passbands of which increase incrementally with distance from the objective (Figure 30). This proposed NIR detection method therefore separates NIR light into discrete wavelength bands, each of which is focussed

onto and imaged by a monochrome CCD camera after passing through a local NIR bandpass filter to remove any unwanted wavelengths.

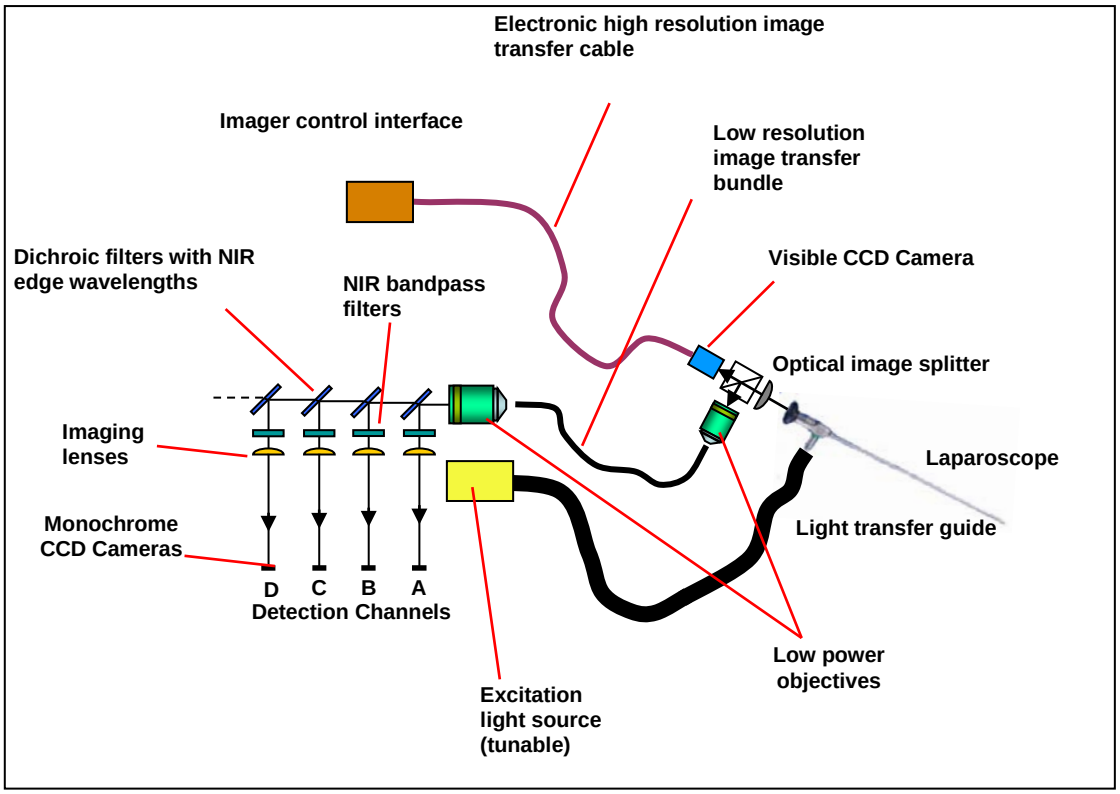

Figure 29. A tuneable detection system based on the separation of NIR light into discrete wavelength bands via dichroic and bandpass filters is shown.

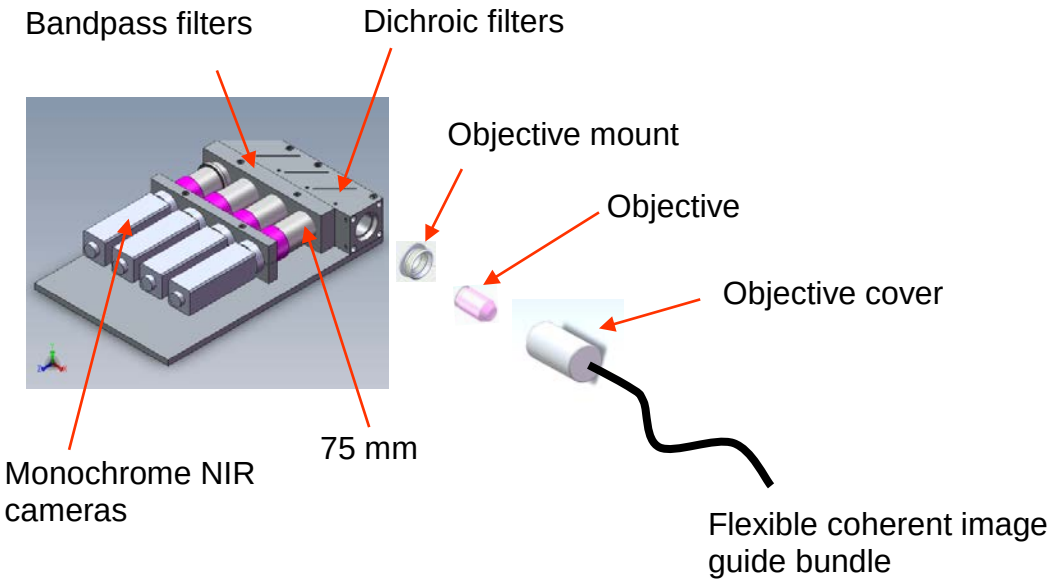

Figure 30. Solidworks™ drawings illustrate a likely setup for a tuneable NIR detector based on dichroic and passband filters. Light leaving a flexible image guide bundle is coupled to a

low power objective lens before being passed through dichroic filters towards monochrome CCD cameras for detection.

Using commercially available components, it is likely that detection channel A would consist of a dichroic filter capable of reflecting light between 662-677 nm whilst passing wavelengths above 677 nm. Similarly, detection channels B, C and D may contain dichroic mirrors with edge wavelengths of 709 nm, 731 nm and 741 nm respectively. Additional detection channels may be introduced, but only with additional costs for further monochrome CCD cameras and filters. Simulations of such setups have been performed using custom-made, in-house software and dichroic transmission data available from corporate websites (Figure 31).

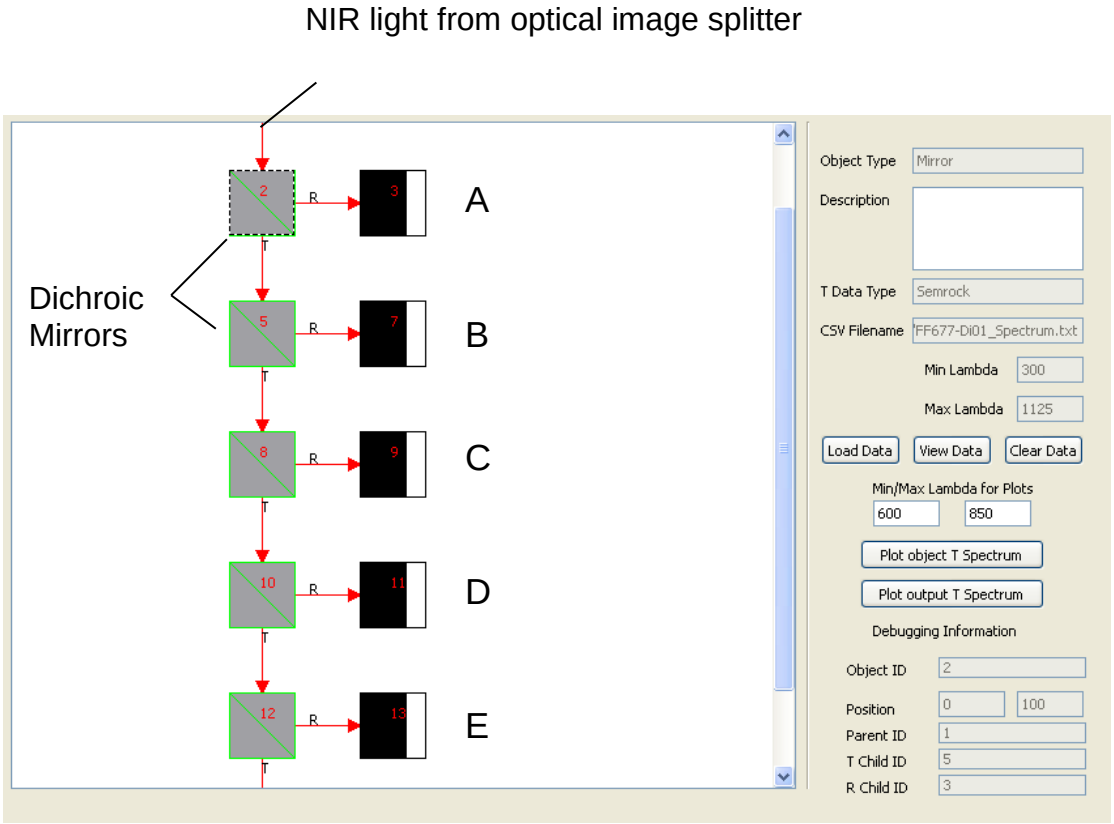

Figure 31. An optical setup containing 5 NIR detection channels has been simulated. Specifically, detection channel A filters NIR light using a dichroic mirror of edge wavelength 677 nm. Detection channels B, C, D and E employ the use of dichroic mirrors with edge wavelengths 709 nm, 731 nm, 741 nm and 801 nm respectively.

In the absence of optical losses, detection channel A receives a NIR wavelength band of 662-677 nm, whilst wavelengths >677 nm are transmitted towards further detection channels. Channel B receives a wavelength band of 697-709 nm while channels C, D and E receive bands of 709-731 nm, 731-741 nm and 741-801 nm respectively (Figure 32).

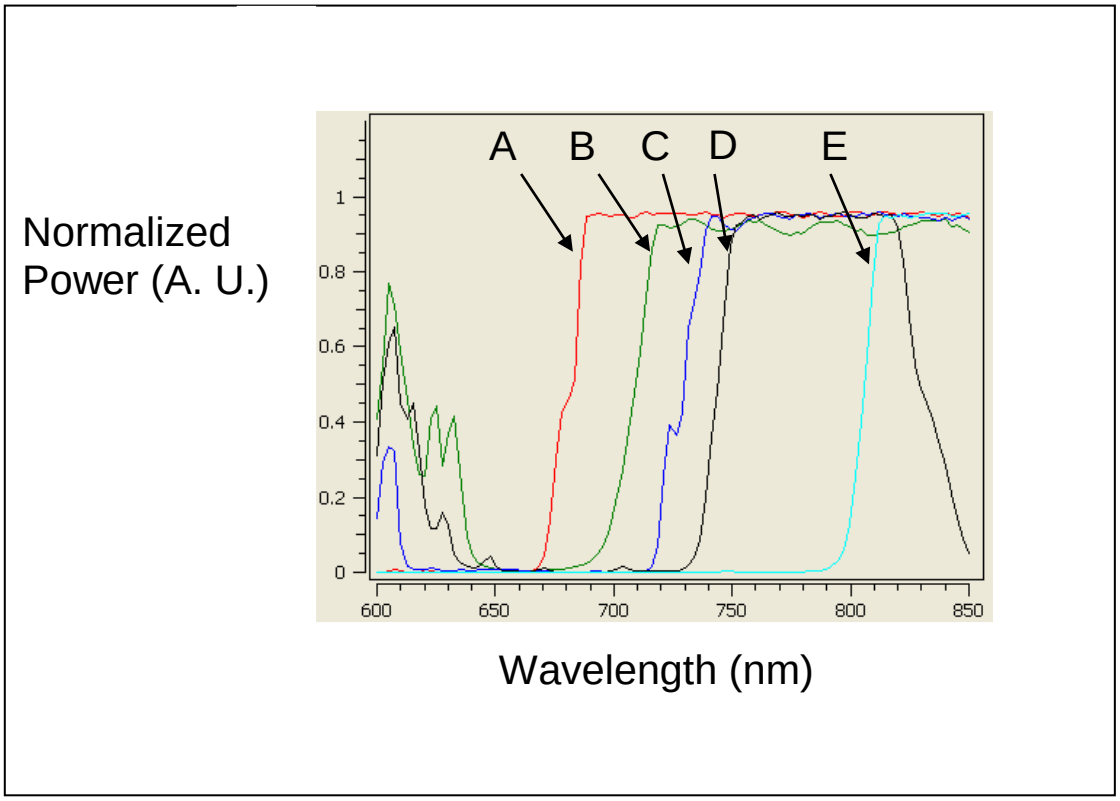

Figure 32. Transmission spectrum of a simulated NIR detector composed of the proposed dichroic filters. The edge wavelength of the dichroic filter used in each channel is indicated.

As the number of detection channels increases more optical components become necessary. Consequently, NIR rays leaving the optical image splitter are subject to additional refractive index boundaries and increased optical losses. In addition, the optical system is likely to result in difficulties with alignment during the construction phase, and may result in a bulky detection system, particularly if a large number of detection channels

are to be incorporated. However, this particular construct removes the need for achromatic optics and provides the user with a flexible imaging system in which all acquisitions, including those obtained by the colour CCD camera, can be performed simultaneously. In addition only a single dichromatic optical splitter is needed at the eyepiece of the laparoscope.

ii. A detection system based on a filter wheel assigned to NIR CCD cameras.

Using a setup similar to that shown in Figure 28 light leaving the laparoscope is separated into visible and NIR bands via an optical image splitter coupled to the eyepiece. Visible images are focussed onto a colour CCD chip before being digitally converted and passed to an imager control interface, from which images on high definition monitors can be displayed. The NIR component is coupled to a flexible light guide via a low power objective before being focussed onto the surface of a NIR sensitive CCD camera. A filter wheel is placed directly in front of the sensor, allowing separate narrow wavelength bands to be imaged sequentially as the filter wheel rotates (Figure 33).

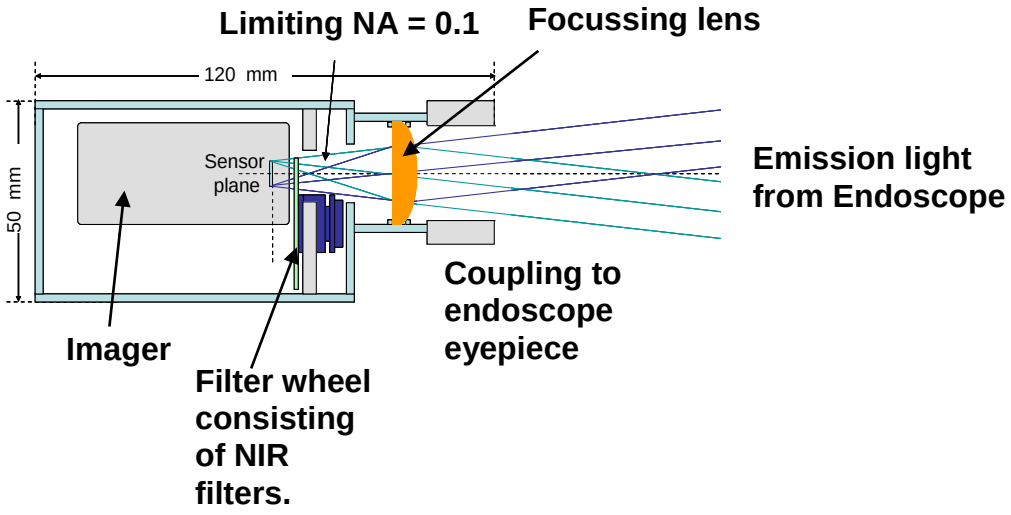

Figure 33. NIR images are collected sequentially using a segmented filter wheel mounted to a housing unit containing the CCD camera. For optimal imaging, the filter wheel rotates at the frame rate of the imager.

The design permits the use of a single dichromatic separator at the eyepiece of the laparoscope, with only two cameras required at the detection end. This detection system is therefore compact, portable and allows visible and NIR images to be acquired in parallel. Imaging of NIR wavelength bands is performed serially at optimal integration times and compared to a detection method in which NIR images are collected in parallel using dichroic and bandpass filters, this particular method is likely to lead to a much slower, acquisition system. Moreover, the use of moving parts is best avoided.

iii. A detection system based on a colour camera with its NIR filter removed.

A single monochrome CCD camera with its usual NIR filter removed is coupled to the eyepiece of the laparoscope. By inserting a stop filter segment between the lens of the eyepiece and the CCD chip, a conventional colour

image is achieved. Similarly, the insertion of appropriate narrow-band NIR filters allows discrete NIR bands to be imaged, with dynamic range limitations overcome by longer NIR integration times.

This simple optical system has the advantage of being composed of a single camera acquisition channel, with no optical image splitter required. In terms of practical limitations for such a design, the optical system needs to be highly achromatic with a colour camera capable of integration. Such devices are rare. In addition, the stop band performance of the filter segments may be optically restrictive but the overall design is likely to be less bulky at the eyepiece. Significantly however, only single NIR bands may be imaged at any given time. A variant of this scheme is to replace the usual RGBG (Red, Green, Blue, Green) mosaic filter ahead of the chip with a custom filter consisting of a RGBX mosaic, where X represents a blank filter, allowing NIR wavelengths to pass through.

iv. A detection system based on a dual CCD approach.

By utilising a dual CCD camera (e.g. AD-080-CL, Jai) which contains colour and NIR CCD chips in conjunction with a filter wheel and separating prism at the eyepiece, a further design potential for a tuneable detection system is realized (Figure 34). By inserting red, green, blue (RGB) and NIR filters into a filter wheel mounted on a housing unit containing the dual CCD camera, sequential imaging of visible and NIR wavelength bands may be possible, with dynamic range limitations overcome by frame

integration

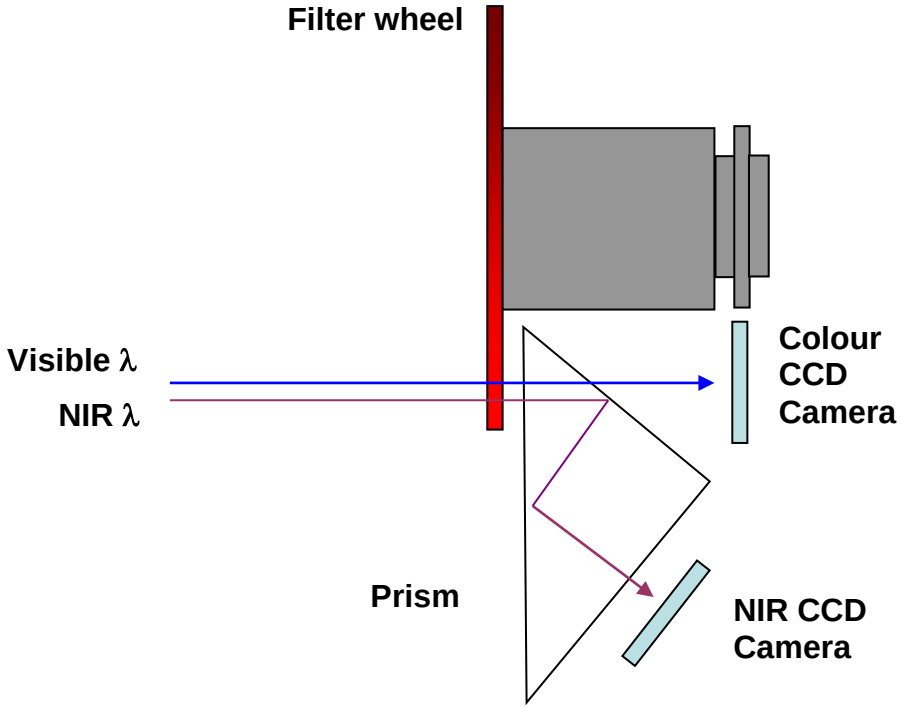

Figure 34. After leaving the eyepiece, light is passed through a series of NIR and RGB filters mounted on a filter wheel before visible and NIR bands are separated via a prism. Colour images are detected via a colour CCD chip whilst NIR images are detected with a NIR CCD chip.

The optical design in this instance is simple with only one filter wheel required and a dichromatic prism contained within the imaging unit. The optical system itself does not need to be achromatic between visible and NIR wavelengths but does still require a method of optical image splitting. The stop band performance of the filter segments are likely to be limiting and using off-the-shelf components, it is likely that the overall system could be NIR limited, with passbands <750 nm unavailable. In addition, dual CCD cameras are limited in number, are therefore expensive and may introduce undesirable bulk and weight at the eyepiece.

v. An optimal detection system based on a filtered pixel approach.

The optimal detection system is composed of a single CCD camera attached to the laparoscope's eyepiece. Emerging light is incident upon a filter matrix composed of a sequence of RGB and selected NIR filters, each of which lies on top of a single visible and NIR sensitive pixel on the imager array (Ocean Optics, U. S. A.) (Figure 35). Discrete visible and NIR wavelength bands are subsequently detected in parallel if the CCD chip is sensitive to wavelengths in the range 300-1000 nm.

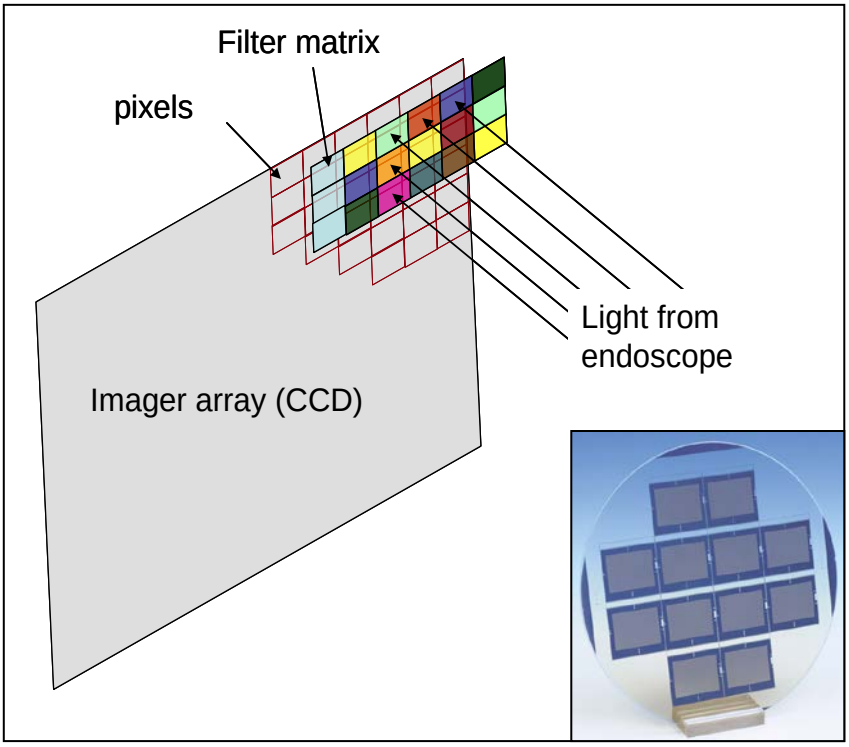

Figure 35. The optimum detection system consists of a single CCD camera coupled to the eyepiece. The CCD chip is composed of pixels situated behind a filter matrix containing RGB and NIR filters.

This particular assembly allows all wavelength bands to be available simultaneously, in turn allowing visible and NIR images to be displayed at the same time. No optical image splitter is required and the final setup is likely to

be compact with no moving parts. With the imager integral to the design, this particular construct is the optimal arrangement. However, the system has an inherently high tooling cost with non-optimal spatial resolution. In principle, colour rendition is somewhat reduced if the imager has pixels which are of equal area to those used in a conventional colour CCD chip, but by using megapixel arrays and smaller pixels, this limitation can effectively be overcome. However, the system has a non-optimal dynamic range control, since NIR filters must be selected prior to manufacture, and a non-optimal utilisation of available light. With minimal optical losses expected however, the filtered pixel approach is likely to be employed as the final detection system.

2.7 Safety Considerations

Light sources used in the field of endoscopy are inherently used to illuminate biological tissue, and they may cause thermal damage via irradiation [78]. As illumination light is activated and directed towards a sample, the local temperature of the tissue under study increases. Provided the tissue temperature does not exceed ~53^{o}, denaturation and irreversible damage is unlikely to occur. However the sample temperature must not approach ~42^{o}, above which heat-shock protein will be enhanced and tissue may become partially damaged.

The introduction of laser sources for illumination may result in an increase in thermal damage, specifically as the laser exposure time and laser powers are increased. The longer the exposure time becomes, the higher degree of damage is likely to be observed, and as expected, the higher the laser power, the earlier damage is likely to occur. Irreversible damage to

tissue is likely to occur for a lasing power of ~4 W over a 10 x 8 cm area when the exposure time is 2.4 – 2.5 s. The high local temperatures observed in such a scenario prolongs denaturation processes because the tissue takes longer to cool down below 53^{o}. NIR laser drivers used within our system have maximum optical intensities of ~5 mW/cm^{2}, are operated with soft-start operation and electrical and optical powers can be monitored and adjusted by control software. Irreversible damage caused by application of NIR lasers in our system is therefore unlikely. Additionally, immediate termination of all illumination sources may be achieved at any given time via use of an interlock controlled on the front panel of the modular NIR laser unit.

For use in human surgery, the optical image splitter is required to comply with British and European electrical safety standards [79]. The introduction of a system positioned at the eyepiece of a laparoscope must be electrically insulated from all electrical components to which it is attached. Conventional, clinically approved colour CCD cameras may be attached to the visible channel directly because plastic and rubber sheathings in which the cameras are contained prevent external leakage current flows. Commercially available NIR cameras are, in general, not approved for clinical use and must be encased within such sheathings to comply with safety standards. To overcome such a limitation, NIR light is likely to be focussed onto a 1.1 mm fibre-optic image guide for transportation to an external detector. By performing optical isolation in this way, the image splitter becomes electrically isolated by default. To compound such a safety feature, the visible and NIR channels exit the image splitter via optical components housed in insulating thermoplastics.

Chapter 3

System Testing

3.1. Optical Transmission of Endoscopic Relay Optics

The collective optical performance of Hopkins rod-lens relay systems contained within a laparoscope is critical for future *in vivo* fluorescence studies. In order to test the suitability of conventional laparoscopes (Karl Storz, Germany) for imaging in the NIR, a xenon source (Nikon Ltd., U.K.) with prominent NIR spectral peaks was imaged through the laparoscope optics and eyepiece, and its output spectrum observed with the aid of a high resolution, NIR-sensitive spectrometer (HR2000, Ocean Optics Inc., U.S.A.). Specifically, light emitted from the source was directed towards a dichroic filter of edge wavelength 662 nm (FF662, Semrock Inc., U.S.A.) to remove ~93% of optical intensity at wavelengths <662 nm. Wavelengths >662 nm were coupled into a conventional fibre-optic light guide (Karl Storz, Germany) via the combination of NIR-visible coated double- and plano-convex lenses with focal lengths 40 mm and 25 mm respectively (NT63-688 and NT45-504, Edmund Optics Ltd., U. K.). Upon leaving the fibre-optic guide, the light was directed through a series of neutral density filters (NT30-937 and NT30-938, Edmund Optics, U.K.) to reduce the intensity of all wavelengths by equal amounts and to avoid detector saturation. Thereafter, a diffuser (Edmund Optics, U.K.) was employed to scatter rays through angles of $\pm 80^{o}$ and ensure light was distributed evenly before entering the laparoscope optics.

Transmitted wavelengths were collected by a 400 μm multimode optical fibre (Thorlabs Ltd., U.S.A.) coupled to the laparoscope eyepiece and directed towards the spectrometer input. Figure 36 illustrates the optical arrangement described.

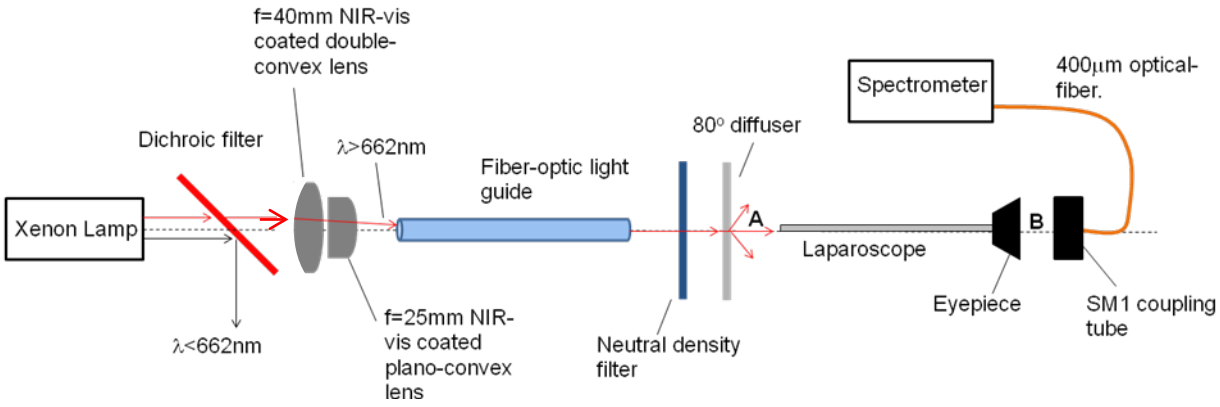

Figure 36. The optical arrangement used for measuring NIR transmission through the endoscopic relay-system optics.

A spectrum taken at position A provides the optical input to the laparoscope and a spectrum taken at position B yields the optical output. By correcting the spectra for differences in integration time, and normalizing each to a peak observed at 485 nm, the ratio between the output spectrum taken at the eyepiece and the input spectrum entering the laparoscope yields the optical transmission of the laparoscopic optics relative to 485 nm (Figure 37).

I. II.

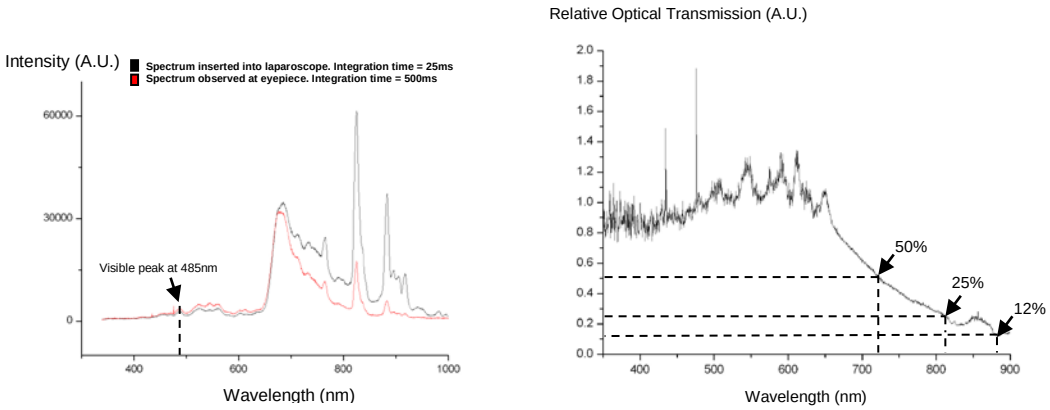

Figure 37. I. In order to gain an appreciation of NIR transmission through the laparoscope optics, spectra at the laparoscope input and at the eyepiece are taken. II. The optical transmission through the laparoscopic relay optics and eyepiece relative to 485 nm.

The relative optical transmission of the laparoscope optics reduces to 50% at 725 nm, 25% at 815 nm and reaches its minimum value of 12% at 880 nm. Reductions in the optical transmission at such wavelengths are likely to be due to optical coatings within the laparoscope, optimised at visible wavelengths.

A mathematical model was applied to the data using analysis and graphing software (OriginPro 8.1, OriginLab, Massachusetts, USA). Specifically, the model is based on a multi-peak exponential function, the equation of which is

$$y = \sum_{i=1}^{7} y_0 + \frac{A_i}{w_i\sqrt{\frac{\pi}{2}}} e^{-2\left(\frac{x-x_{c_i}}{w_i^2}\right)} \qquad (10)$$

where

$$y_0 = y_c - \frac{A_i}{\left(\frac{w_i}{\sqrt{\ln(4)}}\sqrt{\frac{\pi}{2}}\right)} \qquad (11)$$

and y_c is the Intensity at full width half maximum (FWHM). Figure 38 illustrates the mathematical model relative to the data. The model arises from the sum of fitted curves to each of the peaks observed from the data. Specifically, seven peaks were observed, each of which has a FWHM of w_i, a peak wavelength x_{ci} and an area A_i. By modelling the data in this way, experimental noise has been eliminated, and an estimation of the optical transmission through the laparoscope optics relative to 485nm can be determined.

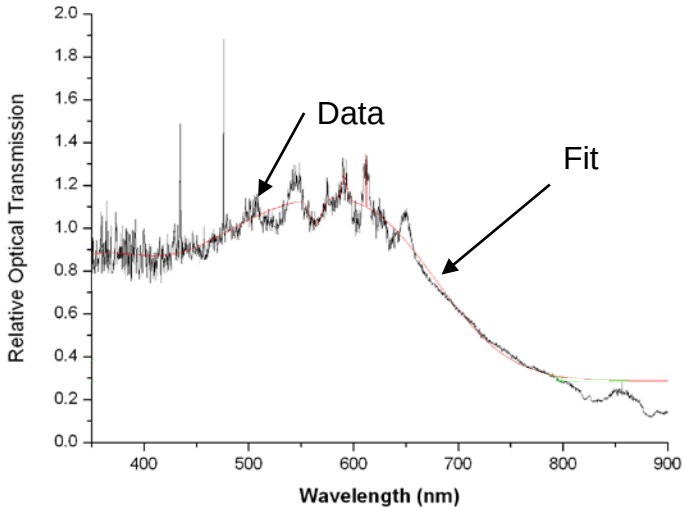

Figure 38. A multi-peak exponential function is used to model the optical transmission of visible and NIR wavelengths through the laparoscope optics relative to 485 nm.

3.2. Optical Transmission of Endoscopic Illumination Fibres

In order to stimulate fluorescence from NIR fluorophores, including those discussed in Chapter 1, illumination fibres within the laparoscope are required to transmit NIR wavelengths. In order to test the NIR transmission of the illumination fibres the xenon source was applied to the illumination port of the laparoscope via a NIR-transmissive fibre-optic light guide (Karl Storz,

Germany) and the output spectrum from the illumination fibres was measured. Light emitted from the xenon source was directed towards a dichroic filter of edge wavelength 662 nm (FF662, Semrock Inc., U.S.A.) such that ~93% of the optical intensity at wavelengths <662 nm was removed. Wavelengths >662 nm were coupled into a conventional fibre-optic light guide via a double- and plano-convex lens arrangement with focal lengths of 40 mm and 25 mm respectively. Neutral density filters were introduced prior to coupling to reduce the intensity of wavelengths entering the laparoscope by equal amounts. The fibre-optic light guide was subsequently coupled to the illumination input port on the laparoscope and light from the source was directed into the illumination fibres. Light transmitted from the illumination fibres was collected by a 400 μm fibre-optic light guide and directed towards the spectrometer input. Figure 39 illustrates the optical setup used.

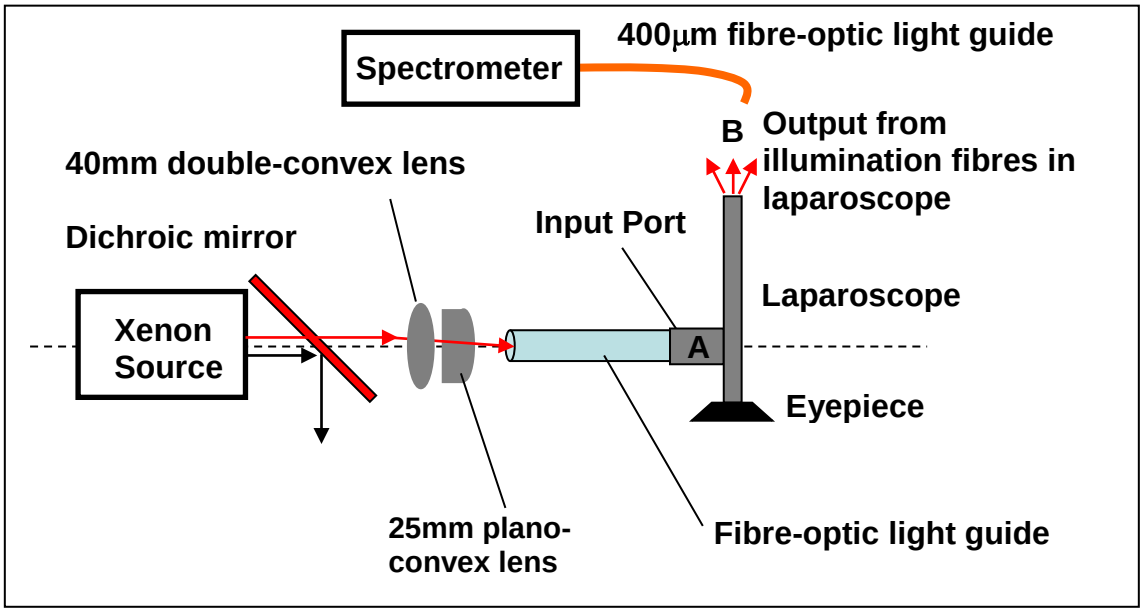

Figure 39. The optical arrangement used for measuring the transmission of visible and NIR wavelengths through conventional laparoscopic illumination fibres.

A spectrum taken at position A provides the optical input to the laparoscope illumination fibres, whilst a spectrum taken at position B yields

the optical output. By correcting the spectra for differences in integration time and normalizing each to 485 nm, the ratio between the output and input spectra yields the relative optical transmission of the illumination fibres (Figure 40).

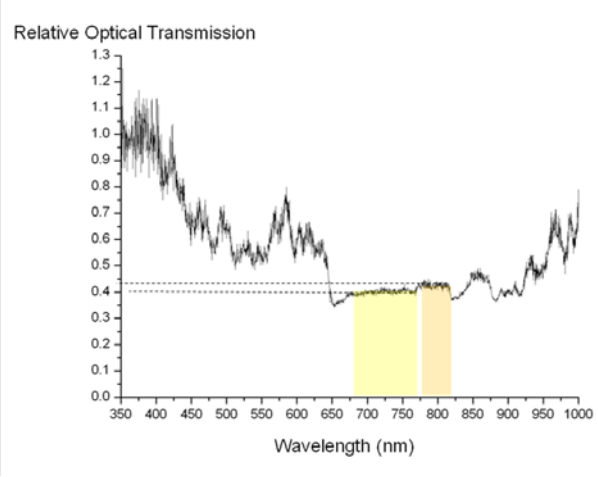

Figure 40. The optical transmission through the illumination fibres contained within the laparoscope is shown. NIR wavelength bands are highlighted.

The wavelength band 680-770 nm is found to have a relative optical transmission of ~40% whilst wavelengths between 775 nm and 815 nm have a relative optical transmission of ~44%. It is likely that reductions in transmission at such wavelengths is due to the absorption characteristics of the material from which the optical fibres are composed.

A mathematical model was applied to the data using a multi-peak exponential function. In this scenario, ten peaks were observed, yielding the equation of the mathematical fit as

$$y = \sum_{i=1}^{10} y_0 + \frac{A_i}{w_i\sqrt{\frac{\pi}{2}}} e^{-2\left(\frac{x-x_{c_i}}{w_i^2}\right)} \qquad (12)$$

where the symbols have their usual meaning. Figure 41 illustrates the mathematical model relative to the observed data. By modelling the data in this way, experimental noise has been eliminated, and an estimation of the optical transmission of the laparoscope illumination fibres relative to 485nm can be determined.

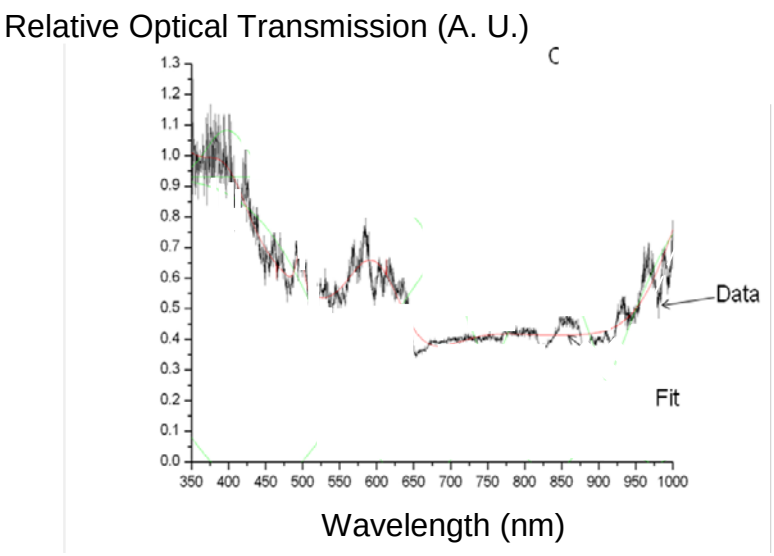

Figure 41. A multi-exponential function is used to model the optical transmission of the laparoscope illumination fibres relative to 485 nm.

3.3. Optical Power Transmission of Tuneable Excitation Light Source

In order to determine the magnitude of conventional white light that can be delivered to the sample through the light coupling unit, the power transmission of visible light through the light coupling unit was determined and compared with conventional illumination delivery powers.

The output power from a conventional fibre-optic light guide attached directly to a standard, clinically approved metal-halide source (Karl Storz, Germany) was measured using a UV-IR sensitive power meter (Model 407A,

Newport Corp., U.K.) and found to be 1.70±0.05 W. The output power from a liquid light guide coupled to the same metal-halide source using a custom-built adaptor was found to be 1.80±0.05 W. Consequently, light transmission from the metal-halide source can be improved by ~6% with the introduction of a liquid light guide.

With the liquid light guide coupled to the optical coupling unit, visible light was allowed to pass through the optics contained within it and leave through a fibre-optic guide. The power leaving the fibre-optic guide was found to be 0.50±0.05 W. The visible transmission through the optical unit is thus 29.4%. The cause of this loss is likely to be due to misalignment of the dichroic mirror relative to the optical axis and imperfections of the optical components used within the assembly.

The output power of visible light leaving the laparoscopic illumination fibres after being delivered by the conventional method is 0.50±0.05 W. With the introduction of the optical coupling unit, the output power leaving the laparoscope reduces to 0.22±0.05 W. As a result, the introduction of the unit reults in a total transmission of 34%. However, since the visible detection channel includes automatic gain control of the camera and the inability of the human eye to differentiate between such differences in optical power, illumination powers achievable with our apparatus are acceptable.

3.4. Visible and NIR Transmission of Optical Image Splitter

In order to determine the performance of the optical image splitter, and the optical performance of the dichroic filter and lenses contained within the

chassis, a broadband white light source was coupled to a UV-IR transmissive liquid light guide (Newport Inc., U.K.) and directed towards the laparoscope optics after being collimated, subjected to a series of neutral density filters (NT30-937 and NT30-938, Edmund Optics, U.K.) and directed through an 80^{o} diffuser. Light leaving the eyepiece was subsequently transferred to the optical splitting unit, with visible light reflected by the dichroic filter and passed through an optical relay system, and NIR light transmitted by the dichroic filter and passed through an 8 mm NIR-coated focussing lens. Figure 42 indicates the arrangement used to test the performance of the optical image splitter.

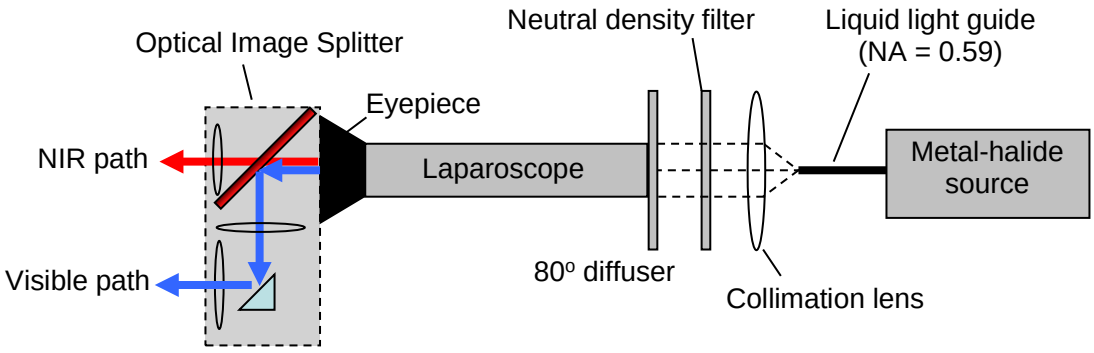

Figure 42. A broadband (~350-800 nm) white light source was passed through the laparoscope and optical image splitter to test the performance of the optical system contained within it.

A 400 μm fibre coupled to a spectrometer (HR200, Ocean Optics Inc., U.S.A.) was placed at the eyepiece to record the spectrum entering the optical image splitter. Similarly, the spectra leaving the NIR and visible paths of the optical image splitter were recorded. Figure 43 indicates the input and output spectra observed.

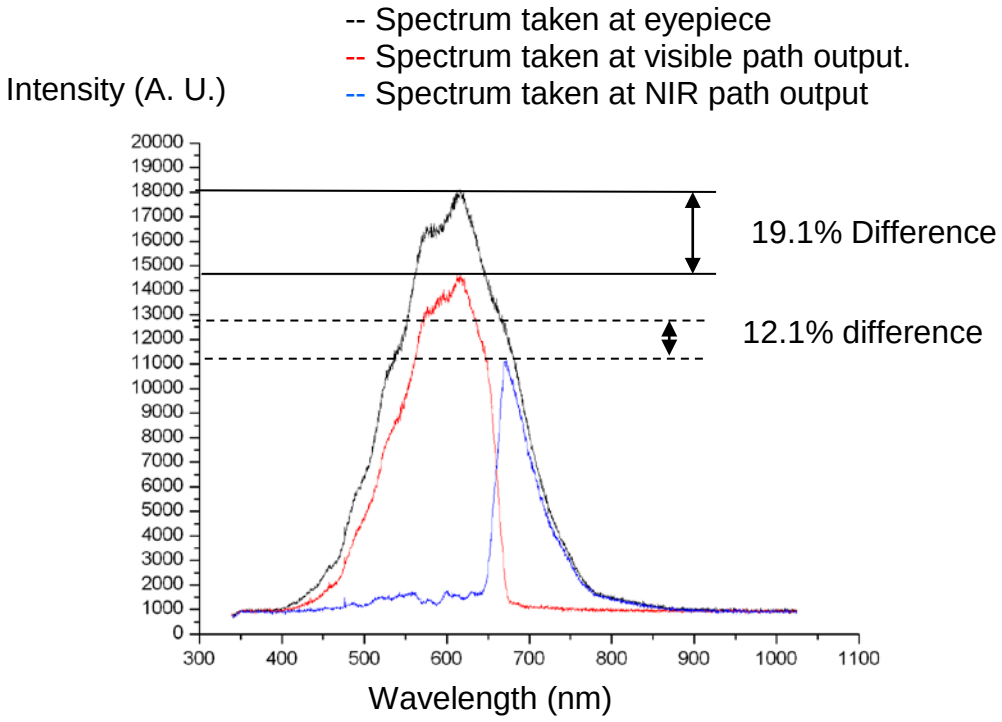

Figure 43. Spectra taken at the input (eyepiece) and output (NIR and visible paths) of the optical image splitter yield properties regarding its overall performance.

At 625 nm, where the intensity of the input reaches its maximum value, the optical image splitter has a transmission of ~80.9% along the visible path. Similarly, the optical intensity passing through the NIR channel reaches a peak at 675 nm and an optical transmission of ~87.9% is observed. Crucially, the intensities passing through the visible and NIR channels are reduced and increased by 50% respectively at 662 nm, implying the effective cut-off operation of the dichroic mirror. Wavelengths >662 nm are detected by the NIR channel whilst those <662 nm are reflected by the dichroic mirror and passed along the visible channel. A wavelength band of ~20 nm centred on 662 nm is however detected on both channels and is due to the inherent dichroic performance as shown in Figure 44:

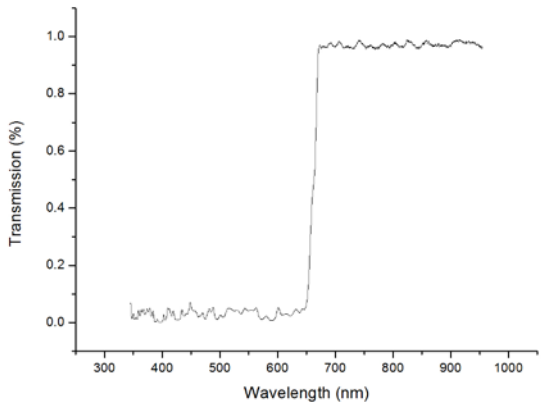

Figure 44. Optical performance of the dichroic mirror.

Quality of Images Observed through the Optical Image Splitter

The field of view (or field of view), FOV, of an optical system is often defined in terms of the angle subtended by the optical system. In endoscopic fields such as laparoscopy which normally afford only a limiting operating area, it is desirable that the introduction of any imaging modality applied to the eyepiece does not significantly reduce its value.

In order to obtain the FOV seen at the laparoscope's eyepiece, the diameter, x, seen across a plane perpendicular to the z-axis by a CCD camera was determined a distance L from the end of the laparoscope (Figure 45).

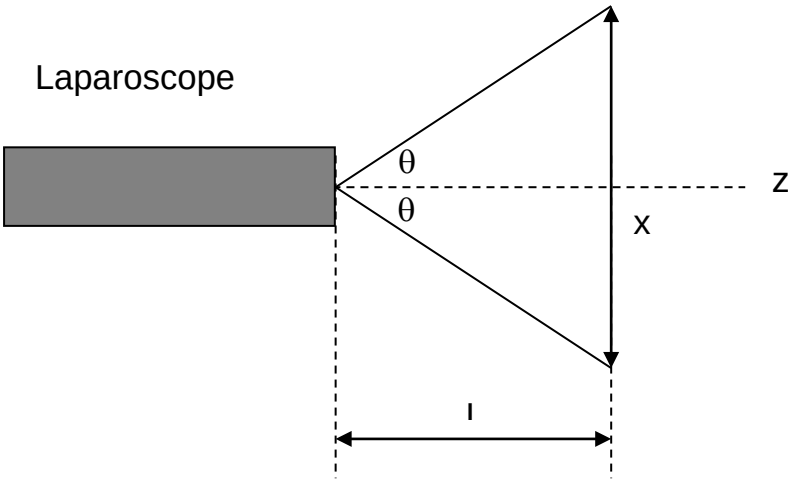

Figure 45. The FOV (FOV = 2θ) can be found given a known distance to a target, the diameter, x, of which can be directly observed.

At a distance of 105 mm, the diameter, x, observed through the eyepiece was measured to be 130 mm. The half-angle, θ, is therefore

$$\theta = Tan^{-1}\left(\frac{x}{L}\right) = 31.76^{o} \qquad (13)$$

Consequently, the field of view seen by a CCD camera at the eyepiece is

$$FOV = 2\theta = 63.52^{0} \qquad (14)$$

This angular field of view refers to the particular laparoscope used (10 mm diameter) and is, in general, reduced for smaller diameter devices. In the present case, an approximation for the laparoscope to object distance is 50 mm. At such a distance, the observed image diameter is expected to be ~62 mm.

Similarly, the diameter, x, seen by the same CCD camera (magnification and focus were unchanged) attached to the visible path of the

optical image splitter at 105 mm is 127 mm. This corresponds to a half-angle of

$$\theta = Tan^{-1}\left(\frac{x}{L}\right) = 31.16^{o} \qquad (15)$$

resulting in a FOV value of

$$FOV = 2\theta = 62.33^{0} \qquad (16)$$

At a laparoscope-object distance of 50 mm, the diameter seen by a CCD camera through the visible path of the optical image splitter is ~61 mm.

Consequently, the introduction of the optical image splitter at the laparoscope eyepiece reduces the field of view by 1.19^{o} along the visible path – a reduction seemingly acceptable for conventional colour imaging. Using the same methodology outlined, the field of view seen along the NIR channel of the optical image splitter is found to be 59.37^{o}.

Quality of Images seen at the Visible Output of the Optical Image Splitter

In optics, the term vignetting refers to a reduction of brightness at the periphery of an image compared to at its center. This undesirable effect arises due to the finite aperture (pupil size) of the optical system and to some extent is affected by finite correction applied to the system. Elements at the rear may be shaded by those in front of them, effectively reducing their opening for off-axis light. A gradual decrease in light intensity from the center to the periphery of the image is subsequently observed.

In order to quantify the effect of vignetting through the visible path of the optical image splitter, images were observed at the eyepiece and visible

output of the optical image splitter respectively, using a conventional colour CCD camera (Figure 46).

A. **B.**

Figure 46. A target consisting of a 5 x 5 mm grid and additional features is imaged A) through the laparoscope eyepiece, as in conventional imaging and B) through the visible path of the optical image splitter. Images shown have not been intensity-corrected, ie. the automatic gain control circuits of the camera have been disabled.

Intensity profiles were taken across each colour image (indicated by the red lines in Figure 46). The magnification and focus of the CCD camera remained unchanged between different imaging modalities, and the automatic gain of the camera was turned off. Figure 47 illustrates the intensity profiles obtained from the images shown in Figure 46.

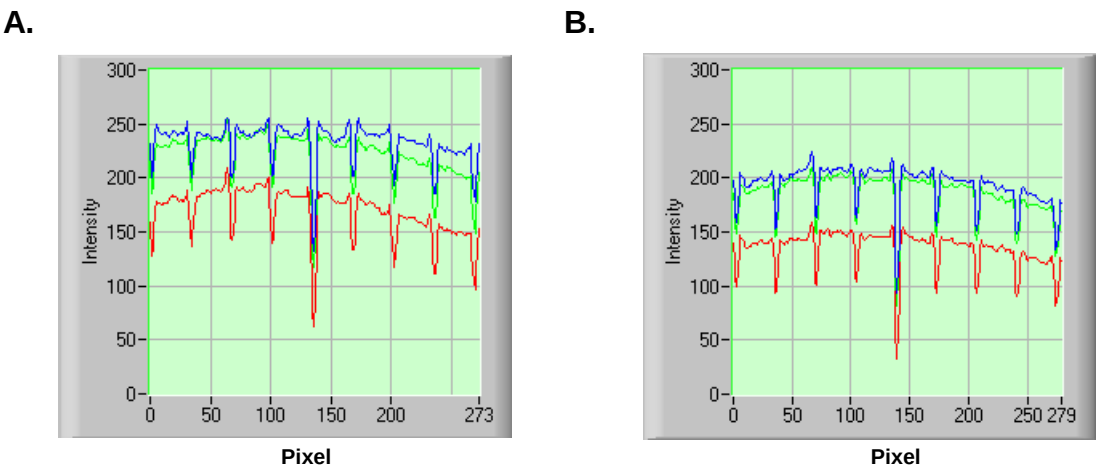

Figure 47. Intensity profiles taken across the center of A) the image seen during conventional imaging and B) the visible image emerging from the optical image splitter.

Background white levels are reduced by ~18% with the optical image splitter in place, yielding the optical transmission of the visible path within the optical image splitter as ~82%. Sharp reductions in intensity caused by the presence of black lines are observed at the same location on each image. Consequently, the radial distortions, including barrel distortion (in which image magnification decreases with distance from the optical axis) and pincushion distortion (in which magnification increases with distance from the optical axis) remain unaffected with the introduction of the optical image splitter. Notably however, the sharp reductions in intensity, particularly those close to the image edge, do not reach significantly lower intensity values as the optical image splitter is introduced. As a result, vignetting along the visible path is deemed acceptable and defined largely by the endoscope. Crucially, such results imply no significant degradation to the quality of colour images with the introduction of our system. Additionally, it can be shown that minimal distortions occur after intensity-corrections have been performed on the images. Figure 48 illustrates images seen through the eyepiece and visible

path of the optical image splitter in which images have been intensity-corrected relative to the image centre. The intensity of the image seen through the optical image splitter has been increased by 18% to compensate for the 18% loss in light transmission through the optical components. Figure 49 displays the respective intensity profiles.

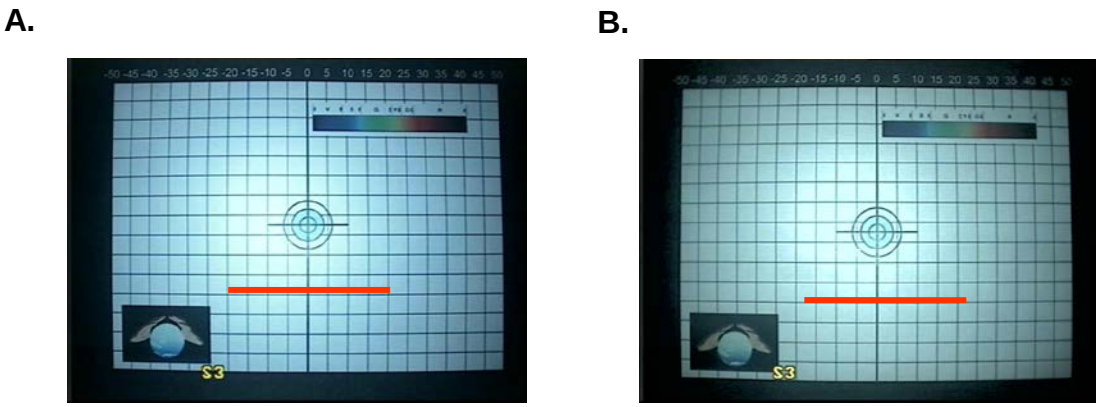

Figure 48. A target consisting of a 5 x 5 mm grid and additional features is imaged A) through the laparoscope eyepiece, as in conventional imaging and B) through the visible path of the optical image splitter. Images shown have been intensity-corrected.

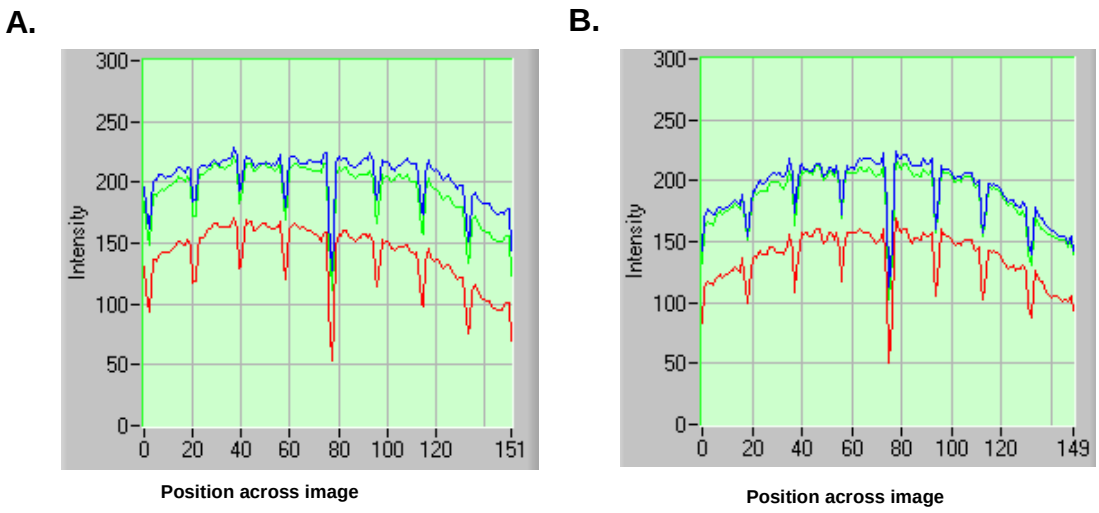

Figure 49. Intensity profiles taken across the centre of A) the image seen during conventional imaging and B) the visible image emerging from the optical image splitter. Images have been intensity-corrected.

The intensity profiles shown in Figure 49 suggest that the introduction of intensity-correction to images seen through the visible channel of the optical

image splitter results in an image quality comparable with that seen conventionally through the laparoscope eyepiece. No apparent loss of resolution is observed, vignetting is acceptable and distortions to the image are minimal.

Chapter 4

A Monte Carlo Algorithm for Visible and Near-Infrared Light Propagation in Biological Tissue.

Monte Carlo models are often used as problem solving techniques for the approximation of solutions based entirely on probabilities. Initially introduced by Ulam *et al.* [80] to study integro-differential equations, and subsequently naturally occurring physical processes, the method is currently playing a dominant role in studies aimed at simulating the propagation of light in biological tissue. In particular, Monte Carlo modeling allows photon trajectories to be recorded as photons are scattered and absorbed by media of known optical properties. Models capable of predicting the distribution of absorbed dose from external visible light sources in homogeneous tissues of different absorption and scattering coefficients have been proposed [81], yet whilst their results have significance for photo-radiation therapy studies, they have thus far neglected anisotropy and reflection.

In this section, mathematical protocols [82] which cast photon trajectories in biological tissue have been implemented as Monte Carlo processes such that one can determine, based entirely on probabilities, the most likely photon penetration depths achievable with NIR and visible illumination sources. Internal reflection and absorption of a photon at

refractive index boundaries are discussed and the use of the phase function in the generation of scattering angles is demonstrated.

4.1 The Mathematical Model

In traditional laparoscopic procedures, the abdomen is sufficiently inflated with carbon dioxide ($n_{carbon\ dioxide} \approx n_{air}$) to create a viewing space into which a laparoscope can be inserted. In a simple 2-D model, illumination photons are propagated towards the biological tissue of interest at an angle, θ_{in}, relative to an axis, x, illustrated in Figure 50.

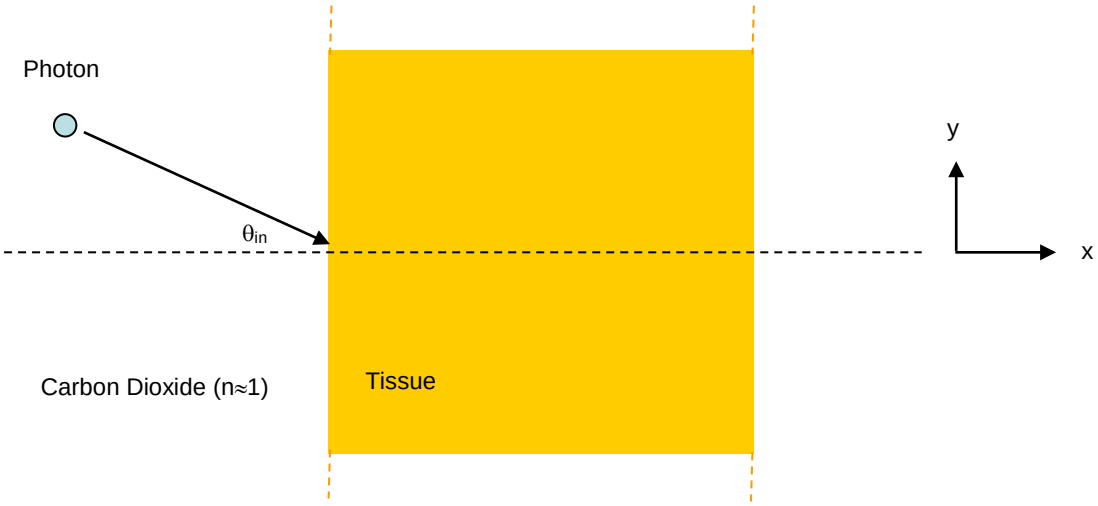

Figure 50. In a simple 2-D model, a photon leaving the laparoscope propagates in carbon dioxide gas before striking the tissue's surface at an angle, θ_{in}, relative to the x-axis.

Upon striking the surface of tissue and realizing an abrupt refractive index change, the photon is either reflected, absorbed, scattered away from or scattered into the tissue (Figure 51). In the latter scenario, the photon propagates a distance Δs to a new scattering location and is repeatedly moved until it propagates out of the tissue or is completely absorbed.

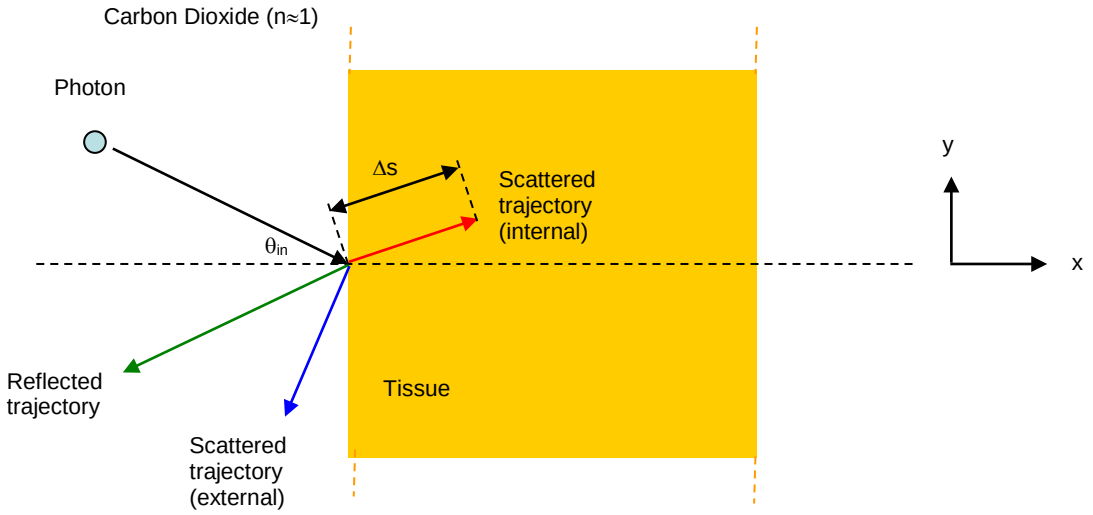

Figure 51. A photon initially traveling in carbon dioxide encounters a refractive index boundary upon striking the tissue's surface. At this point, the photon may either be completely absorbed, reflected (green trajectory), scattered out of the tissue (blue trajectory) or scattered a distance Δs into the tissue (red trajectory).

In the mathematical protocols which follow, it is assumed that the number of photons fired at the tissue is known, with each trajectory determined on a photon-by-photon basis until the desired number of propagated photons is reached. The trajectories of reflected, scattered and absorbed photons are recorded for a tissue of known optical properties, together with maximum penetration depths reached. Values obtained for the latter are likely to approach their true value as the number of photons propagated approaches infinity.

4.2. The Monte Carlo Algorithm

The Monte Carlo simulation initializes by firing the first of m photons of designated wavelength, λ, at an infinitely wide homogeneous medium of known optical properties. Each photon is directed towards the tissue target at

an angle relative to the x-axis, θ_{in}, determined by the user. The initial x-coordinate of the photon is fixed at x = 0 and, assuming all photons hit the tissue on axis at x=1 (Figure 52), the initial vertical displacement of the photon is:

$$y = l\tan(\theta_{in}) \quad (17)$$

where l is the horizontal displacement between photon and tissue. In this model, l is assumed to have a value of unity, therefore reducing Eq. (17) to

$$y = \tan(\theta_{in}) \quad (18)$$

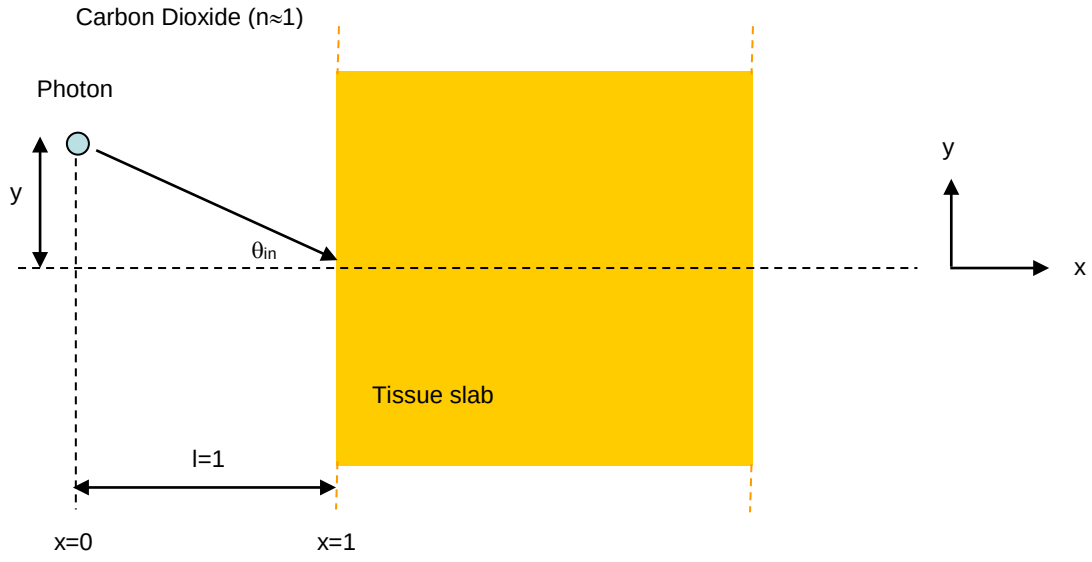

Figure 52.The photon, initially at location (0,y) strikes the surface of the tissue along the x-axis at (1,0).

For the purposes of the discussion which follows, it is assumed that photon scattering and absorption in air is negligible, allowing the photon to travel unperturbed from its starting location to the first scattering, absorption or reflection event on the tissue's surface.

i. The Photon Weight

In order to reduce the number of photons needed to achieve precision of the Monte Carlo calculations, pseudo-random numbers are used in a process known as Variance Reduction [see 82]. The concept of the photon weight, w, is introduced to reduce the variance of the simulation estimates, the size of simulation required and as a result, the number of photons required. Ultimately this results in a reduced computation time.

Consider each photon as a packet of energy. Each packet is directed towards the tissue and may follow a unique path through the sample if absorption or reflection does not occur at the interface. At each scattering location, some fraction of the packet may be absorbed at each step, and the photon is terminated when the remaining fraction decreases below an assigned value. The size of each packet of energy is called the photon weight, w, the initial value of which is set to unity.

ii. Photon Propagation Distance and the Mean Free Path Length.

In the event that the photon is scattered by the medium after striking its surface, its displacement before a further scattering event, Δs, must be small compared to its average mean free path length in the medium, L. In essence,

$$\Delta s << L = \frac{1}{\mu_t} = \frac{1}{(\mu_s + \mu_a)} \qquad (19)$$

where μ_t is the sum of the absorption and scattering coefficients associated with the medium, indicated by μ_a and μ_s respectively. In the event that $\Delta s \rightarrow 0$,

the photon will seldom interact with the tissue and the Monte Carlo simulation will return inaccurate results. On the other hand, if $\Delta s \rightarrow L$, the distance travelled by the simulated photon becomes a poor approximation. However, the probability density function for Δs is proportional to $e^{-\mu_t \Delta s}$, and thus by introducing Δs as a function of a random variable, γ,

$$\Delta s = -\frac{\ln(\gamma)}{\mu_t} \qquad (20)$$

where $\gamma \in [0,1]$, Δs now becomes an accurate estimate for the distance travelled by a photon between tissue interactions. Since Δs is unlikely to be the same throughout a photon's trajectory, the model assigns a new pseudo-random variable to each propagation step taken.

iii. Spatial Variables

At any given time, a photon's location in space may be represented by the position variables x and y. Similarly, the direction of travel may be well represented by the directional cosines μ_x and μ_y corresponding to the cosine of the angle between the x and y axes respectively. If a photon is scattered from an initial position (x, y) along a step of length Δs in the direction (μ_x, μ_y) then the new coordinates (x', y') are

$$\begin{aligned} x' &= x + \mu_x \Delta s \\ y' &= y + \mu_y \Delta s \end{aligned} \qquad (21)$$

In a 3-D model, the new z-component becomes

$$z' = z + \mu_z \Delta s \qquad (22)$$

where the symbols have their usual meaning.

iv. The Fresnel Coefficient and Probability of Reflection at an Air Tissue Interface.

When a photon initially travelling in a medium of refractive index n_1 (e.g. carbon dioxide) encounters a medium of refractive index n_2 (i.e. the tissue) there exists a finite probability, p_r , that the photon will become reflected. The probability is deduced from the Fresnel Reflection Coefficient, $R(\theta_{in})$, where

$$R(\theta_{in}) \equiv p_r = \frac{\left(\frac{1}{2} \left[\frac{\sin^2(\theta_{in} - \theta_{trans})}{\sin^2(\theta_{in} + \theta_{trans})} - \frac{\tan^2(\theta_{in} - \theta_{trans})}{\tan^2(\theta_{in} + \theta_{trans})} \right] \right)}{\max} \qquad (23)$$

The transmission angle, θ_{trans}, is found as a direct result of Snell's equation:

$$\theta_{trans} = \sin^{-1}\left(\frac{n_{air} \sin(\theta_{in})}{n_{tissue}} \right) \equiv \sin^{-1}\left(\frac{n_1 \sin(\theta_{in})}{n_2} \right) \qquad (24)$$

[see 82]. In order to determine whether the photon is reflected or transmitted upon striking the tissue's surface, a random number, α, is introduced. If $\alpha < p_r$ then reflection occurs. In this instance, the photon leaves the tissue surface at $-\theta_{in}$ and is terminated at the point (x,-y). If $\alpha > p_r$ then the photon may either transmit into the tissue via scattering with partial absorption of the photon weight or be completely absorbed. If scattering occurs then the direction and position of the photon before a further scattering event is deduced accordingly.

v. Probability of Photon Absorption

The technique of variance reduction allocates a weight of unity to each photon as it is directed towards the tissue. Upon striking the surface layer of the tissue, the weight is split into two components – a fraction, f_{abs}, is absorbed, and the remainder, f_{scat} is scattered. The latter term may be derived from the photon albedo, a, where

$$a = \frac{\mu_s}{\mu_a + \mu_s} = 1 - \frac{\mu_a}{\mu_a + \mu_s} \qquad (25)$$

since

$$f_{abs} = 1 - a \qquad (26)$$

Given that the initial photon weight is unity, the fraction scattered at the point of striking the tissue surface is

$$f_{scat} = 1 - f_{abs} = 1 - (1 - a) = a \qquad (27)$$

If $f_{abs} \neq 1$ then a proportion of the photon weight is scattered into the tissue. Subsequently, as the photon approaches the next scattering event, its new weight, w_1 is

$$w_1 = a w_0 \qquad (28)$$

In general, the weight of the photon and fraction scattered before the n'th step may be denoted by

$$w_n = a w_{n-1} \qquad (29)$$

By introducing the photon weight in this way, the location and amount of light absorbed at each scattering event may be recorded.

vi. Photon Termination

By definition, the photon weight, w_n, never reaches zero unless the absorption coefficient of tissue is assigned a value of zero. In reality, μ_a, will always be finite such that $w_n \rightarrow 0$ after multiple scattering events. When the weight falls below a specified minimum (~0.1% of w_0), the likelihood of a photon surviving and continuing to scatter in the medium becomes negligible and the photon is unlikely to yield reliable information. In this scenario, the photon is assigned a probability, p_s of surviving. If $p_s > 0.9$ the photon is allowed to continue to the next scattering event. If $p_s < 0.9$, w_n is reduced to zero. As a consequence, photon termination is achieved in a partial manner without violating energy conservation or skewing the number of absorption events.

vii. Scattering: Altering the Photon Position and Direction of Travel via the Henyey-Greenstein Phase Function.

If, upon striking the tissue surface, the photon is deemed to be scattered, a normalized phase function is used to determine the probability density function for the new azimuthal and longitudinal angles into which the photon is directed. Selecting a suitable phase function is, however, non-trivial due to the complex assemblies associated with biological tissue. Fortunately for many applications, the Henyey-Greenstein (H-G) phase function [84] acts as a reasonable approximation if the distance between the light source and

detector is of the order of 20-30 mm [85]. The original form of the Henyey-Greenstein formulation allocated a probability density function, P_{HG} of scattering into a particular angle, $\theta \in [0,\pi]$ existing between the original direction vector before scattering and the direction vector after scattering, i.e.

$$P_{HG}(\theta) = \frac{1}{4\pi} \frac{1-g^2}{\left((1+g^2-2g\cos(\theta)\right)^{\frac{3}{2}}} \qquad (30)$$

where the phase function parameter, g, is

$$g \equiv \langle \cos(\theta) \rangle = 2\pi \int_0^{\pi} \cos(\theta) P_{HG}(\theta) \sin(\theta) d\theta \qquad (31)$$

Consequently, its evaluation rendered a high computation time for each photon trajectory. By expressing the HG function in terms of $\cos(\theta)$,

$$\cos(\theta) = \frac{1}{2g} \left\{ 1+g^2 - \left(\frac{1-g^2}{1-g+2g\beta} \right) \right\} \qquad (32)$$

where β is a pseudo-random number $\epsilon[0,1]$, computation time is significantly reduced since a specific random distribution of scattering angles is determined [86]. If g = 0, then the photon is subject to isotropic scattering and the phase function has no explicit dependence on the azimuthal angle. Eq. (32) may then be expressed as

$$\cos(\theta) = 2\xi - 1 \qquad (33)$$

The longitudinal angle, ϕ, in a 3-D model may be found via

$$\phi = 2\pi\xi \qquad (34)$$

The significance of the HG function lies in its ability to generate random cos(θ) values, found by introducing uniformly distributed values $\xi \in [0,1]$, which follow the distribution law highlighted by Eq. (32) and can, as a result, be used in Monte Carlo simulations [87].

A photon initially travelling in the direction (μ_x, μ_y) and scattered into angles θ (and in 3D, ϕ) has a new direction (μ_x', μ_y') found by

$$\mu_x' = \frac{\sin(\theta)}{\sqrt{(1-\mu_z^2)}}\left(\mu_x\mu_z\cos(\phi) - \mu_y\sin(\phi)\right) + \mu_x\cos(\theta) \qquad (35)$$

$$\mu_y' = \frac{\sin(\theta)}{\sqrt{1-\mu_z^2}}\left(\mu_y\mu_z\cos(\phi) + \mu_x\sin(\phi)\right) + \mu_y\cos(\theta) \qquad (36)$$

If scattered along a z-axis, the corresponding direction of motion is

$$\mu_z' = -\sin(\theta)\cos(\phi)\sqrt{1-\mu_z^2} + \mu_z\cos(\theta) \qquad (37).$$

4.3 Development of the Monte Carlo Algorithm into a Functional Graphical User Interface.

It has been demonstrated that photon trajectories within biological media can be reconstructed by deducing absorption, emission and scattering probability functions. Implementation of this algorithm into a functional graphical user interface was achieved by following the flowchart outlined in Figure 53. All coding was performed in MATLAB (MathWorks Inc., U. S. A.).

The user is initially asked to specify the number of photons to be fired at a mammary fat tissue target, together with the initial angle of incidence relative to the optical axis and wavelength. Depending on the outcome of the latter, the absorption and scattering coefficients of the target tissue are updated to reflect experimental values reported in the literature [88, 89]. The initial location of the photons and the target tissue are subsequently animated before each photon is fired in turn towards the target.

Upon striking the tissue's surface, the probabilities of photon absorption, reflection and scattering are computed. If absorbed, the photon is terminated and its trajectory towards the tissue is plotted. Similarly, if reflection occurs, the photon is terminated and the trajectory of reflection is determined. In the event that the photon is neither absorbed nor reflected, scattering of the photon by the tissue is deemed to occur and the photon is moved to the next absorption or scattering event. If however during this movement, or any movement thereafter, the trajectory leaves the tissue, the photon is terminated. At the next scattering or absorption event, a new photon weight is determined and compared to the predetermined cutoff value. If the photon weight falls below this value, the photon is terminated since it is unlikely to yield any useful information. Alternatively the photon propagates to subsequent absorbers or scatterers until termination ultimately occurs. The process repeats for each photon until all photons have been monitored.

Upon completion of the algorithm, the average maximum penetration depth reached within the tissue for each photon is calculated before an average penetration depth and standard error are found and displayed on the user interface (Figure 54).

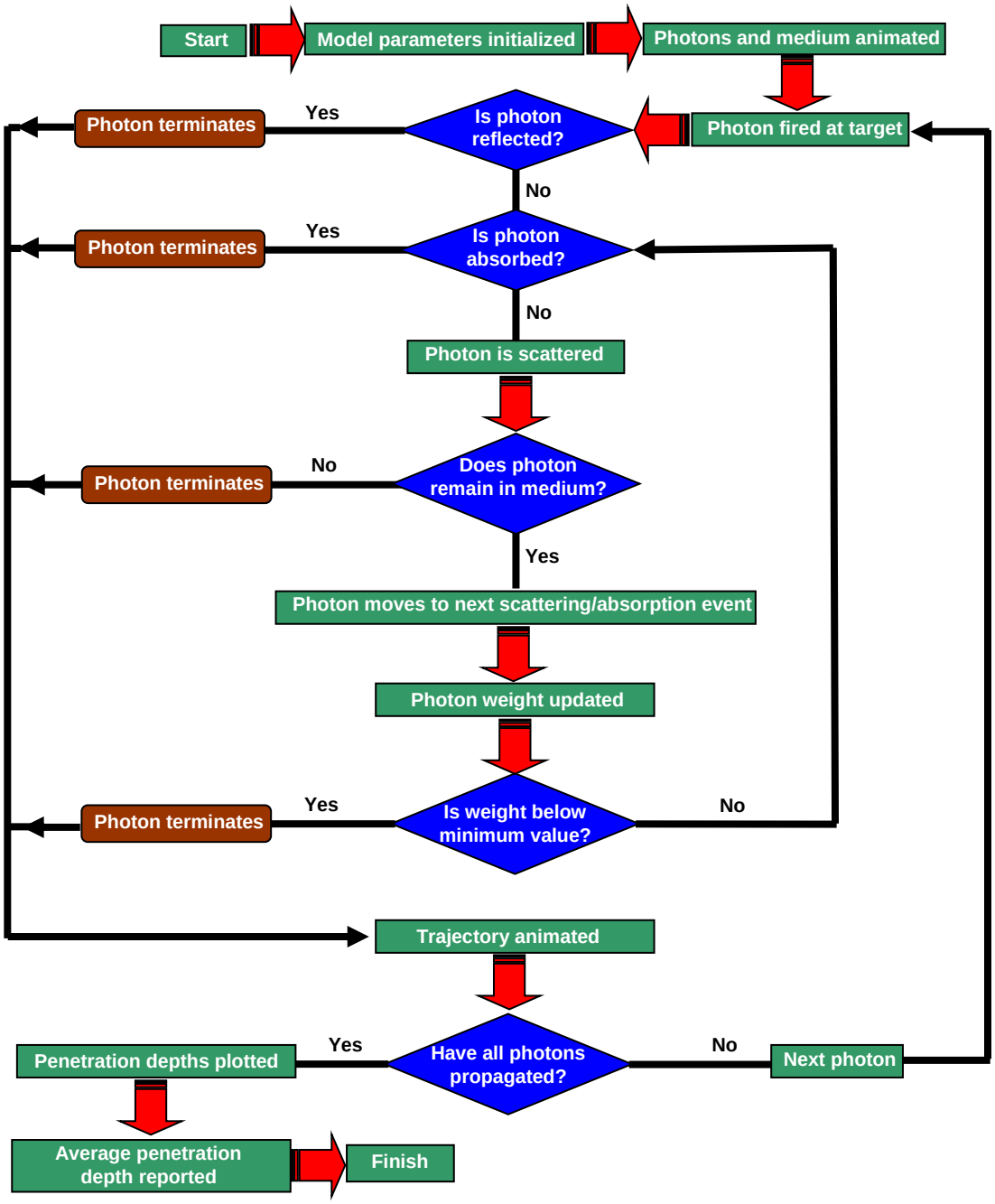

Figure 53. Flowchart of the Monte Carlo algorithm used to model photon migration in biological tissue. After the model parameters have been initialized, each photon is sequentially fired at a tissue target. The probabilities of absorption and internal reflection are checked as the photon hits the tissue surface. In the event of reflection or absorption, the photon is terminated. If the photon is scattered into the medium, then propagation to the next absorption/scattering event is permitted and a new photon weight is determined. Photons may propagate within the medium until the photon weight reduces below a minimum value. In the event of a photon leaving the medium via scattering, the photon is terminated. The process

repeats until all photon trajectories have been monitored, at which point the penetration depths reached are recorded.

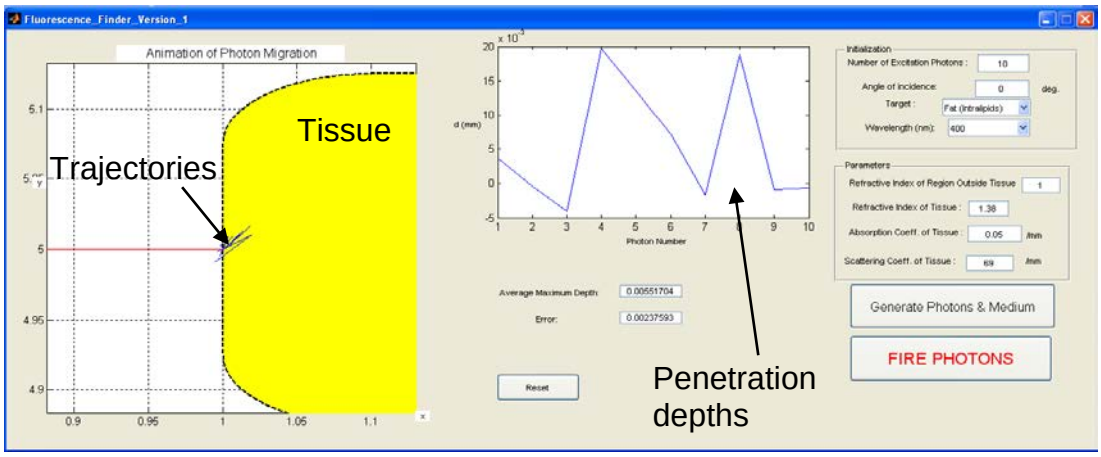

Figure 54. The graphical user interface constructed for modeling photon migration through biological tissue. The number of photons, initial angle of incidence, their wavelength and target are entered by the user after which model parameters, including absorption and scattering coefficients in tissue are updated. The target and photons are animated and each photon trajectory is modeled sequentially. Photon penetration depths, d, are recorded together with the average maximum depth reached and the corresponding error.

In order to allow differentiation between photons reflected and scattered away from the medium, reflected photons are issued green trajectories whilst those scattered out of and away from the medium are highlighted in blue (Figure 55).

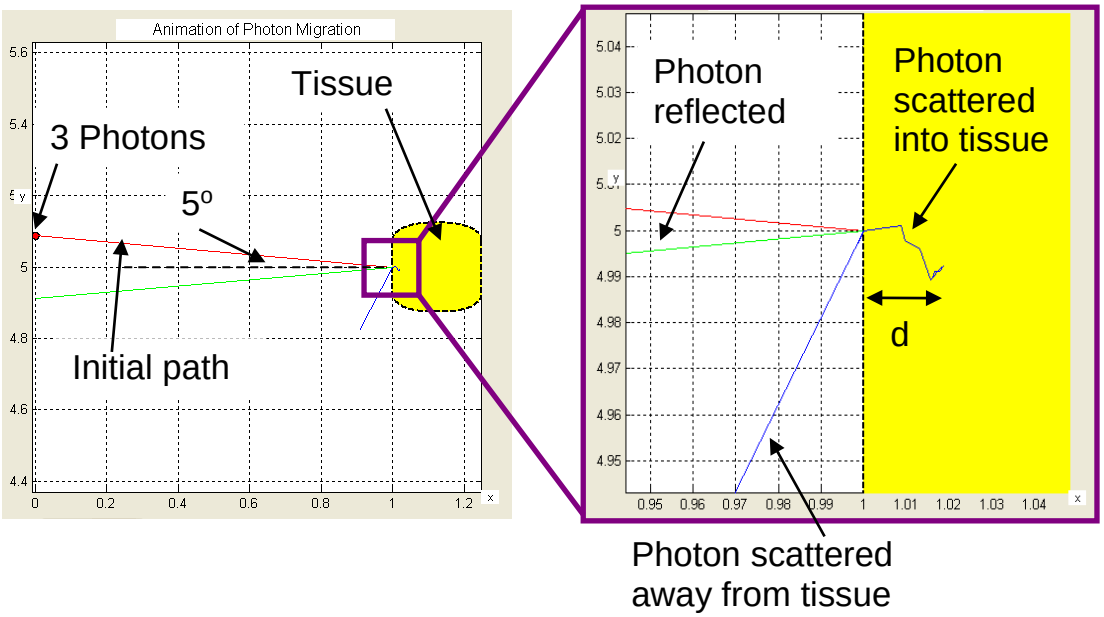

Figure 55. Example of the Monte Carlo model in action. In this instance, three photons (650 nm) were fired at the tissue at 5º relative to the x-axis (red trajectory). One photon is scattered into the tissue, reaching a maximum penetration depth, d, before being terminated. A second photon is reflected at the tissue surface (green trajectory) whilst the third is scattered out of and away from the medium (blue trajectory indicated).

4.4. Determination of Optical Penetration Depths

In order to evaluate the performance of the model, the algorithm was initially implemented in four runs of 10,000 photons per wavelength, with the angle of incidence set to 0º and the tissue target set to mammary fat (Figure 56). The resulting penetration depths were computed and those in the NIR were compared to optical penetration depths observed experimentally by Stolik *et al.* [90] in a method incorporating the diffusion model of light transport.

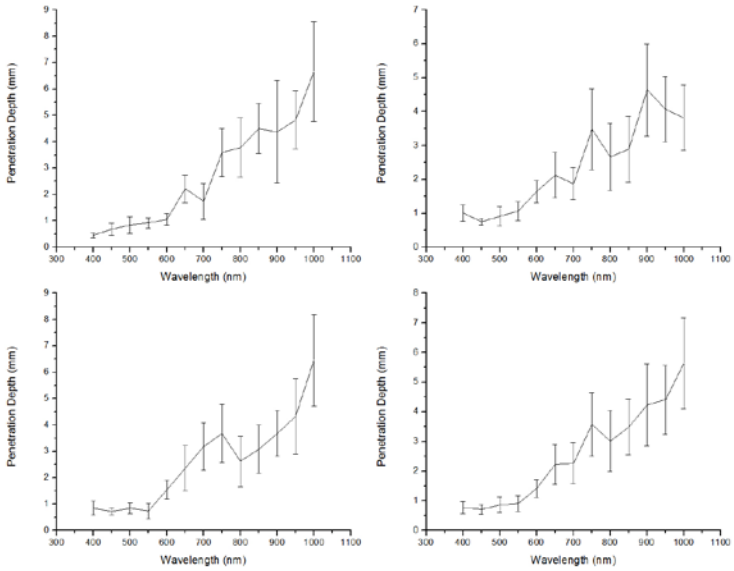

Figure 56. The algorithm was implemented in four runs, each of which consisted of 10,000 photons per wavelength. NIR wavelengths were found to consistently reach, on average, greater penetration depths than those in the 400 – 600 nm range.

For a set of 40,000 photons, each of which was attributed a trajectory based entirely on probabilities, the average penetration depth as a function of wavelength was computed (Table 2). NIR wavelengths were found to reach a greater average penetration depth, compared to wavelengths in the range 400–600 nm range. A 67.5% increase in the average penetration depth was observed between 400 nm and 700 nm, with a 74.8% increase observed between 400 nm and 800 nm.

Wavelength (nm)	**Average Penetration Depth (mm)**
400	0.75 ± 0.20
450	0.66 ± 0.16
500	0.86 ± 0.27
550	0.91 ± 0.25
600	1.40 ± 0.30
650	2.19 ± 0.68
700	2.31 ± 0.69
750	3.54 ± 1.07

800	2.98 ± 1.03
850	3.45 ± 0.95
900	4.18 ± 1.38
950	4.34 ± 1.16
1000	5.49 ± 1.52

Table 2. Using data from Figure 54, the average penetration depth reached as a function of wavelength was determined. An increase of 4.74 mm was observed between 400 nm and 1000 nm, highlighting the consistency of the model with scattering theory.

To compound the consistency of the algorithm with scattering theory, and to emphasise its reliability, predicted photon penetration depths returned by the model were compared to experimental values reported in the literature (Table 3). At 633 nm, the algorithm recorded an accuracy of 97.8% and at 675 nm and 835 nm, the model was found to be 86.7% and 69.0% accurate respectively. In order to reduce the error associated with values reported in the literature, a larger number of photons (e.g. in excess of 100,000) should be examined.

Wavelength (nm)	**Predicted Penetration Depth (mm)**	**Observed Penetration Depth (mm)**
633	1.85	1.81
675	2.3	2.03
780	3.32	2.24
835	3.1	2.79

Table 3. NIR photon penetration depths returned by the Monte Carlo simulation agree with those observed experimentally in the literature.

For the proposed NIR lasing wavelengths included in the spectrally-agile endoscope design, expected photon penetration depths in mammary fat tissue were calculated (Table 4). At 690 nm, 732 nm, 785 nm and 830 nm, the model returned depths of 2.27 mm, 2.90 mm, 3.15 mm and 3.26 mm respectively. Subsequently, the introduction of such NIR wavelengths is likely to improve depth penetration by upwards of ~55%.

Laser Wavelength (nm)	**Expected Penetration Depth (mm)**
690	2.27
732	2.90
785	3.15
830	3.26

Table 4. The Monte Carlo simulation allows the average photon penetration depth to be revealed for NIR lasing wavelengths proposed in our spectrally-agile endoscope design.

Photon penetration depths as a function of angle of incidence were additionally computed by the Monte Carlo model for visible and NIR wavelengths (Figure 57). It is observed that as the angle of incidence increases from 0^{o} to 45^{o}, the photon penetration depth decreases by ~28% across all wavelengths.

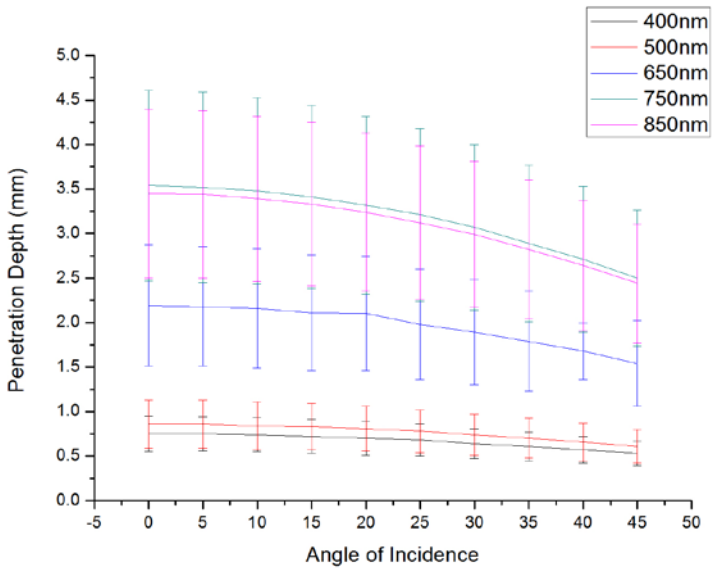

Figure 57. The average penetration depths reached by photons of wavelength 400 nm, 500 nm, 650 nm, 750 nm and 850 nm were calculated as a function of the angle of incidence.

Chapter 5

Discussion

The field of endoscopy is at the forefront of modern surgical techniques, allowing biological structures within the body to be studied in a minimally invasive (keyhole) fashion. Its introduction has played a crucial role in the reduction of patient morbidity rates and post-operative recovery times, but perhaps most significantly, it has helped improve the quality of life for many requiring surgery. As technological developments in the field of endoscopy continue to progress rapidly, a new generation of imaging modalities are being produced and those already existing are being utilized in conjunction with ultrasound [91] and MRI [92] to answer important biological questions. Developments in optical instruments, laser-based technologies and computing power are enhancing the field, allowing three-dimensional images of internal structures to be visualized and analyzed at the organ, tissue and cellular levels, revealing otherwise unobtainable pathological data. However, a variety of technological challenges still remain and a number of limitations have yet to be overcome. In terms of image quality, reductions in fish-eye magnification and distortion are desirable, together with improvements in magnification and resolution at the cellular and sub-cellular levels. Off-axis illumination is needed to alleviate vignetting and improve depth perception, and enhanced illumination sources are required for optimal contrast. Progress is necessary in the development of CCD chips to improve the precision of colour representation of tissues and three-dimensional cameras, polarized

light detectors and systems capable of providing binocular viewing would all be advantageous. In terms of mechanical design, instruments with increased degrees of freedom would assist surgical procedures and the development of micro, ultra-slim endoscopes may allow enhanced tissue imaging in regions inaccessible to contemporary techniques. Overcoming such engineering and scientific obstacles are likely to lead to improved diagnostic procedures and ultimately patient care.

A variety of studies supporting the validity and clinical usefulness of endoscopy applied to sentinel node mapping have recently been reported. Specifically, detection of the sentinel node via endoscopy has enhanced staging procedures by allowing the status of lymph node metastasis to be monitored. As such, endoscopy has played a crucial role in making appropriate treatment decisions.

At present, the radio- or dye-guided methods, and often a combination of both, is utilized to determine the metastatic state of cancer via the detection of sentinel nodes. The radio-guided method has been shown to be a useful tool for detecting their location; however, lymphatic vessels and channels connecting adjacent nodes are difficult to visualize and in a number of hospitals, legal constraints limit its use [93, 94]. Additionally, high levels of radioactivity at the injection site may interfere with the detection of the sentinel node. The dye-guided method is a convenient and safe alternative but the fast excretion of the dye after injection presents one of its limiting factors. Furthermore, the method only allows nodes on the surface layer of tissue to be visualized making detection of sentinel nodes in deep, dark anatomical regions problematic. In this study, a radically novel endoscopic method for

sentinel node mapping has been presented. This has the capability of exploiting the NIR window to image fluorescence from nodes below the surface layer of tissue.

Intraoperative imaging systems based on extracting fluorescence from clinically approved dyes (e.g. indocyanine green, methylene blue and 5-ALA) have been developed for monitoring the flow of blood and lymph fluid. Specifically, such techniques have been employed for neurovascular surgery, organ transplantation, and recently, sentinel node mapping. In the latter, bright NIR fluorescence signals allow real-time visualization of the lymphatic channels and sentinel nodes which are not directly visible by the naked eye. With autofluorescence of tissue reduced at NIR wavelengths, high signal-to-noise ratios have been achieved, indicating the high sensitivity of the fluorescence imaging technique. The introduction of a spectrally-agile fluorescence imaging system during laparoscopic surgery is therefore expected to be a reliable and useful method for determining the location of the sentinel node and is likely to enhance intraoperative staging of a primary tumour.

This work focuses on the development of an endoscope which is both spectrally-agile in the detection and illumination of clinically approved NIR fluorescent dyes injected into tissue. Obtaining spectral information from tissue fluorescence may allow differentiation between normal and cancerous tissue, particularly in cases where distinctions cannot be made using the naked eye. By utilizing simple optical geometries which can be utilized to image fluorophores with emission bands in the near-infrared, a minimally-invasive setup capable of providing subsurface imaging and spectral analysis

has been developed, and may allow for additional diagnostic information to be obtained *in vivo*. Specifically, real-time analysis of the lymphatic system in the vicinity of a tumour may be possible from the development of an optical image splitter. Conventional visible and NIR fluorescence images can be viewed *simultaneously* during surgery, and as a direct consequence, sentinel nodes are likely to be mapped effectively and efficiently. In addition, our design offers a new solution based entirely on commercially available, microlens optics.

A tuneable illumination module which combines visible light from a metal-halide source with NIR laser diodes has been achieved. Visible light may be employed to illuminate the sample for conventional colour imaging, whilst a series of laser diodes, with wavelengths ranging from 690-830 nm, may be used for fluorescence excitation. NIR light penetrates deep into tissue, and has the potential of detecting NIR fluorophores under tissue fat, including those which are bound to plasma proteins in the lymphatic vessels and nodes.

In order to gain an appreciation of the optical penetration depths achievable with our design, a Monte Carlo model of light propagation in turbid biological media has been presented. Based entirely on probabilities, photon trajectories, migration and penetration depths reached in fat tissue have been examined, with results aligning well with experimental data previously published in the literature. The model initially assumes a collimated light source but may be adjusted to accommodate diffuse irradiance if the initial photon direction is chosen randomly from all possible directions. As a photon propagates towards the biological tissue of interest, scattering and absorption in carbon dioxide is neglected and all photons are permitted to strike the

tissue target. In reality, the scattering coefficient of a pure carbon dioxide gas, β, may be well represented by

$$\beta = \frac{8\pi^3 (n(\lambda)-1)^2}{3\lambda^4 N}\left(\frac{6+3\rho}{6-7\rho}\right) \qquad (38)$$

where n(λ) is the refractive index of the molecular gas, N is the number of particles per cubic centimetre at temperature T and pressure P, λ is the wavelength of light and p is the depolarization constant [94]. However, scattering and absorption coefficients of media inside the body are likely to change significantly from person to person and equally, as the photon strikes the tissue surface, the media into which it propagates is expected to be inhomogeneous, with haemoglobin, oxyhaemoglobin and a variety of different tissue cells in abundance. Additionally, as Brownian motion occurs in a typical sample region, photons propagated at different times are unlikely to collide with identical matter.

In order to improve the efficiency of the Monte Carlo method further, implicit capture may be employed. In this technique, a larger number of photons (and larger packet of energy) are transmitted towards the tissue, subsequently improving variance reduction. Absorbing or discarding any remaining weight during photon termination may however skew the absorption profile or violate energy conservation, and a roulette technique, similar to the one presented, must be incorporated in the any such algorithm.

An alternative method to the Monte Carlo algorithm for modelling light transport in biological tissue incorporates the diffusion equation, a derivative of the radiative transport equation, in which light propagation is assumed to be

isotropic [96]. The latter equation is conservative, an approximation to Maxwell's equations and states that the radiance of photons travelling from an initial location, R, along direction $\hat{s}$, at time t, is equivalent to the sum of all mechanisms which contribute to an increase in its value, minus the sum of those mechanisms which reduce it. To date, the diffusion equation has been successfully employed in modelling light transport in diffuse media [97], but the model must ensure that the wavelength of propagated light is much smaller that the dimensions of the tissue under study since wave effects (e.g. diffraction) are neglected. Additionally, this model requires the medium to have a constant refractive index and is computationally expensive when modelling photon migration in large 3D volumes. The Monte Carlo algorithm presented allows for such limitations to be overcome, whilst yielding NIR photon penetration depths which are in agreement with those observed experimentally.

Sentinel node mapping in combination with NIR fluorescence based laparoscopy offers a minimally invasive surgical tool which may be of great benefit to patient recovery rates. To our knowledge, no paper describing a spectrally-agile laparoscopic approach to sentinel node mapping by fluorescence imaging has been published to date. Our developments are aimed at accurately predicting the metastatic status in the lymphatic system within the vicinity of a tumour. By doing so, our system may help reduce the need for lymphadenectomy. In patients where lymph node metastasis is not present, only dissection of the lymph nodes in the same basin as the sentinel node may be sufficient as a treatment. In situations where metastasis has occurred, standard lymphadenectomy should be performed. What is more,

post-operative quality of life is likely to improve as a result, but clinical studies using a large number of patients are required before any such claim can be made. As a consequence of the implementation of spectrally-agile fluorescence laparoscopy to sentinel node mapping, a variety of other clinical applications are likely to arise, particularly as NIR fluorophore chemistry develops [98].

Chapter 6

Concluding Remarks and Future Work

Conventional methods for sentinel node mapping are limited to shallow penetration depths, with nodes obscured by several layers of tissue fat likely to be overlooked. As a consequence, methods relying on the dye-guided methodology are entirely dependant on user experience and have the potential to report the existence of false-negative sentinel nodes if the true sentinel node is concealed. Fortunately, developments in the field of near-infrared fluorescence detection have extended the depths to which imaging can occur during surgery. By injecting clinically approved, near-infrared fluorescent dyes (e.g. indocyanine green, methylene blue) intradermally at the site of a primary tumour, nodes receiving dye uptake and subsequently drainage from the tumour can be monitored. Crucially, the near-infrared fluorescence signals (~650-900 nm) have low absorption coefficients in tissue compared with visible wavelengths, and are able to penetrate to much greater depths. Conventional fluorescence mapping techniques report on the detection of peak fluorescence signals from dye molecules excited at a single wavelength. In this study, the development of a novel spectrally-agile fluorescence laparoscope is reported, capable of performing conventional illumination and imaging as well as NIR excitation and fluorescence detection.

Our apparatus utilizes a tuneable illumination unit which combines NIR lasers with a halogen white light source, to supply conventional illumination and excitation wavelengths to the laparoscope via a fibre-optic light guide.

Visible and near-infrared fluorescence images of the sample area are relayed from the distal to proximal end of the laparoscope via a series of Hopkins rod-lens relay systems. Visible wavelengths are subsequently separated from NIR wavelengths by an optical image splitter situated at the eyepiece. Each wavelength band is thereafter transferred to their respective detectors: colour images are passed towards a visible CCD camera whilst NIR wavelengths are sent towards a tuneable NIR detector.

Implementation of a tuneable illumination unit has been achieved by allowing collimated white- and NIR-laser-diode light to propagate parallel to an axis passing through the centre of a fibre-optic light guide, via a dichroic mirror with a 662 nm edge wavelength. All wavelengths are coupled into the fibre-optic guide via an optical arrangement consisting of NIR-visible coated double- and plano-convex lenses. Illumination is subsequently transferred to optical fibres at the proximal end of the laparoscope before irradiating the sample. Transmission along such fibres reduces to ~44% in the near-infrared, relative to those in the visible. At present, the illumination unit increases light transmission from the metal-halide source by 6%, but a power loss of 70.6% is observed as light is transported to the laparoscope. This loss, though apparently severe, is tolerable, particularly so with the presence of automatic gain in the detection channels. It is likely however that further work will be performed to enhance the optical design of the illumination optics, and in particular, to reduce any misalignment of the dichroic and optical filters.

An optical image splitter capable of separating visible and near-infrared components has been prototyped. It has been found that the optical components within the laparoscope have the ability to transmit both visible

and NIR wavelengths, with transmission relative to 485 nm reducing to 50% at 725 nm, 25% at 815 nm and 12% at 880 nm. As such, visible and NIR wavelengths are expected to reach the optical image splitter. After leaving the eyepiece, NIR wavelengths are transmitted by a dichroic mirror and initially focussed onto a NIR sensitive CCD chip with a transmission of ~87.9%. Visible images are reflected by the mirror and relayed to a conventional colour CCD chip with an optical transmission of 80.9%. Crucially, visible images observed at the optical image splitter have a field of view comparable with those observed at the eyepiece, display little vignetting and negligible distortions. Consequently, the image quality remains unaffected with the introduction of the optical image splitter.

The NIR detection channel is initially composed of a NIR bandpass filter and 25 mm focussing lens to direct NIR light onto an appropriately sensitive CCD chip or an 8 mm focussing lens used for coherent guide imaging. Whilst suitable for laboratory and animal studies, the initial system is not adequate for human studies because the NIR CCD camera is not electrically isolated. A series of alternative tuneable detection channels have thus been proposed in this study, with a detector based on microlithographic pixelated filters likely to be used in the final design. However, this requires high tooling costs and only becomes practical when appropriate emission passbands have been selected using alternative prototypes. Upon the determination of such passbands and implementation of a tuneable NIR detector, it is likely that a variety of fluorescence signals from a wide range of fluorophores will be gained. Clinical applications, and particularly those aimed at sentinel node mapping, will follow.

Our system, upon completion, is likely to be involved in studies aimed at sentinel node mapping in primates. Specifically, the aim is to detect sentinel nodes from animals recently diagnosed with colon cancer using a wide range of fluorophores, including NIR dyes attached to super-paramagnetic iron-oxide nanoparticles (SPIONs) for improved node retention. Each animal will be injected systematically with an infusion of SPIONs, each of which acts additionally as an MRI contrast agent. MRI scans will be performed prior to surgery and an injection of fluorescent dyes will subsequently follow. Thereafter, fluorescence laparoscopy will be performed with the aim of detecting and removing the sentinel lymphatic node for histology. Non-approved clinical dyes (e.g. Cy 5.5 and Cy 7) may also be introduced for fluorescence based laparoscopy in further animal experiments. Eventually, it is expected that our system to be used in the clinic for gastrointestinal and gynaecological sentinel node mapping.

In order to determine NIR photon migration in mammalian fat tissue of known absorption and scattering coefficients, an algorithm has been presented which casts photon trajectories as Monte Carlo processes such that one may determine, based entirely on probabilities, the most likely optical penetration depth for a given wavelength of incident light. Analytical solutions reveal optical penetration depths of 2.27 mm, 2.90 mm, 3.15 mm and 3.26 mm for laser wavelengths of 690 nm, 732 nm, 785 nm and 830 nm respectively - values which agree well with those previously reported by experimental methods. The model can be performed faster than alternative techniques but further work is required to enhance the algorithm’s accuracy: absorption and scattering effects must be incorporated as a photon travels in

carbon dioxide gas and variance reduction must be improved whilst preserving energy conservation. It has been shown that the algorithm is successful in revealing photon migration in mammary fat tissue for a variety of wavelengths spanning the visible and NIR portions of the electromagnetic spectrum, and in principle, the model may be extended to reveal photon trajectories and ultimately optical penetration depths in a variety of turbid and diffuse media.

In conclusion, a spectrally-agile endoscopic imaging system for highly-sensitive and real-time sentinel node mapping during laparoscopic surgery has been presented. The technique could be useful in predicting the metastatic status in lymphatic nodes draining a primary tumour. Dissection of the sentinel node with the aid of NIR fluorescence-guided laparoscopy may be a promising approach as a new minimally invasive surgical tool for patients exhibiting abdominal, gastric and gynaecological tumours. Significantly however, our developments may not be strictly limited to sentinel node mapping techniques and may have far-reaching clinical applications.

References

[1] H. Gray, Gray's Anatomy: the anatomical basis of medicine and surgery. *Churchill Livingstone*. **38**, 1431-1433 (1995).

[2] R. V. Kristić, Human Microscopic Anatomy: An Atlas for Students of Medicine and Biology, *Springer Verlag*, **3**, 78 (1997).

[3] P. G. Herman, I. Yamamoto & H. Z. Mellins, Blood microcirculation in the lymph node during the primary response. *J. Exp. Med.* **136**, 697 (1972).

[4] G. I. Schoefl. The migration of lymphocytes across the vascular endothelium in lymphoid tissues. *J. Exp. Med.* **136**, 568 (1972).

[5] C. Nopajaroonsri, S. C. Luk & G. T. Simon. The architecture of the normal lymph node and hemolymph node. *Lab Invest.* **29**, 258-265 (1973).

[6] D. L. Morton, D. Wen, J. H. Wong, J. S. Economou, L. A. Cagle, F. K. Storm, L. J. Foshag & A. J. Cochran. Technical details of intraoperative lymphatic mapping for early stage melanoma. *Arch. Surg.* **127**, 392-399 (1992).

[7] S. Saha, R. Seghal, M. Patel, K. Doan, A. Dan, A. Bilchik, T. Beutler, D. Wiese, N. Bassily & C. Yee. A multicenter trial of sentinel lymph node mapping in colorectal cancer: prognostic implications for nodal staging and recurrence. *Am. J. Surg.* **191**, 305-310 (2006).

[8] M. Bertagnolli, B. Miedema, M. Redston, J. Dowell, D. Niedzwiecki, J. Fleshman, J. Bem, R. Mayer, M. Zinner & C. Compton. Sentinel node staging of resectable colon cancer: results of a multicenter study. *Ann. Surg.* **240**, 624-628 (2004).

[9] U. Veronesi, G. Paganelli, V. Galimberti, G. Viale, S. Zurrida, M. Bedoni, A. Costa, C. Cicco, J. G. Geraghty, A. Luini, V. Sacchini & P. Veronesi. Sentinel node biopsy to avoid axillary dissection in breast cancer with clinically negative lymph nodes. *Lancet.* **349**, 1864-1867 (1997).

[10] T. Kitai, T. Inomoto, M. Miwa, T. Shikayama. Fluorescence navigation with indocyanine green for detecting sentinel lymph nodes in breast cancer. *Breast. Canc.* **12**, 211-215 (2005).

[11] J. B. Kinmonth. Lymphangiogram in man: method outlining lymphatic trunks and operation. *Clin. Sci.* **11**, 13-20 (1952).

[12] A. Sherman & M. Ter-Pogossian. Lymph node concentration of radioactive colloid gold following interstitial injection. *Cancer.* **6**, 1238-1240 (1953).

[13] M. R. S. Keshtgar & P. J. Ell. Sentinel lymph node detection and imaging. *Euro. J. Nuc. Med.* **26**, 57-67 (1999).

[14] L. Bergqvist, S. E. Strand, B. Persson, L. Hafstrom & P. E. Jonsson. Dosimetry in lymphoscintigraphy of TC-99m antimony sulphide collide. *J. Nucl. Med.* **23**, 698-705 (1982).

[15] G. Mariani, L. Moresco, G. Viale, G. Villa, M. Bergnasco, G. Canavese, J. Buscombe, H. W. Strauss & G. Paganelli. Radioguided sentinel lymph node biopsy in breast cancer surgery. *J. Nucl. Med.* **42**, 1198-1215 (2001).

[16] T. Tiourina, B. Arends, D. Huysmans, H. Rutten, B. Lemaire & S. Muller. Evaluation of surgical gamma probes for radioguided sentinel node localisation. *Euro. J. Nucl. Med.* **25**, 1224-1231 (1998).

[17] D. L. Morton, D. Wen, J. H. Wong, J. S. Economou, L. A. Cagle, F. K. Storm, L. J. Foshag & A. J. Cochran. Technical Details of Intraoperative Lymphatic Mapping for Early Stage Melanoma. *Arch. Surg.* **127**, 392-399 (1992).

[18] M. K. Lingam, R. M. Mackie & A. J. McKay. Intraoperative identification of sentinel lymph node in patients with malignant melanoma. *J. Canc.* **75**, 1505-1508 (1997).

[19] A. E. Giuliano, D. M. Kirgan, J. M. Guenther & D. L. Morton. Lymphatic mapping and sentinel lymphadenectomy for breast cancer. *Ann. Surg.* **220**, 391-401 (1994).

[20] T. Ichikura, D. Morita, T. Uchida, E. Okura, T. Majima, T. Ogawa & H. Mochizuki. Sentinel Node Concept in Gastric Carcinoma. *J. Surg.* **26**, 318-322 (2002).

[21] A. Raabe, J. Beck, R. Gerlach, M. Zimmerman & V. Seifert. Near-Infrared Indocyanine green video angiography: a new method for intraoperative assessment of vascular flow. *Neurosurgery.* **52**, 132-139 (2003).

[22] M. Sekjima. An intraoperative fluorescent imaging system in organ transplantation. *Transplant Proc.* **36**, 2188-2190 (2004).

[23] M. Kusano, Y. Tajima, K. Yamazaki, M. Kato, M. Watanabe & M. Miwa. Sentinel Node Mapping Guided by Indocyanine Green Fluorescence Imaging: A New Method for Sentinel Node Navigation Surgery in Gastrointestinal Cancer. *Dig. Surg.* **25**, 103-108 (2007).

[24] T. Kitai, T. Inomoto, M. Miwa & T. Shikayama. Fluorescence Navigation with Indocyanine Green for Detecting Sentinel Lymph Nodes in Breast Cancer. *Breast Canc.* **12**, 211-215 (2005).

[25] R. C. Benson & H. A. Kues. Fluorescence properties of indocyanine green as related to angiography. *Phys. Med. Biol.* **23**, 159-163 (1978).

[26] P. Hillemanns, J. Reiff, H. Stepp & P. Soergel. Lymph node metastasis detection of ovarian cancer by porphyrin fluorescence photodetection: case report. *Lasers Med. Sci.* **22**, 131-135 (2007).

[27] M. Kriegmair, R. Baumgartner, R. Knuchel, H. Stepp, F. Hofstadter & A. Hofstetter. A detection of early bladder cancer by 5-aminolevelunic acid induced porphyrin fluorescence. *J. Urol.* **155**, 105-109 (1996).

[28] W. Stummer, S. Stocker, S. Wagner, H. Stepp, C. Fritsch, C. Goetz, A. Goetz, R. Kiefmann & H. J. Reulen. Interaoperative detection of malignant gliomas by 5-aminolevelunic acid-induced porphyrin fluorescence. *Neurosurg.* **42**, 518-526 (1998).

[29] Y. Murayama, Y. Harada, K. Imaizumi, P. Dai, K. Nakano, K. Okamoto, E. Otsuji, T. Takamatsu. Precise detection of lymph node metastases in mouse rectal cancer by using 5-aminolevulinic acid. *Int. J. Canc.* **125**, 2256-2263 (2009).

[30] Y. Tajima, M. Murakami, K. Yamazaki, Y. Masuda, M. Kato, A. Sato, S. Goto, K. Otsuka, T. Kato & M. Kusano. Sentinel Node Mapping Guided by Indocyanine Green Fluorescence Imaging During Laparoscopic Surgery in Gastric Cancer. *Ann. Surg. Oncol.* **In print**. (2010).

[31] J. Mack, R. J. Aranoff, T. E. Acuff, M. B. Douhit, R. T. Bowman & W. H. Ryan. Present role of thorascopy in the diagnosis and treatment of the chest. *Annals of Thoracic Surg.* **54**, 403-408 (1992).

[32] A. Marwan, C. Harmon, K. E. Georgeson, G. F. Smith & O. J. Muensterer. Use of Laparoscopy in the Management of Paediatric Abdominal Trauma. *J. Trauma.* **In Print**. (2010).

[33] M. C. Roughton, M. Millis, G. Testa & A. Fichera. Laparoscopic En Bloc Resection of Locally Advanced Colon Cancer with Involvement of the Liver, Small Bowel, Omentum, and Abdominal Wall. *Surg. Laparoscopy, Endoscopy & Percutaneous Techniques.* **19**, 38-40 (2009).

[34] A. Husain, D. S. Chi, M. Prasad, N. Abu-Rustum, R. R. Barakat, C. L. Brown, E. A. Poynor, W. J. Hoskins & J. P. Curtin. The Role of Laparoscopy in Second-Look Evaluations for Ovarian Cancer. *Gynecologic Oncol.* **80**, 44-47 (2001).

[35] C. L. Kay, D. Kulling, R. H. Hawes, J. W. R. Young & P. B. Cotton. Virtual Endoscopy – Comparison with Colonoscopy in the Detection of Space Occupying Lesions of the Colon. *Endoscopy.* **32(3)**, 226-232 (2000).

[36] T. Kuiper, P. Fockens & E. Decker. Colonoscopy, tumors and inflammatory bowel disease. *Endoscopy essentials.* **42**, 49-52 (2010).

[37] S. A. Boppart, T. F. Deutsch & D. W. Rattner. Optical imaging technology in minimally invasive surgery. *Surg. Endoscopy.* **13**, 718-722 (1999).

[38] D. F. Jimminez. Intracranial Endoscopic Neurosurgery. *Am. Soc. Neurol. Surg.* **1**, 3-5 (1998).

[39] S. Dobson & H. H. Hopkins. A new rod-lens relay system. *J. Phys. E. Soc.* **22**, 450-455 (1989).

[40] S. J. Dobson. An easily manufactured rod-lens relay system with improved image quality. *Meas. Sci. Technol.* **3**, 674-677 (1992).

[41] J. G. Websterm Minimally Invasive Medical Technology. *IOP Pub.* 1, 136-137 (2001).

[42] A. D. Muller & A. Sonnenberg. Prevention of Colorectal Cancer by Flexible Endoscopy and Polypetomy: A Case-Control Study of 32 702 Veterans. **123**, 904-910 (1995).

[43] R. Lorenz, G. Jorysz & M. Clasen. The globus syndrome: value of flexible endoscopy of the upper gastrointestinal tract. *J. Laryngology & Otology.* **107**, 535-537 (1993).

[44] J. S. Ploem & H. J. Tanke. Introduction to Fluorescence Microscopy. *Oxford Sci. Pub.* **10**, 1 (1987).

[45] S. D. Quinn, J. C. Penedo-Esteiro, I. D. W. Samuel. Advanced optical techniques to study the molecular basis of Alzheimer's disease. *Univ. St. Andrews* (2008).

[46] G.G. Guilbault. Practical Fluorescence. *CRC Press.* **2**, 76-77 (1990).

[47] B. W. Rice & C. H. Contag, The Importance of Being Red. *Nat. Biotech.* **27**, 624-625 (2009).

[48] J. B. Pawley, Handbook of Biological Confocal Microscopy. *SpringerScience and Business New York*. **3**, 338-352 (2006).

[49] T. Chishima, Y. Miyagi, X. Wang, H. Yamaoka, H. Shimada, A. R. Moossa & R. M. Hoffman. Cancer Invasion and Micrometatastasis Visualized in Live Tissue by Green Fluorescent Protein Expression. *Cancer Res.* **57**, 2042-2047 (1997).

[50] R. M. Hoffman. Imaging cancer dynamics in vivo at the tumour and cellular level with fluorescent proteins. *Clin. Exp. Metastasis.* **26**, 345-355 (2009).

[51] X. Shu, A. Royant, M. Z. Lin, T. A. Aguilera, V. Lev-Ram, P. A. Steinbach & R. Y. Tsien. Mammalian Expression of Infrared Fluorescent Proteins Engineered from a Bacterial Phytochrome. *Sci.* **324**, 804-807 (2009).

[52] Q. Peng, T. Warloe, K. Berg, J. Moan, M. Kongshaug, K. Giercksky, J. M. Nesland. 5-Aminolevulinic acid based photodynamic therapy. Clinical research and future challenges. *Canc.* **79**, 2282-2308 (1997).

[53] T. J. Dougherty, B. W. Henderson, C. J. Gomer, G. Jori, D. Kessel, M. Korbelik, J. Moan & Q. Peng. Photodynamic Therapy. *J. Nat. Canc. Inst.* **90**, 889-905 (1998).

[54] M. Kondo, N. Hiroto, T. Takaoka & M. Kajiwara. Hemebiosynthetic enzyme activities and porphyrin accumulation in normal liver and hepatoma cell lines of rat. *Cell Biol. Toxicol.* **9**, 95-105 (1993).

[55] R. Pottier. In vitro and in vivo fluorescence monitoring of photosensitizers. *J. Photochem. Photobiol. B.* **6**, 103-109 (1990).

[56] A. M. Wennberg, F. Gudmundson, B. Stenquist, A. Ternesten, L. Molne, A. Rosen & O. Larko. In vivo detection of basal cell carcinoma using imaging spectroscopy. *Acta Dermatol Venereol*. **79**, 54-61 (1999).

[57] T. Momma, M. R. Hamblin & T. Hasan. Hormonal modulation of the accumulation of 5-aminolevulinic acid-induced protoporphyrin and phototoxicity in prostate cancer cells.

[58] J. Bedwell, A. J. MacRobert, D. Phillips & S. G. Bown. Fluorescence distribution and photodynamic effect of ALA-induced PP-IX in the DMH rat colonic tumor-model. *J. Cancer*. **65**, 818 (1992).

[59] M. T. Wyss-Desserich, C. H. Sun, P. Wyss, C. S. Kurlawalla, U. Haller, M. W. Berns & Y. Tadir. Accumulation of 5-Aminolevulinic Acid-Induced Protoporphyrin IX in normal and neoplastic human endometrial epithelial cells.

[60] M. Kriegmair, Detection of Early Bladder Cancer by 5-Aminolevulinic Acid Induced Porphyrin Fluorescence. *J. Urol.* **155 (1)**, 105-110 (1996).

[61] J. W. Meng, X. J. Wang, H. P. Ma, X. G. Ren, X. R. Xu & W. M. Ren. Protoporphyrin IX fluorescence from the plasma of tumor-implanted mouse. *J. Lumin.* **83**, 251-254 (1999).

[62] M. B. Ericson, S. Grapengiesser, F. Gudmundson, A. Wennberg, O. Larko, J. Moan & A. Rosen. A spectroscopic study of the photobleaching of protoporphyrin IX in solution. *Lasers. Med. Sci.* **18**, 56-62 (2003).

[63] J. Caesar, S. Shaldon, L. Chiandussim L. Guevara & S. Sherlock. The use of indocyaninee green in the measurement of hepatic blood flow and as a test of hepatic function. *Clin. Sci.* **21**, 43-57 (1961).

[64] H. Schad, H. Brechtelsbauer & K. Kramer. Studies on the suitability of a cyanine dye (Viher-Test) for indicator dilution technique and its application to the measurement of pulmonary artery and aortic flow. *European J. Physiol.* **370**, 139-144 (1977).

[65] C. P. Herbert, P. LeHoang & Y. Guex-Crosier. Schematic interpretation of indocyanine green angiography in posterior uveitis using a standard angiographic protocol. *Opthalmol.* **105**, 432-440 (1998).

[66] Y. Tajima, M. Murakami, K. Yamazaki, M. Kato, A. Sato, S. Goto, K. Otsuka, T. Kato & M. Kusano. Sentinel Node Mapping Guided by Indocyanine Green Fluorescence Imaging During Laparoscopic Surgery in Gastric Cancer. *Ann. Surg. Oncol.* **In print**. (2010).

[67] http://omlc.ogi.edu/spectra/icg/

[68] H. T. Gold, H. T. Do & M. P. Osborne. Cost-effectiveness of isosulfan blue vs. methylene blue dye in sentinel node biopsy. *J. Clin. Oncol.* **23**, 6103 (2005).

[69] R. Simmons, S. Thevarajah, M. B. Brennan, P. Christos & M. Osborne . Methylene blue dye as an alternative to isosulfan blue dye for sentinel lymph node localization. *Ann. Surg. Oncol.* **10**, 242-247 (2003).

[70] K. Eldrageely, M. P. Vargas, I. Khalkhali, R. Venegas, M. Burla, K. D. Gonzalez & H. I. Vargas. Sentinel lymph node mapping of breast cancer: a case-control study of methylene blue tracer compared to isosulfan blue. *Ann. Surg.* **70**, 872-875 (2004).

[71] A. Nour. Efficacy of methylene blue dye localization of sentinel lymph node in breast cancer patients. *Breast J.* **10**, 388-391 (2004).

[72] L. A. Newman. Lymphatic mapping and sentinel node biopsy in breast cancer patients: a comprehensive review of variations in performance and technique. *J. Am. Coll. Surg.* **199**, 804-816 (2004).

[73] K. M. McMaster, T. M. Tuttle, D. J. Carlson, C. M. Brown, R. D. Noyes, R. L. Glaser, D. J. Vennekotter, P. S. Turk, P. S. Tate, A. Sardi, P. B. Cerrito & M. J. Edwards. Sentinel lymph node biopsy for breast cancer: a suitable alternative to routine axillary dissection in multi-institutional practice when optimal technique is used. *J. Clin. Oncol.* **18**, 2560-2566 (2000).

[74] W. K. Hung, C. M. Chan, M. Ying, S. F. Chong, K. L. Mak & A. W. C. Yip. Randomized clinical trial comparing blue dye with combined dye and isotope for sentinel lymph node biopsy in breast cancer. *Brit. J. Surg.* **92**, 1494-1497 (2005).

[75] J. M. East, C. S. P. Valentine, E. Kanchev & G. O. Blake. Sentinel lymph node biopsy for breast cancer using methylene blue dye manifests a short learning curve among experienced surgeons. *BMC Surg.* **9**, 2 (2009).

[76] T. L. Klausen, A. H. Chakera, E. Frills, F. Rank, B. Hesse & S. Holm. Radiation doses to staff involved in sentinel node operations for breast cancer. *Clin. Physiol. Imaging.* **25**, 196-202 (2005).

[77] M. Chu & Y. Wan. Sentinel lymph node mapping using near-infrared fluorescent methylene blue. *J. Biosci. Bioeng.* **107**, 455-459 (2009).

[78] J. Zhou, J. K. Chen & Y. Zhang, Theoretical Analysis of Thermal Damage in Biological Tissues Caused by Laser Irradiation, *MCB*, **4 (1)**, 27-39 (2007).

[79] Medical electrical equipment – Part 1: General requirements for basic safety and essential performance.

[80] N. Metropolis & S. Ulam, The Monte Carlo method. *J. Am. Stat. Assoc.* **44**, 335-341 (1949).

[81] B. C. Wilson & G. Adam, A Monte Carlo model for the absorption and flux distributions of light in tissue. *Med. Phys.* **10**, 824-830 (1983).

[82] S. A. Prahl, M. Keijzer, S. L. Jacques & A. J. Welch. A Monte Carlo Model of Light Propagation in Tissue. *SPIE*. **5**, 102-111 (1989).

[83] B. A. P. James. Variance Reduction Techniques. *J. Opt. Res. Soc.* **36(6)**, 525-530 (1985).

[84] L. G. Henyey & J. Greenstein. Diffuse radiation in the galaxy. *Astrophys. J.* **93**, 70-83 (1941).

[85] M. Campolat & J. Mourant. High-angle scattering events strongly affect light collection in clinically relevant measurement geometries for light transport through tissue. *Phys. Med. Biol.* **45**, 1127-1140 (2000).

[86] A. N. Witt. Multiple scattering in reflection nebulae I. A Monte Carlo approach. *Astrophys. J.* **35**, 1-6 (1977).

[87] T. Binzoni, T. S. Leung, A. H. Gandjbakhche, D. Rufenacht & D. T. Delpy. The use of the Henyey-Greenstein phase function in Monte Carlo simulations in biomedical optics. *Phys. Med. Biol.* **51**, 313-322 (2006).

[88] S. J. Matcher, M. Cope & D. T. Delpy. *In vivo* measurements of the wavelength dependence of tissue-scattering coefficients between 760 and 900 nm measured with time-resolved spectroscopy. *Applied Optics. **36**,* 386-396 (1997).

[89] B. J. Tromberg, O. Coquoz, J. B. Fishkin, T. Pham, E. R. Anderson, J. Butler, M. Cahn, J. D. Gross, V. Venugopalan & D. Pham. Non-invasive measurements of breast tissue optical properties using frequency domain migration. *Phil. Trans. R. Soc. B.* **352**, 661-668 (1997).

[90] S. Stolik, J. A. Delgado, A. Perez & L. Anasagasti. Measurement of the penetration depths of red and near infrared light in human “ex vivo” tissues. *J. Photochem. Photobiol. B.* **57**, 90-93 (2000).

[91] S. R. Puli, M. L. Bechtold, J. B. K. Reddy, A. Choudhary, M. R. Antillon & W. R. Brugge. How Good is Endoscopic Ultrasound Differentiating Various T Stages of Rectal Cancer? Meta-Analysis and Systematic Review. *Surg. Oncol.* **16**, 254-265 (2008).

[92] S. Sathyanarayana & P. A. Bottomley. MRI endoscopy using intrinsically localized probes. *Med. Phys.* **36**, 908-919 (2009).

[93] Y. Kitagawa, H. Fujii, K. Kumai, T. Kubota, Y. Otani, Y. Saikawa, M. Yoshida, A. Kubo & M. Kitajima. Recent advances in sentinel node navigation for gastric cancer: a paradigm shift of surgical management. *J. Surg. Oncol.* **90**, 147-151 (2005).

[94] T. Aikou, Y. Kitagawa, M. Kitajima, Y. Uenosono, A. J. Bilchik, S. R. Martinez & S. Saha. Sentinel lymph node mapping with GI cancer. *Canc. Metastasis Rev.* **25**, 269-277 (2006).

[95] D. R. Cutten. Rayleigh Scattering Coefficients for Dry Air, Carbon Dioxide, and Freon-12. *Appl. Optics.* **13 (3)**, 468-469 (1974).

[96] S. R. Arridge. Optical tomography in medical imaging. *Inverse Problems.* **15**, 41-93 (1999).

[97] D. Contini, F. Martelli & G. Zaccanti. Photon migration through a turbid slab described by a model based on diffusion approximation. I. Theory. *Appl. Optics.* **36**, 4587-4599 (1997).

[98] J. Frangioni. In vivo near-infrared fluorescence imaging. *Curr. Opin. Chem. Biol.* **7**, 626-634 (2003).